Developments in Extended Finite Element Methods for Extraction of Strain Energy Release Rates and Computational Nanomechanics for SWCNT Aggregates

Mengyu Lan

Submitted in partial fulfillment of the
requirements for the degree
of Doctor of Philosophy
in the Graduate School of Arts and Sciences

COLUMBIA UNIVERSITY

2013

©2013
Mengyu Lan
All Rights Reserved

ABSTRACT

Developments in Extended Finite Element Methods for Extraction of Strain Energy Release Rates and Computational Nanomechanics for SWCNT Aggregates

Mengyu Lan

In this dissertation, developments in computational mechanics are presented in two parts. In the first part, a new analytical approach, within the extended finite element (XFEM) framework, is proposed to compute Strain Energy Release Rates (SERRs) directly from Irwin's integral. Crack tip enrichment functions in XFEM allow for evaluation of integral quantities in closed form (for some crack configurations studied) and therefore results in an accurate and efficient method. The effects of high order enrichments, mesh refinement and the integration limits of Irwin's integral are examined in benchmark numerical examples. The results indicate that high order enrichment functions have significant effect on the convergence, in particular when the integral limits are finite. When the integral limits tend to zero, simpler SERR expressions are obtained and high order terms vanish. Nonetheless, these terms contribute indirectly via coefficients of first order terms.

The analytical formulation is then extended to cracks in arbitrary orientations. Several benchmark examples are investigated including off-center cracks, inclined cracks and crack growth problems. On all these problems, the method is shown to work well, giving accurate results. Moreover, due to its analytical nature, no special postprocessing is required which leads to a fast approach to obtain Strain Energy Release Rates. Thus it is concluded that this method may provide a good alternative to the popular J-integral method.

In the second part of the thesis, the stress-strain behavior of short single walled carbon nanotube (SWCNT) aggregates is investigated by a novel incremental constrained minimization approach. An AIREBO potential is used to model the interactions within and

between CNTs. The idea is to homogenously disperse SWCNTs in the computational cell at random positions and orientations following spherical uniform distributions, and incrementally deform the cell while restraining the movement of atoms at the ends of nanotubes. The stress-strain response of the system is obtained in each loading direction and it is shown to converge to an isotropic behavior (a similar response in all directions) as the number of CNTs in the system increases. In addition, it is shown that the Young's modulus of the system increases linearly with the CNT aggregates density and the method agrees well with results obtained from molecular dynamics simulations running at near zero degrees kelvin, which are obtained at only a fraction of the CPU time required for MD methods.

Table of Contents

I Introduction **1**

1 Scope and Outline **2**

1.1 Introduction 2

1.2 Outline 3

II An Analytical Method to Extract SERRs from Irwin's Integral-I **5**

2 Introduction & Literature Survey **6**

3 Modeling cracks by the extended finite element method **9**

3.1 Problem Statement 9

3.2 XFEM overview 10

3.3 High order enrichment functions 12

4 Extraction of Strain Energy Release Rates using Irwin's integral and XFEM **14**

4.1 Analytical expansion of Irwin's integral 14

4.2 XFEM realization of Irwin's integral 18

5 Numerical examples **22**

5.1 Mode I: Single Edge Notch Tension (SENT) problem 23

5.2 Mode II example 25

5.3 Mixed mode benchmark problem 26

III An Analytical Method to Extract SERRs from Irwin's Integral-II 31

6 Introduction 32

7 Extraction of Strain Energy Release Rates using Irwin's integral and XFEM 33

7.1 Analytical expansion of Irwin's integral 33

7.2 Analytical formulation of Irwin's integral 34

7.3 Numerical formulation of Irwin's integral 37

8 Numerical examples 40

8.1 Off-center crack tip problem 40

8.2 Angle-cracked plate under tension problem 43

8.3 Double cantilever beam 43

8.4 L-shaped plate 45

IV The Mechanics of SWCNT Aggregates 52

9 Introduction 53

10 Computational model 56

10.1 Bonding potentials 56

10.2 Generation of randomly dispersed CNTs in the cell 57

10.3 Simulation scheme 59

11 Results and discussion 63

11.1 Comparison with MD simulations 63

11.2 Studies with increasing number of randomly dispersed CNTs at constant density 65

11.3 Studies with 800 randomly dispersed CNTs and increasing density 69

V Conclusions **70**

12 Conclusions **71**

12.1 Summary of Contributions 71

12.2 Future Work 72

VI Bibliography **74**

Bibliography **75**

VII Appendices **84**

A Extracting SERRs from Irwin's Integral **85**

A.1 Expansion of leading high order functions 85

A.2 Derivatives of high order functions used for XFEM implementation 86

A.3 Derivation of Eqs. (4.10) and (4.11) 89

A.4 Derivatives of displacement field and shape function in polar coordinates . . 93

A.5 Coefficients of Irwin's integral expansion 93

A.6 Coefficients of Irwin's integral expansion 96

A.7 Derivatives of displacement field and shape function in polar coordinates . . 110

List of Figures

3.1 A solid with a plane crack 10

3.2 Enrichment visualization of cracks in XFEM. Crack lines are illustrated in red, blue circles are jump enriched nodes and green squares are tip enriched nodes 11

4.1 Crack sliding and opening in polar coordinate system 15

4.2 Tip element illustration with crack tip at center: crack line is illustrated in red. 18

5.1 Numerical integration of Irwin's integral used to verify the analytical results in Section 4. Same color 'x' symbols indicate stress and displacement opening couples used in the integration. 23

5.2 Mode I: Single Edge Notch Tension (SENT) benchmark problem 25

5.3 Mode II example problem. 26

5.4 Mixed mode edge crack example problem: (a) geometric definition of the problem with boundary conditions (b) enriched jump and tip nodes 28

7.1 An inclined crack with tip at O'. Red solid line represents crack. P is an arbitrary point within the element under polar coordinate (r,θ). 35

7.2 Admissible integration step Δc: (a) Δc is defined as the distance to the boundary before the crack tip (b) Δc is defined as the distance to the boundary after the crack tip 38

8.1 Crack tip off the center of the tip element 41

8.2 Angle-cracked plate under uniaxial loading in opposite direction 44
8.3 K_I and K_{II} in a plate with an angled center crack. Dashed line and solid line represent exact SIFs K_I and K_{II} 45
8.4 Double cantilever beam specimen under opposite load 46
8.5 Crack extension illustration: Green colored element indicate a tip element and blue indicate an element fully cut by the crack (a) Step i: Red dashed line shows the tentative direction and extension of crack propagation at step $i+1$ determined using the proposed method (b) Step $i+1$: The kink in tip element at step i is removed by assuming a straight line segment in the element (shown in green) and the actual crack path at propagation step $i+1$ is shown by the red line. 47
8.6 Crack propagation illustration by setting initial perturbation $\theta = 15$ 48
8.7 Comparison of crack path initiated by different perturbation 49
8.8 Geometry and initial setup of the L-shaped plate example 49
8.9 Crack propagation illustration for steps 1, 7, 14 and 19 50
8.10 Computed equivalent mode I SIF K_I^{eq}. Solid red line represents the material fracture toughness below which the crack growing stops. 51

10.1 (a) Orientation of a SWCNT in axial direction. (b) Rotation and translation of a SWCNT in an arbitrary direction 58
10.2 (a) A representative computational cell with 10 (5,5) SWCNTs. (b) A representative computational cell with 200 (5,5) SWCNTs 59
10.3 Illustration of the incremental loading procedure. Dashed lines correspond to increment i and solid lines to increment i+1. The bold ends on the CNT indicate that its ends are fixed. 61

11.1 Stress-strain curve for 25-(5,5) CNTs using (a) Molecular Statics (b) Molecular Dynamics 64
11.2 stress-strain curves obtained from atomistic simulations of 50-, 200-, 800- and 1000-(5,5) armchair CNT aggregates 66

11.3 The coefficients of variance indicating the variation of the Young modulus from its average, obtained with increasing number of CNTs at constant density. 68
11.4 Young's modulus at each direction. 68
11.5 Young's modulus for different densities 69

List of Tables

5.1 Results for K_I of SENT problem 24

5.2 Results for K_{II} of pure mode II problem 27

5.3 Results for K_I of mixed mode case 29

5.4 Results for K_{II} of mixed mode case 30

8.1 Results for K_I and K_{II} of off-center pure mode problem 41

11.1 Comparison between MD simulations and the proposed molecular mechanics method for increasing number of nanotubes. The problem was run on a SiCortex parallel machine with 600 processors 65

11.2 Order parameters for 50-,200-,800-, and 1000- CNT aggregates 66

Acknowledgments

Above all I would like to express my deeply-felt thanks to my advisor, Professor Haim Waisman, for his warm encouragement and great support in the past four years. Prof. Waisman is someone you will immediately love and never forget once you meet him. His insightful guidance and broad research experience direct me into the challenging field of computational mechanics. I hope I could be as lively and energetic as him and maybe someday be able to command an audience as well as he can. I am extremely fortunate to have Prof. Issac Harari as my research advisor in XFEM. He is one of the smartest researchers I know. His ideas and suggestions offered me a great deal of assistance when my research was through slow phase. Most important, his frank and down-to-earth research attitudes as well as his unique scientific perception, serves as an inspiration in my life. My forever thanks goes to my former advisor James Guest at Johns Hopkins University and Hongzhi Zhong at Tsinghua University. I will never forget their support, generosity and kindness.

I would like to thank all committee members (Prof. Haim Waisman, Prof. Jacob Fish, Prof. George Deodatis, Prof. Jeffrey Kysar and Prof. Issac Harari) for attending my PhD thesis defense.

PhD students often talk about loneliness during the course of their study but this is something which I never experienced at Columbia. A heartfelt thanks to my supportive roommates and friends who made the Columbia experience interesting, in particular, Weizhi Shao, Tsung-Ming Liu, Xinyi Song, Zifeng Yuan, Hao Sun, Yang Liu, Nan Hu, Hao Wang, Xu Han and Ziyang Sang.

My special appreciation is reserved for my parents, Xiaolei Lan and Yusha Zhang, without whose support this work cannot be accomplished. I love them so much, and they are my source of power that sustains me all along. I am deeply thankful to my all time best

friend Bo Tu, who shares all my difficulties confronted in this long journey and make me believe my dream is achievable.

Finally, I would like to thank all faculty and staffs in the Department of Civil Engineering and Engineering Mechanics at Columbia University.

This work is dedicated to my parents
who love, encourage, and urge me all along.

Part I

Introduction

Chapter 1

Scope and Outline

This introductory chapter discusses the author's research content and an outline of this dissertation.

1.1 Introduction

In this thesis some developments made by the author in the field of computational solid mechanics are presented.

In the first part, contributions to computational fracture mechanics are made by developing a new analytical approach, within the extended Finite element (XFEM) framework to compute Strain Energy Release Rates (SERRs) directly from Irwin's integral. High order enrichment functions are derived and incorporated in the system which is shown to yield accurate results when applied to horizontal, inclined and crack propagation problems in linear elastic fracture mechanics.

In the second part of the thesis contribution to computational nanomechanics are made by developing a novel incremental constrained minimization approach to study the stress-strain behavior of short single walled carbon nanotube (SWCNT) aggregates. The aim of this research was to study the isotropic stress-strain response of SWCNT aggregates by employing molecular statics simulation.

1.2 Outline

This dissertation is organized in five parts:

Part I contains this introduction and outline.

Part II focuses on a new analytical derivation that follows directly from Irwin's integral to model straight cracks with tip located at the element center, employing with the extended finite element method. Part II consists of four chapters. In Chapter 2, a brief introduction to the XFEM is presented. In Chapter 3 the high order enrichment XFEM and the new proposed approach are introduced. Chapter 4 expands Irwin's integral analytically in terms of the XFEM, followed by several benchmark examples on 2D pure and mixed mode problems in Chapter 5. The results indicate that high order terms have significant effect when the integral limits are finite. However, when the integral limits tend to zero, the expressions are simplified as these terms vanish from the expression of SERRs, and thus have only indirect contribution via coefficients of first order terms.

Part III extends the formulation in Part II to investigate inclined cracks whose tip can be located at any point within an element. This part contains two chapters. In Chapter 6, a more general analytical approach is developed that can study crack in arbitrary settings and includes both analytical formulation and numerical implementation of of Irwin's integral. Chapter 7 contains several benchmark examples including an off-center problem, an angle-cracked problem and crack propagation problems. The proposed analytical approach does not require any special postprocessing procedures and can generate accurate results.

Part IV discusses the stress-strain behavior of short single walled carbon nanotube (SWCNT) aggregates using a novel incremental constrained minimization approach. This part consists of four chapters. In Chapter 8, a brief introduction to carbon nanotube (CNT) is presented along with a thorough literature review of computational simulation techniques to study the Young's modulus of CNTs. Chapter 9 presents the computational model developed in this work in which the atomistic potential(AIREBO) that accounts for both short and long atom interactions is introduced and, a detailed algorithm for generating randomly dispersed CNTs. Next in Chapter 10 the proposed incremental constrained minimization method is presented. The stress-strain response curves and the corresponding discussion are presented in Chapter 11.

Finally, Part V contains the summary, concluding remarks and future study. This part contains a list of the author's primary contribution in the field of computational fracture mechanics with developments in Extended Finite Element Methods for Extraction of Strain Energy Release Rates and Computational Nanomechanics for SWCNT Aggregates. Following this part is the bibliography and appendix. In the appendix the expansion of leading high order functions, derivatives of high order functions used for XFEM implementation, derivatives of displacement fields and shape functions in polar coordinates and coefficients of Irwin's integral expansion are presented.

Part II

An Analytical Method to Extract SERRs from Irwin's Integral-I

Chapter 2

Introduction & Literature Survey

Stress Intensity Factors (SIFs) or equivalently Strain Energy Release Rates (SERRs) are important quantities in linear elastic fracture mechanics, used to predict the "stress intensity" near the tip of a crack due to a remote load or residual stresses. In numerical simulations these quantities are of significant importance as they are used to determine the stability and direction of crack propagation [22; 32; 47]. Hence it is important to obtain accurate estimation of SIFs in order to predict accurate crack paths and overall response of the structure.

Several methods have been proposed in the literature to extract SIFs. These methods can be grouped as direct and indirect methods. Direct methods are the simplest methods to compute SIFs and are mainly based on correlation of crack opening displacements, obtained directly from the FE solution with analytical solutions [11; 65]. Indirect methods on the other hand, are based on integral or energy quantities to calculate SERRs and often require additional steps during the FE analysis process or a special postprocessing technique, yet they yield more accurate results [2; 42].

Some of the most well known and used indirect methods are the J-integral method [60], its domain (area) variant [42; 18; 51] and the related M-integral (or interaction integral) method [81; 76; 1]; the stiffness derivative method [55; 30]; and the virtual crack closure technique (VCCT) [62] which is inspired by Irwin's integral [34]. These methods are considered to be the cornerstone of computational fracture mechanics, receiving significant attention in the past few decades.

While Irwin's contention is extremely important from a theoretical point of view, direct implementation of the integrals in commercial software has been avoided, mainly due to numerical issues. For example, the stress fields obtained from the finite element method, whether standard or quarter point elements are employed [3], may not be sufficiently accurate due to numerical differentiation required to obtain the stress fields. In particular these errors increase close to the singularity, where Irwin's integral is valid. To this end, Rybicki and Kanninen [62] proposed the VCCT method, where they interpret Irwin's integral as the amount of work required to close the crack an amount Δc and extract the energy release rates through a penalty approach. The VCCT method has been implemented in many commercial softwares due to its simplicity and effectiveness in computing the individual components of the mixed-mode energy release rates [66; 24]. Extensive review of the method can be found in [39].

Recently, an extended finite element method (XFEM) has been proposed by Belytschko and co-workers [49; 4] for fracture problems without re-meshing. In other words, one can model cracks without the need for special conforming meshes, which imply that for crack propagation problems re-meshing may completely be avoided. The key idea of XFEM is to locally enrich the standard FE shape functions with Heaviside functions behind the crack tip to enable opening displacements, and four asymptotic functions (called branch functions) at the tip element. These branch functions are obtained from Williams analytical solution [77] and incorporate the $\sqrt{r}$ terms in the displacement field, which provides the stress singularity at the crack tip. The XFEM will be reviewed in a later chapter.

While the cracks in XFEM can be modeled without re-meshing, it is still necessary to determine the stability and direction of crack propagation. Most of the XFEM literature related to Linear Elastic Fracture Mechanics (LEFM) has focused on the computation of SIFs by the J-integral method developed by Rice [60] and its variants. A different approach that extends Parks classical stiffness derivative method [55] to XFEM, has been proposed by Waisman [74]. In that work, it was shown that the stiffness derivative can be computed in a closed form during the analysis and thus the virtual crack extension, and the error inherent in the finite difference scheme of the classical method can completely be avoided.

In this part a new analytical approach is proposed based on XFEM to compute SERRs,

reverting back to the definition of Irwin's integral. It is important to note that while the VCCT method works well for FEM, extension to XFEM is not trivial as the extraction of forces at the crack tip becomes more complicated. On the other hand, direct evaluation of Irwin's integral is straightforward with XFEM since more accurate asymptotic fields are employed to enrich the tip element, and hence closed form expressions are be obtained and so there is no need for special postprocessing.

For convenience, the derivation is carried out in polar coordinates and the integrals, which are obtained in closed form, are verified via numerical integration. Several benchmark examples on pure and mixed mode problems are studied. High order terms have also been studied by [45; 84; 83; 58]. In the interesting work of Liu *et al.* [45], the branch functions have been replaced with high order asymptotic terms, retaining not only the leading terms but also the associated coefficients. Employing this strategy the authors show that SIFs can directly be extracted without any post-processing. This approach has inspired Zamani *et al.*[84] and Réthoré *et al.* [58] to achieve high accuracy by having appropriate modifications of the enrichment scheme and employing an overlapping domain decomposition scheme.

The results indicate that high order terms have significant effect when the integral limits are finite. However, when the integral limits tend to zero, the expressions are simplified as these terms vanish from the expression of SERRs, and thus have only indirect contribution via coefficients of first order terms. The numerical results show that high accuracy can be achieved with high order enrichment terms and mesh refinement. However, the effect of the integral limits remains an open question, with finite integration intervals chosen as $h/2$ tend to give more accurate results

Chapter 3

Modeling cracks by the extended finite element method

3.1 Problem Statement

Consider a two dimensional solid with an internal crack in the domain Ω, as illustrated in Figure 3.1. The solid is subjected to body forces $\boldsymbol{b}$ in Ω, traction loading $\bar{\boldsymbol{t}}$ applied on Γ_t and displacement boundary conditions $\boldsymbol{u} = \bar{\boldsymbol{u}}$ on Γ_u. In cartesian coordinates, the displacement field is decomposed into its components $\boldsymbol{u} = \{u_x, u_y\}$ as illustrated. Additionally, the crack is defined by internal boundaries Γ_c, which are assumed to be traction free.

The Galerkin approximation of the proposed problem is to seek a kinematically admissible displacement field $\boldsymbol{u}^h \in \mathcal{U}^h$, which is a finite-dimensional subspace of the solution space $\mathcal{U}$, such that

$$\int_\Omega \boldsymbol{\epsilon}(\boldsymbol{u}^h) : \boldsymbol{C} : \boldsymbol{\epsilon}(\boldsymbol{w}^h)\,\mathrm{d}\Omega = \int_\Omega \boldsymbol{b}\cdot\boldsymbol{w}^h\,\mathrm{d}\Omega + \int_{\Gamma_t} \bar{\boldsymbol{t}}\cdot\boldsymbol{w}^h\,\mathrm{d}\Gamma \qquad \forall \boldsymbol{w}^h \in \mathcal{U}_0^h \tag{3.1}$$

where $\boldsymbol{\epsilon}$ and $\boldsymbol{C}$ are the standard strain and elasticity tensors. The weighting functions $\boldsymbol{w}^h$, whose values vanish on the Dirichlet boundary Γ_u, belong to the finite-dimensional subspace $\mathcal{U}_0^h$.

The aim of this work is to compute the Strain Energy Release Rates (SERRs) directly from Irwin's integral, by employing the extended finite element method with high order crack tip asymptotic functions. These functions allow for the evaluation of the integral

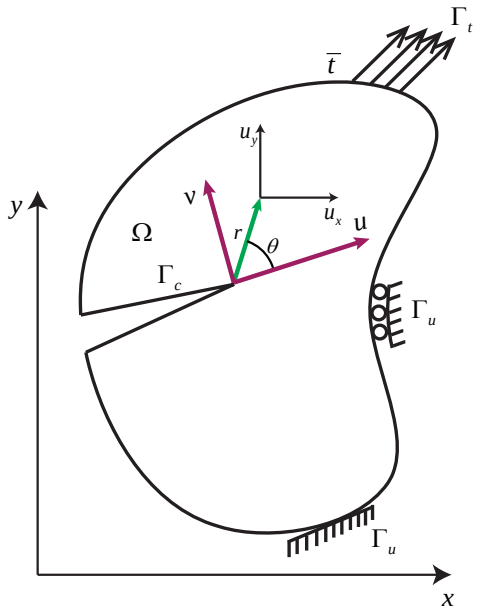

Figure 3.1: A solid with a plane crack

quantities in closed form and would therefore result in an accurate and efficient method.

3.2 XFEM overview

The key idea of XFEM is to locally enrich the standard finite element approximation with local partitions of unity enrichment functions which are chosen according to the physics of the problem at hand. It follows that for crack problems, the mesh is independent of the crack orientation [49; 4; 70]. An excellent review on the XFEM can be found in [6; 26]. Similar enrichment methods for modeling cracks are based on the generalized finite element method [20; 21].

Let $\boldsymbol{u}^h \in \mathcal{U}^h$ be an extended finite element approximation to the descretized weak form of elasticity, where $\mathcal{U}^h$ is the appropriate Sobolev space [31]. The XFEM enriches the conventional shape function space with a set of functions $H(\boldsymbol{x})$ and $F_j\left(\boldsymbol{x}(r,\theta)\right)$, such that

$$\boldsymbol{u}^h(\boldsymbol{x}) = \sum_{I=1}^{n} N_I(\boldsymbol{x})\boldsymbol{u}_I + \sum_{I=1}^{n_J} N_I(\boldsymbol{x})H(\boldsymbol{x})\boldsymbol{a}_I + \sum_{I=1}^{n_T}\left[N_I(\boldsymbol{x})\sum_{j=1}^{n_F} F_j\left(\boldsymbol{x}(r,\theta)\right)\boldsymbol{b}_{jI}\right] \tag{3.2}$$

where $\boldsymbol{x} = \{x, y\}^T$ are the spatial coordinates. n, n_J, n_T and n_F are the number of total nodal points, jump-enriched nodes, tip-enriched nodes and number of enrichment functions,

respectively. $N_I(\boldsymbol{x})$ are the standard finite element shape functions associated with standard degrees of freedom $\boldsymbol{u}_I$, whereas $\boldsymbol{a}_I$ and $\boldsymbol{b}_{jI}$ are the degrees of freedom associated with the enriched nodes. Typically, for linear elastic fracture problems, the crack tip zone is enriched with the classical analytical solution for the near tip field [77], and only the $\sqrt{r}$ terms, which are given in Eq. (3.10), are employed. Note that these functions are given in polar coordinates (r, θ), which is illustrated in Figure 3.1. Element nodes (behind the crack tip) which are fully cut by the crack are enriched with the Heaviside function

$$H(\boldsymbol{x}) = \begin{cases} +1 & \text{above } \Gamma_c^+ \\ -1 & \text{below } \Gamma_c^- \end{cases} \tag{3.3}$$

where Γ_c^+ and Γ_c^- defines the edges of the discontinuity line that splits the element into two parts. Note that the $\sqrt{r}$ term in the displacement field is directly built into the equations and hence the stress singularity of $\frac{1}{\sqrt{r}}$ appears in the solution. The enriched nodes of inclined 2D cracks are illustrated in Figure 3.2.

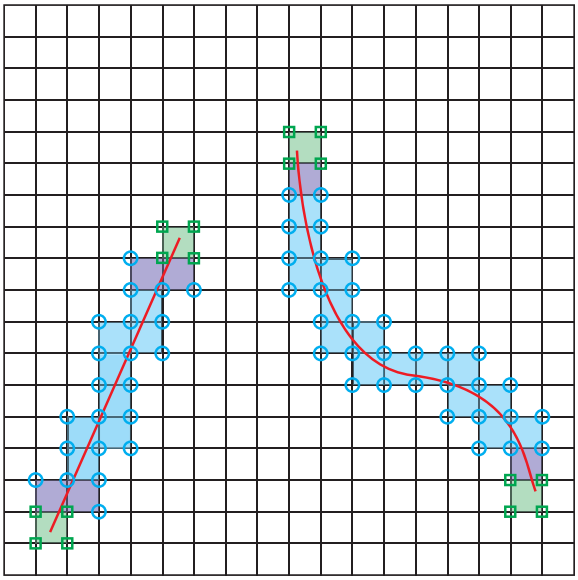

Figure 3.2: Enrichment visualization of cracks in XFEM. Crack lines are illustrated in red, blue circles are jump enriched nodes and green squares are tip enriched nodes

Typically, these enriched nodes (and the corresponding elements) are easily obtained with the levelset functions. These function represent discontinuities and boundaries implic-

itly, however they have been found very useful and in particular problems involving moving boundaries are easily handled by the levelset method [53; 64]. In the context of finite elements, this approach has been found very useful as information of the crack geometry is only stored as additional nodal variables and then interpolated to gauss (integration) points employing standard shape functions. It is also straight forward to update this data during crack propagation. Moreover, the levelset approach allows an automatic detection of enriched nodes and the representation of the enrichment functions in Eq. (3.2) by means of levelset values. For crack problems one defines two levelset functions Ψ and Φ which are simply the distance in local crack coordinate system from any point to the crack front and crack surface, respectively. Thus the angle θ and distance r given in Eq. (3.14), are obtained by

$$r = \sqrt{\Psi^2 + \Phi^2} \qquad \text{and} \qquad \theta = \tan^{-1}\left(\frac{\Phi}{\Psi}\right) \tag{3.4}$$

For more details the reader is referred to [70; 50].

3.3 High order enrichment functions

For traction-free cracks in local crack coordinates (see Figure 3.1), the asymptotic fields for the displacement components u and v near the crack tip are given by Williams [77], as

$$\begin{aligned} u(r,\theta) =& \sum_{i=1}^{\infty} \frac{r^{i/2}}{2\mu n\sqrt{2\pi}}\{K_{Ii}[(\kappa + \frac{i}{2} + (-1)^i)\cos\frac{i}{2}\theta - \frac{i}{2}\cos(\frac{i}{2}-2)\theta] \\ &+K_{IIi}[(\kappa + \frac{i}{2} - (-1)^i)\sin\frac{i}{2}\theta - \frac{i}{2}\sin(\frac{i}{2}-2)\theta]\} \end{aligned} \tag{3.5}$$

$$\begin{aligned} v(r,\theta) =& \sum_{i=1}^{\infty} \frac{r^{i/2}}{2\mu i\sqrt{2\pi}}\{K_{Ii}[(\kappa - \frac{i}{2} - (-1)^i)\sin\frac{i}{2}\theta + \frac{i}{2}\sin(\frac{i}{2}-2)\theta] \\ &+K_{IIi}[(-\kappa + \frac{i}{2} - (-1)^i)\cos\frac{i}{2}\theta - \frac{i}{2}\cos(\frac{i}{2}-2)\theta]\} \end{aligned} \tag{3.6}$$

where K_{Ii} and K_{IIi} are coefficients, μ and κ are shear modulus and Kolosov constant, respectively. The Kolosov constant is defined as

$$\kappa = \begin{cases} 3 - 4\nu, & \text{plane strain} \\ \dfrac{3-\nu}{1+\nu}, & \text{plane stress} \end{cases} \tag{3.7}$$

where ν is Poisson ratio.

The expressions in Eqs. (3.5) and (3.6) may be simplified as

$$u(r,\theta) = \sum_{i=1}^{4} u_i(r^{i/2},\theta) + O(r^{5/2}) \tag{3.8}$$

$$v(r,\theta) = \sum_{i=1}^{4} v_i(r^{i/2},\theta) + O(r^{5/2}) \tag{3.9}$$

where the coefficients $u_1, ..., u_4$ and $v_1, ..., v_4$ in Eqs. (3.8) and (3.9) are given in Appendix A.1.

As opposed to [45],the high order terms are incorporated in a traditional XFEM fashion, considering only the space spanned by high order terms. See Appendix A.2 for the complete derivation. Thus the enrichment functions for different orders of r are

$$\sqrt{r}: \qquad \mathbf{F}^1 = \{\sqrt{r}\sin\frac{\theta}{2}, \sqrt{r}\cos\frac{\theta}{2}, \sqrt{r}\sin\theta\sin\frac{\theta}{2}, \sqrt{r}\sin\theta\cos\frac{\theta}{2}\} \tag{3.10}$$

$$r: \qquad \mathbf{F}^2 = \{r\cos\theta, r\sin\theta\} \tag{3.11}$$

$$r^{3/2}: \qquad \mathbf{F}^3 = \{r^{3/2}\cos\frac{\theta}{2}, r^{3/2}\sin\frac{\theta}{2}, r^{3/2}\sin\theta\sin\frac{\theta}{2}, r^{3/2}\sin\theta\cos\frac{\theta}{2}\} \tag{3.12}$$

$$r^2: \qquad \mathbf{F}^4 = \{r^2, r^2\sin 2\theta, r^2\cos 2\theta\} \tag{3.13}$$

and the full set of enrichments, with thirteen terms, used in analysis is therefore

$$\mathbf{F}(r,\theta) = \{\mathbf{F}^1, \mathbf{F}^2, \mathbf{F}^3, \mathbf{F}^4\} \tag{3.14}$$

Chapter 4

Extraction of Strain Energy Release Rates using Irwin's integral and XFEM

4.1 Analytical expansion of Irwin's integral

According to Irwin [34], the work required to extend a crack by an infinitesimal distance Δc is equal to the work required to close the crack to its original length. Thus, the Strain Energy Release Rate for a mixed mode state, expressed in a polar coordinate system (r, θ) with the origin at the crack tip, is defined by

$$\mathcal{G} = \mathcal{G}_I + \mathcal{G}_{II} \tag{4.1}$$

where $\mathcal{G}$ is the total energy release rate, additively decomposed into individual components $\mathcal{G}_I$ and $\mathcal{G}_{II}$ due to Mode I and Mode II deformations

$$\mathcal{G}_I = \lim_{\Delta c \to +0} \frac{1}{2\Delta c} \int_0^{\Delta c} \sigma_{\theta\theta}(\Delta c - r, 0) \bar{u}_\theta(r) \mathrm{d}r \tag{4.2}$$

$$\mathcal{G}_{II} = \lim_{\Delta c \to +0} \frac{1}{2\Delta c} \int_0^{\Delta c} \sigma_{r\theta}(\Delta c - r, 0) \bar{u}_r(r) \mathrm{d}r \tag{4.3}$$

$\sigma_{\theta\theta}$ and $\sigma_{r\theta}$ are the normal and shear stresses in polar coordinates, $\bar{u}_r$ and $\bar{u}_\theta$ are relative sliding and opening displacements between corresponding points on crack surfaces and Δc is the crack extension at the crack tip. The sliding and opening displacement jumps are defined by

$$\overline{u}_r(r) = u_r(r, -\pi) - u_r(r, \pi) \tag{4.4}$$

$$\overline{u}_\theta(r) = u_\theta(r, -\pi) - u_\theta(r, \pi) \tag{4.5}$$

The transformation of displacement fields from polar coordinates to cartesian coordinates is given as

$$u_r = u\cos\theta + v\sin\theta \tag{4.6}$$

$$u_\theta = -u\sin\theta + v\cos\theta \tag{4.7}$$

$\overline{u}_r(r)$ and $\overline{u}_\theta(r)$ represent the crack sliding and opening in polar coordinate system, which is illustrated in Fig. 4.1.

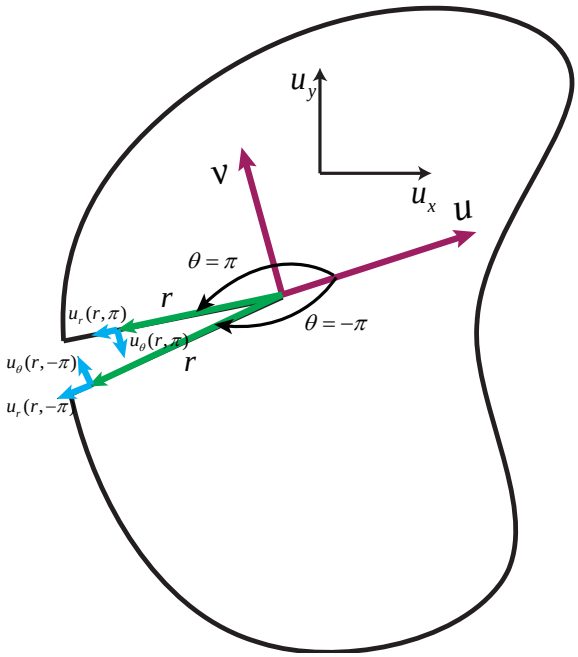

Figure 4.1: Crack sliding and opening in polar coordinate system

Thus, under the assumption that the local crack coordinate system is aligned with the crack axis (see Figure 3.1), the relations are simplified and the sliding and opening

displacement jumps, Eq. (4.4)–(4.5), become

$$\overline{u}_r(r) = u\,(r,\pi) - u\,(r,-\pi) \tag{4.8}$$

$$\overline{u}_\theta(r) = v\,(r,\pi) - v\,(r,-\pi) \tag{4.9}$$

Plugging Williams expansion, Eqs. (3.5)–(3.6), into Eqs. (4.4)–(4.5), retaining only the first three leading terms, yields

$$\overline{u}_r(r) = \sum_{i=1}^{\infty} u_i(r^{i/2},\pi) - \sum_{i=1}^{\infty} u_i(r^{i/2},-\pi) = \sum_{i=1}^{3} m_i^{II} r^{\frac{2i-1}{2}} + \mathrm{O}\big(r^{\frac{7}{2}}\big) \tag{4.10}$$

$$\overline{u}_\theta(r) = \sum_{i=1}^{\infty} v_i(r^{i/2},\pi) - \sum_{i=1}^{\infty} v_i(r^{i/2},-\pi) = \sum_{i=1}^{3} m_i^{I} r^{\frac{2i-1}{2}} + \mathrm{O}\big(r^{\frac{7}{2}}\big) \tag{4.11}$$

More details on the expansion of the terms in Eqs. (4.10) and (4.11) are shown in Appendix A.3. Note that even order terms of r in the expansion of the displacement jump vanish from the sum as these terms are continuous across the discontinuity, hence only odd order terms appear in the derivation in Eqs. (4.10) and (4.11). Also, note that the resulting sum is truncated after the order of $r^{5/2}$ appear in the formulation. To clarify, this is due to the choice of high order enrichment functions (see Eq. (3.14)) and considering the XFEM formulation given in Section 4.2.

The kinematic strain-displacement in polar coordinates are defined as

$$\epsilon_{rr} = \frac{\partial u_r}{\partial r} \tag{4.12}$$

$$\epsilon_{\theta\theta} = \frac{u_r}{r} + \frac{1}{r}\frac{\partial u_\theta}{\partial \theta} \tag{4.13}$$

$$\epsilon_{r\theta} = \frac{1}{2}\Big(\frac{1}{r}\frac{\partial u_r}{\partial \theta} + \frac{\partial u_\theta}{\partial r} - \frac{u_\theta}{r}\Big) \tag{4.14}$$

where $\epsilon_{rr}, \epsilon_{\theta\theta}$ and $\epsilon_{r\theta}$ are the radial, tangential and shear strain, respectively. Considering a plane strain state, the stresses $\sigma_{\theta\theta}$ and $\sigma_{r\theta}$ are given as

$$\sigma_{\theta\theta} = \frac{E}{(1+\nu)(1-2\nu)}(\nu\epsilon_{rr} + (1-\nu)\epsilon_{\theta\theta}) \tag{4.15}$$

$$\sigma_{r\theta} = \frac{E}{(1+\nu)}\epsilon_{r\theta} \tag{4.16}$$

Combining the stresses with strains, Eqs. (4.12)–(4.15) and plugging in Williams solutions, Eqs. (3.5)–(3.6), the definition of normal and shear stresses ahead of the crack tip can be

expressed as

$$\sigma_{\theta\theta}(r,0) = \frac{E}{(1+\nu)(1-2\nu)} \sum_{i=4}^{11} m_i^I r^{\frac{i-5}{2}} + \mathrm{O}\big(r^{\frac{7}{2}}\big) \tag{4.17}$$

$$\sigma_{r\theta}(r,0) = \frac{E}{2(1+\nu)} \sum_{i=4}^{11} m_i^{II} r^{\frac{i-5}{2}} + \mathrm{O}\big(r^{\frac{7}{2}}\big) \tag{4.18}$$

Note that all orders of r in Eqs. (4.17) and (4.18) are preserved in the derivation of the stresses (as opposed to the derivation of displacement jump in Eqs. (4.10) and (4.11). However, the sum is truncated after r^3 which again is due to the choice of high order enrichment functions (see Eq. (3.14)) and considering the XFEM formulation given in Section 4.2 and shape functions are introduced (see Eq. (4.29)).

Finally, substituting the opening displacements in Eq. (4.10)–(4.11) and stresses in Eqs. (4.17)–(4.18) into the definition of Strain Energy Release Rate, $\mathcal{G}_I$ in Eq. (4.21) and $\mathcal{G}_{II}$ in Eq. (4.22) and integrating arrive at

$$\widetilde{\mathcal{G}}_I(\Delta c) = \frac{E}{(1+\nu)(1-2\nu)} \sum_{i=0}^{11} \alpha_i^I \Delta c^{\frac{i}{2}} + \mathrm{O}\big(\Delta c^6\big) \tag{4.19}$$

and

$$\widetilde{\mathcal{G}}_{II}(\Delta c) = \frac{E}{2(1+\nu)} \sum_{i=0}^{11} \alpha_i^{II} \Delta c^{\frac{i}{2}} + \mathrm{O}\big(\Delta c^6\big) \tag{4.20}$$

Here $\widetilde{\mathcal{G}}_I$ and $\widetilde{\mathcal{G}}_{II}$ have been defined as

$$\widetilde{\mathcal{G}_I} = \frac{1}{2\Delta c} \int_0^{\Delta c} \sigma_{\theta\theta}(\Delta c - r, 0) \bar{u}_\theta(r) \mathrm{d}r \tag{4.21}$$

$$\widetilde{\mathcal{G}_{II}} = \frac{1}{2\Delta c} \int_0^{\Delta c} \sigma_{r\theta}(\Delta c - r, 0) \bar{u}_r(r) \mathrm{d}r \tag{4.22}$$

so that

$$\mathcal{G}_I = \lim_{\Delta c \to +0} \widetilde{\mathcal{G}}_I(\Delta c) \tag{4.23}$$

$$\mathcal{G}_{II} = \lim_{\Delta c \to +0} \widetilde{\mathcal{G}}_{II}(\Delta c) \tag{4.24}$$

The coefficients α_i^I and α_i^{II} are listed in Appendix A.5.

A simple expression is obtained in the limit when $\Delta c \to 0$ since all high order terms vanish, i.e.

$$\widetilde{\mathcal{G}}_I(\Delta c = 0) = \frac{E}{(1+\nu)(1-2\nu)}\alpha_0^I = \frac{E}{(1+\nu)(1-2\nu)}\frac{\pi}{4}m_1^I m_4^I \tag{4.25}$$

$$\widetilde{\mathcal{G}}_{II}(\Delta c = 0) = \frac{E}{2(1+\nu)}\alpha_0^{II} = \frac{E}{2(1+\nu)}\frac{\pi}{4}m_1^{II} m_4^{II} \tag{4.26}$$

The goal is to find the coefficients α_i^I and α_i^{II} analytically, using the enrichment functions in XFEM.

4.2 XFEM realization of Irwin's integral

To obtain expressions for the coefficients α_i^I and α_i^{II}, consider a generic rectangular element with a horizontal crack and tip at the center of the element, as shown in Figure 4.2. In polar coordinates, any point in the element domain is defined by

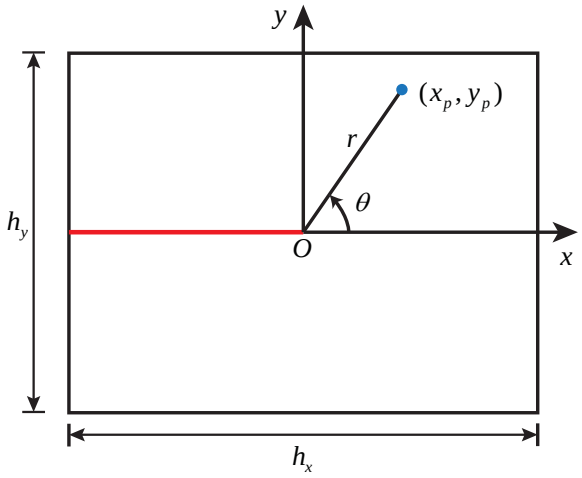

Figure 4.2: Tip element illustration with crack tip at center: crack line is illustrated in red.

$$x_p = r\cos\theta \qquad\qquad y_p = r\sin\theta \tag{4.27}$$

The nodal coordinates of the element are therefore $(x_I, y_I), x_I = \pm h_x/2, y_I = \pm h_y/2, I = 1, ..., 4$, where h_x and h_y are the length of the edges in x- and y- directions, respectively.

Tip elements in XFEM consider near tip asymptotic fields, and hence the displacement

field in Eq. (3.2) may be simplified and written in polar coordinates as

$$\boldsymbol{u}(r,\theta) = \sum_{I=1}^{4} N_I(\boldsymbol{u}_I + \sum_{j=1}^{n_F} F_j \boldsymbol{b}_{jI}) \tag{4.28}$$

In polar coordinates, the standard linear shape functions are

$$N_I(r,\theta) = \frac{1}{4}(1+4\frac{x_I r\cos\theta}{h_x^2})(1+4\frac{y_I r\sin\theta}{h_y^2}) \qquad I=1,...,4 \tag{4.29}$$

and the derivatives of the displacement field $\frac{\partial \boldsymbol{u}}{\partial r}$, $\frac{\partial \boldsymbol{u}}{\partial \theta}$ and shape functions $\frac{\partial N_I}{\partial r}$, $\frac{\partial N_I}{\partial \theta}$ are given in Appendix A.4.

Assuming a general case where all enrichment functions, including high order functions in Eq. (3.14), are used to enrich the solution space (i.e. $n_F = 13$), substituting Eqs. (4.28)–(4.29) into Eqs. (4.4)–(4.5) arrives at

$$\begin{aligned}\overline{u}_r(r) &= \sum_{I=1}^{4} N_I(r,\pi)(u_{xI} + \sum_{j=1}^{13} F_j(r,\pi)b_{xjI}) - \sum_{I=1}^{4} N_I(r,-\pi)(u_{xI} + \sum_{j=1}^{13} F_j(r,-\pi)b_{xjI}) \\ &= \sum_{I=1}^{4} \frac{1}{4}(1-4\frac{x_I r}{h_x^2})(2\sqrt{r}b_{x1I} + 2r^{\frac{3}{2}}b_{x8I})\end{aligned} \tag{4.30}$$

and

$$\begin{aligned}\overline{u}_\theta(r) &= \sum_{I=1}^{4} N_I(r,\pi)(u_{yI} + \sum_{j=1}^{13} F_j(r,\pi)b_{yjI}) - \sum_{I=1}^{4} N_I(r,-\pi)(u_{yI} + \sum_{j=1}^{13} F_j(r,-\pi)b_{yjI}) \\ &= \sum_{I=1}^{4} \frac{1}{4}(1-4\frac{x_I r}{h_x^2})(2\sqrt{r}b_{y1I} + 2r^{\frac{3}{2}}b_{y8I})\end{aligned} \tag{4.31}$$

Similarly, the stress $\sigma_{\theta\theta}(r,0)$ is obtained by plugging Eqs. (A.24)–(A.27) into Eqs. (4.17)–(4.18) and using the derivatives of the enrichment function in Eqs. (A.10)–(A.11), gives the expressions

$$\begin{aligned}\sigma_{\theta\theta}(r,0) &= \frac{E\nu}{(1+\nu)(1-2\nu)}(\sum_{I=1}^{4}\frac{x_I}{h_x^2}(u_{xI} + \sqrt{r}b_{x2I} + rb_{x5I} + r^{\frac{3}{2}}b_{x7I} + r^2(b_{x11I} + b_{x13I})) \\ &+ \sum_{I=1}^{4}\frac{1}{4}(1+4\frac{x_I r}{h_x^2})(\frac{1}{2\sqrt{r}}b_{x2I} + b_{x5I} + \frac{3}{2}\sqrt{r}b_{x7I} + 2r(b_{x11I} + b_{x13I}))) \\ &+ \frac{E(1-\nu)}{(1+\nu)(1-2\nu)}(\frac{1}{r}\sum_{I=1}^{4}(\frac{\left(h_x^2 + 4\,x_I r\right)y_I r}{h_x^2 h_y^2})(u_{yI} + \sqrt{r}b_{y2I} + rb_{y5I} + r^{\frac{3}{2}}b_{y7I} + r^2(b_{y11I} + b_{y13I})) \\ &+ \frac{1}{r}\sum_{I=1}^{4}\frac{1}{4}(1+4\frac{x_I r}{h_x^2})(\sqrt{r}(\frac{1}{2}b_{y1I} + b_{y4I}) + rb_{y6I} + r^{\frac{3}{2}}(\frac{1}{2}b_{y8I} + b_{y10I}) + 2r^2 b_{y12I}))\end{aligned} \tag{4.32}$$

and similarly the stress $\sigma_{r\theta}(r,0)$

$$\sigma_{r\theta}(r,0) = \frac{E}{2(1+\nu)}(\frac{1}{r}\sum_{I=1}^{4}(\frac{\left(h_x^2+4\,x_I r\right)y_I r}{h_x^2 h_y^2})(u_{xI}+\sqrt{r}b_{x2I}+rb_{x5I}+r^{\frac{3}{2}}b_{x7I}+r^2(b_{x11I}+b_{x13I}))$$
$$+\frac{1}{r}\sum_{I=1}^{4}\frac{1}{4}(1+4\frac{x_I r}{h_x^2})(\sqrt{r}(\frac{1}{2}b_{x1I}+b_{x4I})+rb_{x6I}+r^{\frac{3}{2}}(\frac{1}{2}b_{x8I}+b_{x10I})+2r^2 b_{x12I})$$
$$+\sum_{I=1}^{4}\frac{x_I}{h_x^2}(u_{yI}+\sqrt{r}b_{y2I}+rb_{y5I}+r^{\frac{3}{2}}b_{y7I}+r^2(b_{y11I}+b_{y13I}))$$
$$+\sum_{I=1}^{4}\frac{1}{4}(1+4\frac{x_I r}{h_x^2})(\frac{1}{2\sqrt{r}}b_{y2I}+b_{y5I}+\frac{3}{2}\sqrt{r}b_{y7I}+2r(b_{y11I}+b_{y13I}))) \tag{4.33}$$

The final step is to match all coefficients of leading order terms for opening displacement jumps in Eq. (4.30) with (4.10) and Eq. (4.31) with (4.11). Similarly, the coefficients for stresses in Eqs. (4.32)–(4.33) are matched with those in (4.17)–(4.18). These constants are listed in Appendix A.5. Finally, the general solution for Strain Energy Release Rates with finite integration limits is obtained in closed form.

In the special case of $\Delta c \to 0$, high order terms vanish and only constants m_1^I, m_4^I and m_1^{II}, m_4^{II} remain. These are given as

$$m_1^I = \sum_{I=1}^{4}\frac{1}{2}b_{y1I} \qquad\qquad m_1^{II} = \sum_{I=1}^{4}\frac{1}{2}b_{x1I} \tag{4.34}$$

and

$$m_4^I = \nu\sum_{I=1}^{4}\frac{b_{x2I}}{8}+(1-\nu)\sum_{I=1}^{4}(\frac{b_{y1I}}{8}+\frac{b_{y4I}}{4}) \tag{4.35}$$

$$m_4^{II} = \sum_{I=1}^{4}(\frac{b_{x1I}}{8}+\frac{b_{x4I}}{4}+\frac{b_{y2I}}{8}) \tag{4.36}$$

where the coefficients b_{xj} and b_{yj} are obtained from the solution of the algebraic system of equations. Thus the Strain Energy Release Rates (SERRs) can be computed in close form and obtained directly without the need for special postprocessing techniques, and is given

by

$$\widetilde{\mathcal{G}}_I(\Delta c=0)=\frac{\pi}{4}\frac{E}{(1+\nu)(1-2\nu)}(\nu\sum_{I=1}^{4}\frac{b_{x2I}}{8}\sum_{I=1}^{4}\frac{1}{2}b_{y1I}+(1-\nu)\sum_{I=1}^{4}(\frac{b_{y1I}}{8}+\frac{b_{y4I}}{4})\sum_{I=1}^{4}\frac{1}{2}b_{y1I}) \tag{4.37}$$

$$\widetilde{\mathcal{G}}_{II}(\Delta c=0)=\frac{\pi}{4}\frac{E}{2(1+\nu)}(\sum_{I=1}^{4}\frac{1}{2}b_{x1I}\sum_{I=1}^{4}(\frac{b_{x1I}}{8}+\frac{b_{x4I}}{4}+\frac{b_{y2I}}{8})) \tag{4.38}$$

Although the SERRs computation with Δc equal to 0, as in Eqs. (4.37) and (4.38), does not depend directly on the degrees-of-freedom of the higher-order asymptotic functions, these functions effect the coefficients of the branch functions, and hence the computation of the SERRs.

In Section 5 results are presented for both $\Delta c=0$ and $\Delta c=\frac{h_x}{2}$. Stress Intensity Factors (SIF)s are related to SERRs and can directly be obtained by [62]

$$K_I=\sqrt{\frac{\mathcal{G}_1 E}{\gamma}} \qquad\qquad K_{II}=\sqrt{\frac{\mathcal{G}_2 E}{\gamma}} \tag{4.39}$$

where

$$\gamma=\begin{cases}1-\nu^2, & \text{plane strain}\\ 1, & \text{plane stress}\end{cases} \tag{4.40}$$

and E is the Young modulus.

Chapter 5

Numerical examples

The proposed approach is studied on a Mode I: Single Edge Notch Tension (SENT) panel problem, a Mode II problem and a Mixed Mode benchmark problem. All numerical examples shown in this section are plane strain problems. To alleviate computational issues related to tip element integration, the trapezoidal integration rule is used with 200×200 equally spaced quadrature points for computation of element stiffness matrix. One of the future directions will investigate better quadrature rules and other specialized methods to handle the tip element with the singularity.

The SERRs are computed using the Irwin's integral. In all examples the effect of high order terms, mesh refinement and the effect of integration interval Δc are considered. In particular: (i) integration step of $\Delta c = 0$, computed by Eqs. (4.37) and (4.38) and (ii) integration step of $\Delta c = \frac{h_x}{2}$, computed by Eqs. via (4.19) and (4.20).

All results related to the derivation in Section 4 have been verified by numerical integration (1D Gauss Quadrature rule) of Irwin's integral, as shown in Fig. 5.1. Stress points in front of the crack tip and the corresponding displacement opening behind the tip have been computed numerically by the following approximation

$$\widetilde{\mathcal{G}}_I(\Delta c) = \frac{1}{2\Delta c}\int_0^{\Delta c} \sigma_{\theta\theta}(\Delta c - r, 0)\bar{u}_\theta(r)\mathrm{d}r \approx \frac{1}{2\Delta c}\sum_{i=1}^{n_{gp}} w_i \sigma_{\theta\theta}(\Delta c - r_i^*, 0)\bar{u}_\theta(r_i^*) \tag{5.1}$$

$$\widetilde{\mathcal{G}}_{II}(\Delta c) = \frac{1}{2\Delta c}\int_0^{\Delta c} \sigma_{r\theta}(\Delta c - r, 0)\bar{u}_r(r)\mathrm{d}r \approx \frac{1}{2\Delta c}\sum_{i=1}^{n_{gp}} w_i \sigma_{r\theta}(\Delta c - r_i^*, 0)\bar{u}_r(r_i^*) \tag{5.2}$$

where n_{gp} is the number of Gauss quadrature points, r_i^* are the Gauss point coordinates and

w_i are the weights associated with the integration rule. The pairs of stress and displacement opening used in Eq. (5.1) and (5.2) to compute SERRs are illustrated by the same color 'x'-symbol in Fig. 5.1. The analytical derivation in Section 4 is verified and it is in excellent agreement with the numerical integration.

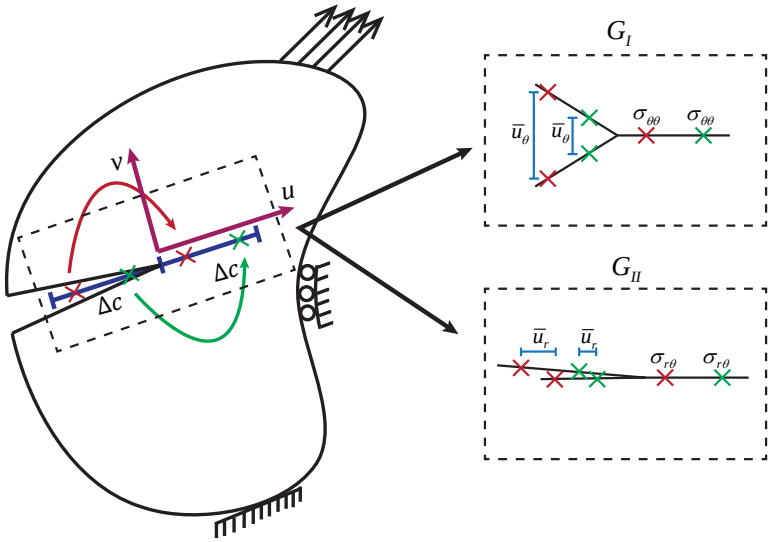

Figure 5.1: Numerical integration of Irwin's integral used to verify the analytical results in Section 4. Same color 'x' symbols indicate stress and displacement opening couples used in the integration.

5.1 Mode I: Single Edge Notch Tension (SENT) problem

First consider a Mode I problem: a single edge notch tension panel [23]. The problem studied consists of an edge crack of length a in a rectangular domain with dimensions $h \times W$ under 1 unit traction force on its upper and bottom edges in opposite direction, as shown in Figure 5.2. Young's modulus and Poisson's ratio are taken as, $E = 10^7$ and $\nu = 0.3$, respectively. The dimension h/W is set equal to 2 and a/W is set equal to 1/2. For this benchmark problem, K_I can be expressed as [23]

$$K_I = [1.12 - 0.23(\frac{a}{W}) + 10.56(\frac{a}{W})^2 - 21.74(\frac{a}{W})^3 + 30.42(\frac{a}{W})^4]\sqrt{\pi a} \tag{5.3}$$

The computed results are summarized in Table 5.1. It can be seen from the table that

Table 5.1: Results for K_I of SENT problem

Order	Mesh	$K_I(\Delta c = 0)$	Relative Error	$K_I(\Delta c = h_x/2)$	Relative Error
1/2	9×19	5.891	47.45%	8.128	27.50%
	19×39	6.127	45.35%	8.474	24.42%
	29×59	6.201	44.69%	8.577	23.49%
	39×79	6.237	44.37%	8.627	23.05%
1	9×19	10.406	7.18%	10.216	8.88%
	19×39	10.659	4.93%	10.478	6.54%
	29×59	10.729	4.30%	10.552	5.88%
	39×79	10.762	4.01%	10.587	5.57%
3/2	9×19	10.459	6.71%	10.834	3.37%
	19×39	10.639	5.10%	11.009	1.81%
	29×59	10.699	4.57%	11.060	1.35%
	39×79	10.728	4.31%	11.084	1.13%
2	9×19	10.490	6.43%	10.871	3.04%
	19×39	10.684	4.71%	11.029	1.63%
	29×59	10.740	4.20%	11.075	1.22%
	39×79	10.767	3.97%	11.096	1.03%
J-integral	9×19	10.446	6.83%		
	19×39	10.862	3.11%		
	29×59	10.984	2.03%		
	39×79	11.041	1.52%		

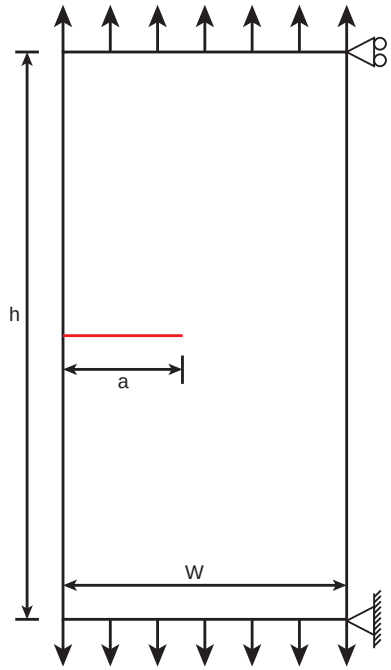

Figure 5.2: Mode I: Single Edge Notch Tension (SENT) benchmark problem

the proposed approach yields convergent results with higher order enrichment at the tip element. Setting $\Delta c = h_x/2$ generally produces more accurate results while setting $\Delta c = 0$ results in computational simplicity. Nonetheless, both methods compute the SIFs in closed form and no special postprocessing is required. The accuracy of proposed approach with order of 3/2 is in line with J-integral method while higher order r^2 performs slightly better.

5.2 Mode II example

A Mode II example shown in Fig. 5.3 is studied. The problem consists of a square domain with $h = W = 10$ units, with $a/W = 1/2$ under $p = 1$ unit traction load on its left edge. Young's modulus and Poisson's ratios are taken as $E = 10^7$ and $\nu = 0.3$. The traction force acts in opposite directions, as indicated in the Figure to force Mode II sliding deformation. No analytical results are available for this problem, hence the J-integral method with a very fine mesh (99×99) is used as the reference solution, which gives

$$K_{II} = 1.244 \tag{5.4}$$

The results are summarized in Table 5.2. It is interesting to note that for this example the

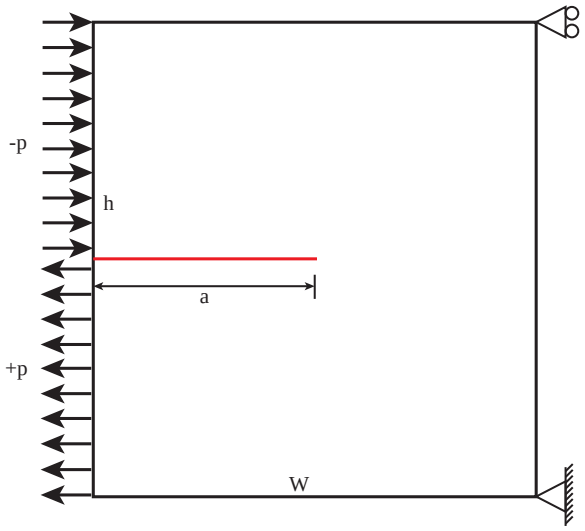

Figure 5.3: Mode II example problem.

choice of $\Delta c = 0$ provides the most accurate results. Similar to Example 5.1, the proposed approach with order of 3/2 provides comparable accuracy with J-integral method while higher order r^2 performs slightly better.

5.3 Mixed mode benchmark problem

The proposed approach is studied on a benchmark mixed mode problem [45; 79]. The problem considered consists of a rectangular domain with dimensions 7×16 units subjected to a unit stress shear traction on its upper edge and is fixed on the bottom, as shown in Figure 5.4(a). The crack length is 3.5 units and the enriched jump and tip nodes are illustrated in Figure 5.4(b). The stress intensity factors K_I and K_{II} are computed using proposed approach. Young's modulus and Poisson's ratio are taken as $E = 3 \times 10^7$ and $\nu = 0.25$.

The analytical solution for this problem, given in [45; 79], is:

$$K_I = 34.00; \qquad K_{II} = 4.55 \tag{5.5}$$

Table 5.3 and 5.3 present numerical results for Mode I and Mode II, respectively. The most significant improvement in accuracy is observed when adding order r terms to the

Table 5.2: Results for K_{II} of pure mode II problem

Order	Mesh	$K_{II}(\Delta c = 0)$	Relative Error	$K_{II}(\Delta c = h_x/2)$	Relative Error
1/2	9×9	0.593	52.3%	0.662	46.8%
	19×19	0.768	38.3%	0.854	31.4%
	29×29	0.826	33.6%	0.919	26.1%
	39×39	0.855	31.3%	0.952	23.5%
1	9×9	0.758	39.1%	0.768	38.3%
	19×19	0.974	21.7%	0.981	21.1%
	29×29	1.047	15.9%	1.054	15.3%
	39×39	1.083	12.9%	1.090	12.4%
3/2	9×9	0.820	34.1%	0.820	34.1%
	19×19	1.061	14.8%	1.056	15.1%
	29×29	1.140	8.4%	1.134	8.8%
	39×39	1.179	5.3%	1.173	5.7%
2	9×9	0.846	32.0%	0.825	33.7%
	19×19	1.080	13.2%	1.059	14.9%
	29×29	1.160	6.8%	1.137	8.6%
	39×39	1.200	3.6%	1.176	5.5%
J-integral	9×9	0.818	34.3%		
	19×19	1.051	15.6%		
	29×29	1.131	9.1%		
	39×39	1.172	5.8%		

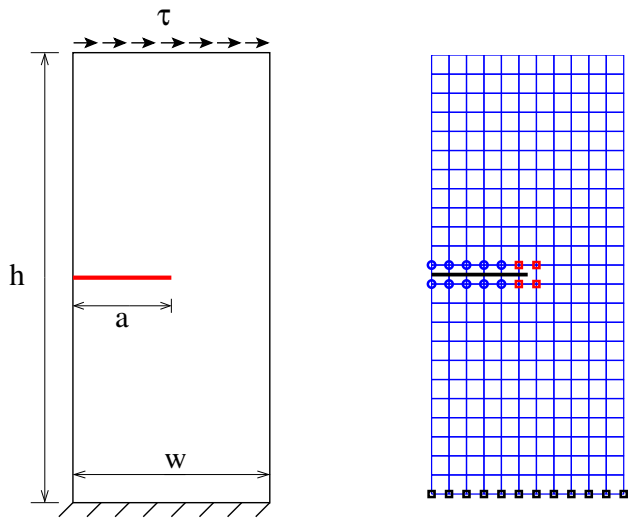

(a) (b)

Figure 5.4: Mixed mode edge crack example problem: (a) geometric definition of the problem with boundary conditions (b) enriched jump and tip nodes

enrichment space. Nonetheless, $r^{3/2}$ terms also improves the accuracy of the solution. However, when enriching with r^2 terms the results actually worsen. A similar trend has also been reported in[45; 84] when high order functions were employed.

Table 5.3: Results for K_I of mixed mode case

Order	Mesh	$K_I(\Delta c = 0)$	Relative Error	$K_I(\Delta c = h_x/2)$	Relative Error
1/2	13×23	19.863	41.6%	24.824	27.0%
	25×45	20.318	40.2%	25.815	24.1%
	37×67	20.462	39.8%	26.132	23.1%
	49×89	20.532	39.6%	26.287	22.7%
1	13×23	31.575	7.1%	31.125	8.5%
	25×45	32.229	5.2%	31.835	6.4%
	37×67	32.422	4.6%	32.048	5.7%
	49×89	32.512	4.4%	32.147	5.4%
3/2	13×23	32.529	4.3%	33.126	2.6%
	25×45	33.064	2.8%	33.645	1.0%
	37×67	33.238	2.2%	33.796	0.6%
	49×89	33.322	2.0%	33.865	0.4%
2	13×23	32.326	5.0%	33.083	2.7%
	25×45	32.928	3.2%	33.591	1.2%
	37×67	33.100	2.6%	33.732	0.8%
	49×89	33.179	2.4%	33.797	0.6%
J-integral	13×23	31.923	6.1%		
	25×45	33.097	2.7%		
	37×67	33.452	1.6%		
	49×89	33.620	1.1%		

Table 5.4: Results for K_{II} of mixed mode case

Order	Mesh	$K_{II}(\Delta c = 0)$	Relative Error	$K_{II}(\Delta c = h_x/2)$	Relative Error
1/2	13×23	3.170	30.3%	3.550	22.0%
	25×45	3.260	28.4%	3.610	20.7%
	37×67	3.293	27.6%	3.631	20.2%
	49×89	3.310	27.2%	3.642	20.0%
1	13×23	4.128	9.3%	4.128	9.3%
	25×45	4.150	8.8%	4.155	8.7%
	37×67	4.156	8.7%	4.179	8.1%
	49×89	4.159	8.6%	4.182	8.1%
3/2	13×23	4.527	0.5%	4.503	1.0%
	25×45	4.537	0.3%	4.519	0.7%
	37×67	4.540	0.2%	4.524	0.6%
	49×89	4.542	0.2%	4.526	0.5%
2	13×23	4.648	2.2%	4.509	0.9%
	25×45	4.659	2.4%	4.527	0.5%
	37×67	4.660	2.4%	4.531	0.4%
	49×89	4.660	2.4%	4.533	0.4%
J-integral	13×23	4.452	2.2%		
	25×45	4.493	1.3%		
	37×67	4.506	1.0%		
	49×89	4.513	0.8%		

Part III

An Analytical Method to Extract SERRs from Irwin's Integral-II

Chapter 6

Introduction

The approach presented in Part II is extended to study extracting SERRs in arbitrary crack settings based on Irwin's integral and high order XFEM methods. Thus inclined cracks as well as crack propagation can directly be handled by this analytical approach. Several benchmark examples are investigated including off-center cracks, inclined cracks and crack growth problems. On all these problems, the method is shown to work well, giving accurate results. Moreover, due to its analytical nature, no special postprocessing is required.

Chapter 7

Extraction of Strain Energy Release Rates using Irwin's integral and XFEM

7.1 Analytical expansion of Irwin's integral

Starting from Irwin's integral [34], the work required to extend a crack by an infinitesimal distance Δc is equal to the work required to close the crack to its original length, which is defined by Eqs. (4.1) to (4.22).

Different from previous study, the first four leading terms of r in sliding and opening displacement jumps in Eqs. (4.4) to (4.5) are retained, by plugging Williams expansion, Eqs. (3.5)–(3.6), into Eqs. (4.4)–(4.5), which yields

$$\overline{u}_r(r) = \sum_{i=1}^{\infty} u_i(r^{i/2}, \pi) - \sum_{i=1}^{\infty} u_i(r^{i/2}, -\pi) = \sum_{i=1}^{4} m_i^{II} r^{\frac{2i-1}{2}} + \mathrm{O}\big(r^{\frac{9}{2}}\big) \tag{7.1}$$

$$\overline{u}_\theta(r) = \sum_{i=1}^{\infty} v_i(r^{i/2}, \pi) - \sum_{i=1}^{\infty} v_i(r^{i/2}, -\pi) = \sum_{i=1}^{4} m_i^{I} r^{\frac{2i-1}{2}} + \mathrm{O}\big(r^{\frac{9}{2}}\big) \tag{7.2}$$

Note that the resulting sum is truncated after the order of $r^{5/2}$ appear in the formulation. Again, this is due to the choice of high order enrichment functions (see Eq. (3.14)) and considering the XFEM formulation given in Section 7.2. In section 7.2, shape functions are introduced (see Eq. (7.10)), which add additional r terms, and so it will become apparent

that all leading terms of r up to $r^{7/2}$ contribute to the derivation of the displacement jump and must remain.

Combining the stresses with strains, Eqs. (4.12)–(4.15) and plugging in Williams solutions, Eqs. (3.5)–(3.6), the definition of normal and shear stresses ahead of the crack tip is arrived at

$$\sigma_{\theta\theta}(r,0) = \frac{E}{(1+\nu)(1-2\nu)} \sum_{i=5}^{12} m_i^I r^{\frac{i-6}{2}} + \mathrm{O}\big(r^{\frac{7}{2}}\big) \tag{7.3}$$

$$\sigma_{r\theta}(r,0) = \frac{E}{2(1+\nu)} \sum_{i=5}^{12} m_i^{II} r^{\frac{i-6}{2}} + \mathrm{O}\big(r^{\frac{7}{2}}\big) \tag{7.4}$$

The sum is truncated after r^3 which again is due to the choice of high order enrichment functions (see Eq. (3.14)) and considering the XFEM formulation given in Section 7.2 and shape functions are introduced (see Eq. (7.10)).

Finally, substituting the opening displacements in Eqs. (7.1)–(7.2) and stresses in Eqs. (7.3)–(7.4) into the definition of Strain Energy Release Rate, $\mathcal{G}_I$ in Eq. (4.21) and $\mathcal{G}_{II}$ in Eq. (4.22) and integrating arrive at

$$\widetilde{\mathcal{G}}_I(\Delta c) = \frac{E}{(1+\nu)(1-2\nu)} \sum_{i=0}^{13} \alpha_i^I \Delta c^{\frac{i}{2}} + \mathrm{O}\big(\Delta c^7\big) \tag{7.5}$$

and

$$\widetilde{\mathcal{G}}_{II}(\Delta c) = \frac{E}{2(1+\nu)} \sum_{i=0}^{13} \alpha_i^{II} \Delta c^{\frac{i}{2}} + \mathrm{O}\big(\Delta c^7\big) \tag{7.6}$$

Here $\widetilde{\mathcal{G}}_I$ and $\widetilde{\mathcal{G}}_{II}$ have been defined in Eqs. (4.21) and (4.22).

The coefficients α_i^I and α_i^{II} are listed in Appendix A.6.

The goal is to find the coefficients α_i^I and α_i^{II} analytically, using the enrichment functions in XFEM.

7.2 Analytical formulation of Irwin's integral

To obtain expressions for the coefficients α_i^I and α_i^{II}, a generic rectangular element is considered with an inclined crack with crack tip at O', as shown by the red line in Figure 7.1, where O is the center of the element, (x,y) is global Cartesian coordinate system. (u,v)

defines the local Cartesian coordinate system with α being the the angle between the two Cartesian coordinate systems. u_r and u_θ are displacements in polar coordinate system (r,θ). In polar coordinate system, any point in the element domain can be defined with respect to the global system (x,y) as

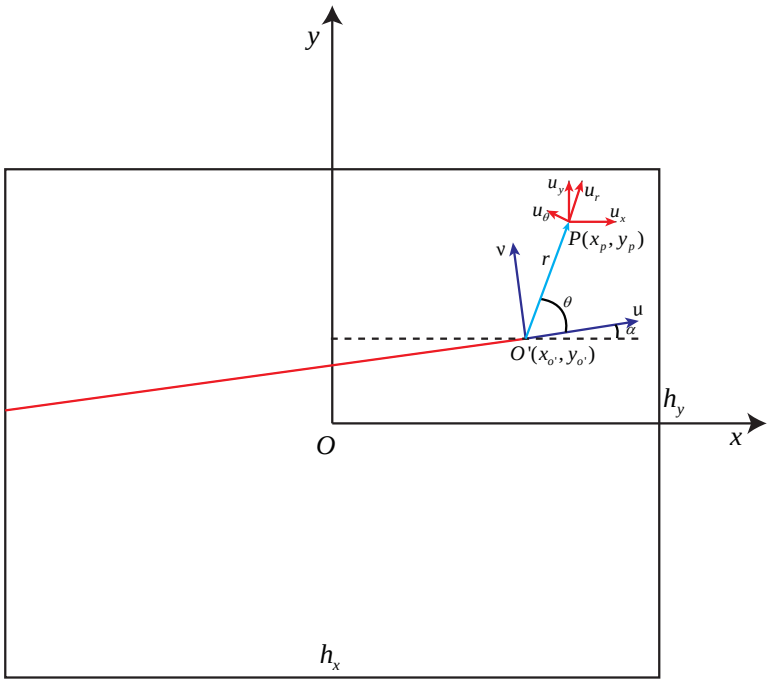

Figure 7.1: An inclined crack with tip at O'. Red solid line represents crack. P is an arbitrary point within the element under polar coordinate (r,θ).

$$x_p = r\cos(\theta+\alpha) + x_{o'} \tag{7.7}$$

$$y_p = r\sin(\theta+\alpha) + y_{o'} \tag{7.8}$$

The nodal coordinates of the element are therefore $(x_I, y_I), x_I = \pm h_x/2, y_I = \pm h_y/2, I = 1, ..., 4$, where h_x and h_y are the length of the edges in x- and y- directions, respectively.

The transformation of displacement fields from polar coordinates to cartesian coordinates can conveniently written in matrix form as

$$\begin{bmatrix} u_r \\ u_\theta \end{bmatrix} = \begin{bmatrix} \cos(\theta+\alpha) & \sin(\theta+\alpha) \\ -\sin(\theta+\alpha) & \cos(\theta+\alpha) \end{bmatrix} \begin{bmatrix} u_x \\ u_y \end{bmatrix} \tag{7.9}$$

Tip elements in XFEM consider near tip asymptotic fields, and hence the displacement field in Eq. (3.2) may be simplified and written in polar coordinates in Eq. (4.28)

In polar coordinates, the standard linear shape functions are

$$N_I = \frac{1}{4}(1 + 4\frac{x_I(r\cos(\theta+\alpha) + x_{o'})}{h_x^2})(1 + 4\frac{y_I(r\sin(\theta+\alpha) + y_{o'})}{h_y^2}) \qquad I = 1, ..., 4 \quad (7.10)$$

and the derivatives of the displacement field $\frac{\partial \boldsymbol{u}}{\partial r}$, $\frac{\partial \boldsymbol{u}}{\partial \theta}$ and shape functions $\frac{\partial N_I}{\partial r}$, $\frac{\partial N_I}{\partial \theta}$ are given in Appendix A.7.

First Eq. (7.9) is substituted into Eqs. (4.4)–(4.5) to arrive at

$$\begin{aligned}\begin{bmatrix}\overline{u}_r(r)\\ \overline{u}_\theta(r)\end{bmatrix} &= -\begin{bmatrix}\cos(\pi+\alpha) & \sin(\pi+\alpha)\\ -\sin(\pi+\alpha) & \cos(\pi+\alpha)\end{bmatrix}\begin{bmatrix}u_x(r,\pi) - u_x(r,-\pi)\\ u_y(r,\pi) - u_y(r,-\pi)\end{bmatrix}\\ &= \begin{bmatrix}\cos(\alpha) & \sin(\alpha)\\ -\sin(\alpha) & \cos(\alpha)\end{bmatrix}\begin{bmatrix}u_x(r,\pi) - u_x(r,-\pi)\\ u_y(r,\pi) - u_y(r,-\pi)\end{bmatrix}\end{aligned} \quad (7.11)$$

Assuming a general case where all enrichment functions, including high order functions in Eq. (3.14), are used to enrich the solution space (i.e. $n_F = 13$), Eq.(7.10) is substituted into Eq.(4.28) which leads to

$$\begin{aligned}u_x(r,\pi) - u_x(r,-\pi) =& \sum_{I=1}^{4} N_I(r,\pi)(u_{xI} + \sum_{j=1}^{13} F_j(r,\pi)b_{xjI})\\ &- \sum_{I=1}^{4} N_I(r,-\pi)(u_{xI} + \sum_{j=1}^{13} F_j(r,-\pi)b_{xjI}) \quad (7.12)\\ u_y(r,\pi) - u_y(r,-\pi) =& \sum_{I=1}^{4} N_I(r,\pi)(u_{yI} + \sum_{j=1}^{13} F_j(r,\pi)b_{yjI})\\ &- \sum_{I=1}^{4} N_I(r,-\pi)(u_{yI} + \sum_{j=1}^{13} F_j(r,-\pi)b_{yjI}) \quad (7.13)\end{aligned}$$

To obtain stress $\sigma_{\theta\theta}(r,0)$ and $\sigma_{r\theta}(r,0)$ the strain in Eqs. (4.12)–(4.14) is expressed by plugging Eq. (7.11) to give expression

$$\epsilon_{rr} = \frac{\partial u_x}{\partial r}\cos\alpha + \frac{\partial u_y}{\partial r}\sin\alpha \quad (7.14)$$

$$\epsilon_{\theta\theta} = \frac{1}{r}(u_x\cos\alpha + u_y\sin\alpha - \frac{\partial u_x}{\partial \theta}\sin\alpha + \frac{\partial u_y}{\partial \theta}\cos\alpha) \quad (7.15)$$

$$\epsilon_{r\theta} = \frac{1}{2}(\frac{1}{r}\frac{\partial u_x}{\partial \theta}\cos\alpha + \frac{1}{r}\frac{\partial u_y}{\partial \theta}\sin\alpha - \frac{\partial u_x}{\partial r}\sin\alpha + \frac{\partial u_y}{\partial r}\cos\alpha + \frac{u_x}{r}\sin\alpha - \frac{u_y}{r}\cos\alpha) \quad (7.16)$$

Then stress $\sigma_{\theta\theta}(r,0)$ and $\sigma_{r\theta}(r,0)$ are obtained by plugging Eqs. (7.14)–(7.16) into Eqs. (4.15)–(4.16) which gives the expressions

$$\begin{aligned}\sigma_{\theta\theta}(r,0) = &\frac{E\nu}{(1+\nu)(1-2\nu)}\Big(\frac{\partial u_x}{\partial r}\Big|_{\theta=0}\cos\alpha + \frac{\partial u_y}{\partial r}\Big|_{\theta=0}\sin\alpha\Big)\\ &+\frac{E(1-\nu)}{(1+\nu)(1-2\nu)}\Big(-\frac{1}{r}\frac{\partial u_x}{\partial\theta}\Big|_{\theta=0}\sin\alpha + \frac{1}{r}\frac{\partial u_y}{\partial\theta}\Big|_{\theta=0}\cos\alpha\Big)\end{aligned} \tag{7.17}$$

$$\sigma_{r\theta}(r,0) = \frac{E}{2(1+\nu)}\Big(\frac{1}{r}\frac{\partial u_x}{\partial\theta}\Big|_{\theta=0}\cos\alpha + \frac{1}{r}\frac{\partial u_y}{\partial\theta}\Big|_{\theta=0}\sin\alpha - \frac{\partial u_x}{\partial r}\Big|_{\theta=0}\sin\alpha + \frac{\partial u_y}{\partial r}\Big|_{\theta=0}\cos\alpha\Big) \tag{7.18}$$

The next step is to expand Eqs. (7.11) and Eqs. (7.17)–(7.18) by substituting Eq. (4.28), Eq. (7.10) and Eqs. (A.44)–(A.47) at appropriate angle. Then the final step is to match all coefficients of leading order terms for opening displacement jumps in Eq. (7.11) with (7.1) and (7.2). Similarly, the coefficients for stresses in Eqs. (7.17)–(7.18) are matched with those in (7.3)–(7.4). Finally, the general solution for Strain Energy Release Rates with finite integration limits is obtained in closed form. These constants are listed in Appendix A.6. Finally, the general solution for Strain Energy Release Rates with finite integration limits is obtained in closed form.

Remark: *It is important to note that in the case of a horizontal crack with $\alpha = 0$ and crack tip positioned at $(x_{o'}, y_{o'}) = (0,0)$ all the formulations and coefficients presented in this chapter reduce back to the derivations given in Chapter 4. Thus the current work is a generalization of the method proposed in Part II.*

7.3 Numerical formulation of Irwin's integral

The SERRs are computed using the Irwin's integral. The integration step of Δc can be chosen from 0 to admissible distance within an element, which is defined as the crack tip to the closest boundary before or behind the crack tip. The admissible distance is illustrated in Fig. 7.2.

All results related to the derivation in this section have been verified by numerical integration (1D Gauss Quadrature rule) of Irwin's integral, as shown in Fig. 5.1.

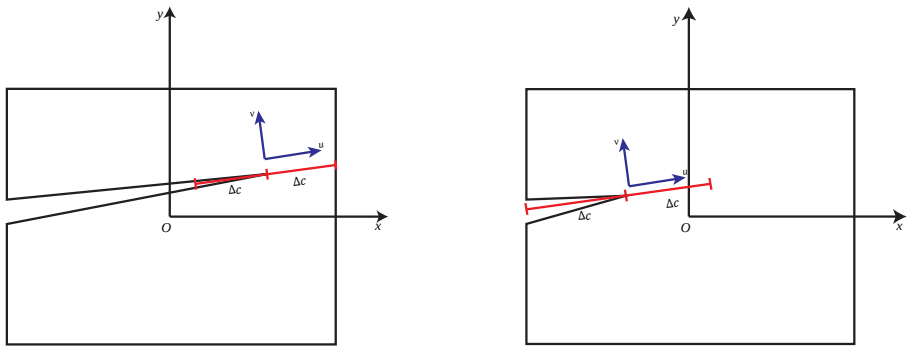

(a) (b)

Figure 7.2: Admissible integration step Δc: (a) Δc is defined as the distance to the boundary before the crack tip (b) Δc is defined as the distance to the boundary after the crack tip

In practical XFEM realization, the stress and strain are computed in Cartesian coordinate system so both quantities need to be transformed into polar coordinate system shown in Eqs. (5.1) and (5.2). The transformation relation for displacement is given in Eq. (7.11) and for stress is given below

$$\begin{bmatrix} \sigma_{rr}(r,0) \\ \sigma_{\theta\theta}(r,0) \\ \sigma_{r\theta}(r,0) \end{bmatrix} = \begin{bmatrix} \cos^2(\alpha) & \sin^2(\alpha) & 2\cos(\alpha)\sin(\alpha) \\ \sin^2(\alpha) & \cos^2(\alpha) & -2\sin(\alpha)\cos(\alpha) \\ -\sin(\alpha)\cos(\alpha) & \sin(\alpha)\cos(\alpha) & \cos^2(\alpha)-\sin^2(\alpha) \end{bmatrix} \begin{bmatrix} \sigma_{xx}(r,0) \\ \sigma_{yy}(r,0) \\ \sigma_{xy}(r,0) \end{bmatrix} \tag{7.19}$$

The algorithm using numerical implementation is straightforward although time consuming due to nonlinearity stress and opening fields near the crack tip, which is illustrated below.

Algorithm: **Numerical Implementation of Irwin Integral**

Preprocessor

i. Initialize the system by incorporating high order enrichment functions $\mathbf{F}$. (Eqs. (3.10) to (3.14))

Solution

i. Solve linear system $\mathbf{Kd} = \mathbf{f}$ to find node displacement $\mathbf{d}$.

Postprocessor

i. Extract node displacement $\mathbf{d_e}$ at tip element.

ii. Compute displacement $\mathbf{u_x}$, $\mathbf{u_y}$ stress $\sigma_{\mathbf{xx}}$, $\sigma_{\mathbf{yy}}$, $\sigma_{\mathbf{xy}}$ at Gauss point with $\mathbf{d_e}$.

iii. Transform displacement $\mathbf{u_x}$, $\mathbf{u_y}$ into crack opening using Eq. (7.11).

iv. Transform stress $\sigma_{\mathbf{xx}}$, $\sigma_{\mathbf{yy}}$, $\sigma_{\mathbf{xy}}$ using Eq. (7.19).

v. Compute numerical approximation of Irwin integral using Eq. (5.2).

Chapter 8

Numerical examples

The proposed approach is studied on an off-center crack tip problem, an angle-cracked plate under tension problem and a crack growth problem. All numerical examples shown in this section are plane strain problems. To alleviate computational issues related to tip element integration, we used used the trapezoidal integration rule with 200×200 equally spaced quadrature points for computation of element stiffness matrix. Future research will develop more efficient integration techniques. In all subsequent examples the crack extension in the Irwin's integral is taken as the admissible distance.

8.1 Off-center crack tip problem

In order to show the robustness of proposed approach the first examples are pure modes I and II cases with crack tip being off the center of tip element. The problem consists of a square plate with dimensions 10×10 units. Displacement boundary conditions with normalized stress intensity factors $K_I = 1$ and $K_{II} = 1$ are applied to generate modes I and II cracks openings. These essential boundary conditions (assuming a plane strain state) are given by

$$\text{Mode I}: \begin{cases} u_x = \frac{2(1+\nu)}{E} K_I \sqrt{\frac{r}{2\pi}} \cos(\frac{\theta}{2})[2 - 2\nu - \cos^2(\frac{\theta}{2})] \\ u_y = \frac{2(1+\nu)}{E} K_I \sqrt{\frac{r}{2\pi}} \sin(\frac{\theta}{2})[2 - 2\nu - \cos^2(\frac{\theta}{2})] \end{cases} \tag{8.1}$$

$$\text{Mode II}: \begin{cases} u_x = \frac{2(1+\nu)}{E} K_{II} \sqrt{\frac{r}{2\pi}} \sin(\frac{\theta}{2})[2 - 2\nu + \cos^2(\frac{\theta}{2})] \\ u_y = -\frac{2(1+\nu)}{E} K_{II} \sqrt{\frac{r}{2\pi}} \cos(\frac{\theta}{2})[1 - 2\nu - \sin^2(\frac{\theta}{2})] \end{cases} \tag{8.2}$$

where r is the distance from the boundary to the crack tip and θ is the angle between the positive x axis and boundary node. The boundary conditions are applied to all four sides of the rectangular domain. The Young's modulus and Poisson ratio are chosen as $E = 1 \times 10^7$ and $\nu = 0.3$ respectively and the mesh is chosen as 19×19.

The crack tip is located from $-2h_x/5$ to $2h_x/5$ at an incremental $h_x/10$ within the tip element, which is illustrated in Fig. 8.1.

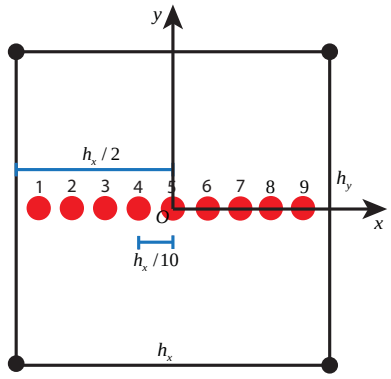

Figure 8.1: Crack tip off the center of the tip element

The computed results are summarized in Table 8.1.

Table 8.1: Results for K_I and K_{II} of off-center pure mode problem

Order	Tip location	K_I	Relative Error	K_{II}	Relative Error
1/2	1	0.763	23.71%	0.723	27.69%
	2	0.780	21.97%	0.751	24.87%
	3	0.787	21.34%	0.778	22.16%
	4	0.789	21.12%	0.801	19.88%
	5	0.791	20.89%	0.820	18.03%
	6	0.763	23.65%	0.820	18.04%
	7	0.734	26.55%	0.818	18.24%

	8	0.701	29.92%	0.813	18.67%
	9	0.656	34.43%	0.805	19.52%
1	1	0.864	13.58%	0.823	17.69%
	2	0.856	14.40%	0.848	15.24%
	3	0.893	10.73%	0.885	11.54%
	4	0.936	6.44%	0.915	8.53%
	5	0.966	3.49%	0.935	6.54%
	6	0.990	1.03%	0.950	5.06%
	7	1.009	0.93%	0.960	4.00%
	8	1.023	2.30%	0.967	3.28%
	9	1.030	3.01%	0.973	2.65%
3/2	1	0.910	8.97%	0.931	6.89%
	2	0.965	3.46%	0.972	2.75%
	3	1.000	0.03%	0.996	0.37%
	4	1.007	0.72%	1.003	0.33%
	5	1.007	0.65%	1.004	0.42%
	6	1.010	1.03%	1.007	0.72%
	7	1.013	1.26%	1.011	1.08%
	8	1.014	1.39%	1.015	1.50%
	9	1.011	1.06%	1.022	2.16%
2	1	0.994	0.61%	0.960	4.08%
	2	0.998	0.19%	0.995	0.47%
	3	1.007	0.72%	1.005	0.53%
	4	1.010	0.97%	1.008	0.77%
	5	1.007	0.71%	1.006	0.64%
	6	1.007	0.71%	1.009	0.90%
	7	1.006	0.56%	1.012	1.19%

8	1.004	0.36%	1.014	1.37%
9	1.000	0.03%	1.014	1.41%

It can be seen from the Table 8.1. that the proposed approach yields convergent results with higher order enrichment at the tip element. The integration step Δc varies at different tip location while the computation presents relatively stable results.

8.2 Angle-cracked plate under tension problem

The second benchmark example is a plate under uniaxial opposite stress tension with an inclined crack placed in the center (Fig. 8.2). The square plate has side length $W = 10$ units with crack length $a = 0.5$ units. Uniaxial loading is applied onto the top and bottom sides. In the example, the mesh is chosen as 99×99. Poisson's ratio ν is chosen as 0.3 and Young's modulus E as 100 respectively. The exact SIFs are given by

$$K_I = \sigma\sqrt{\pi a}\cos^2(\alpha) \tag{8.3}$$

$$K_{II} = \sigma\sqrt{\pi a}\sin(\alpha)\cos(\alpha) \tag{8.4}$$

where α is the crack angle to the horizontal. The numerical results, in comparison with exact solutions, are illustrated in Fig. 8.3, where the dashed line and solid line represent exact solution K_I and K_{II}. It can be seen that order=3/2 provides satisfactory results while order=2 presents more stability.

8.3 Double cantilever beam

Next consider a crack growth example [4] in a double cantilever beam specimen. The geometry is chosen as 11.8×3.94units shown in Fig. 8.4. The initial horizontal crack length $a = 3.94$ units and opposite loads $P = 197$ are applied on the left side. Poisson's ratio ν is chosen as 0.3 and Young's modulus $E = 3 \times 10^7$ respectively. The mesh is chosen as 80×32. A small perturbation with length $\Delta x = 0.3$ units is initiated at the crack tip at angle θ. To observe the different crack propagation path corresponding to different perturbations, θ is

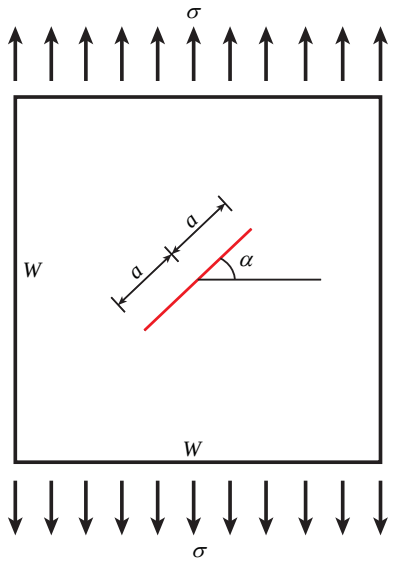

Figure 8.2: Angle-cracked plate under uniaxial loading in opposite direction

set equal to 0, 5, 10 and 15. We used the maximum hoop stress [49] criteria to compute the direction θ_c in which the crack will propagate. The angle θ_c is computed as

$$\theta_c = 2\arctan\frac{1}{4}\left(\frac{K_I}{K_{II}} \pm \sqrt{\left(\frac{K_I}{K_{II}}\right)^2 + 8}\right), -\pi < \theta_c < \pi \tag{8.5}$$

where SIFs K_I and K_{II} are computed using proposed approach. An illustration of the crack extension implementation scheme used in this study is two steps shown in Fig. 8.5. The crack is propagated in the following two steps:

Step i: *The direction of crack propagation is determined from the proposed method by computing K_I and K_{II}, and the crack is virtually extended by a length of $\Delta a = \sqrt{h_x^2 + h_y^2}$. We choose this extension length to make sure that the crack propagates to the next element. In Fig. 8.5(a) the black line indicate the crack extension at propagation at step I, and the red dashed line represent the virtual crack extension.*

Step i+1: *The kink inside the element is removed by assuming a straight line segment in the element. This is represented by the green line in Fig. 8.5(b), which simply connects the two crossing points in the element. Thus we obtain the new crack segment at the tip element (shown in solid red line in Fig. 8.5(b) in step i+1).*

Fig. 8.6 illustrates the crack growth path initiated by perturbation $\theta = 15$ and Fig. 8.7

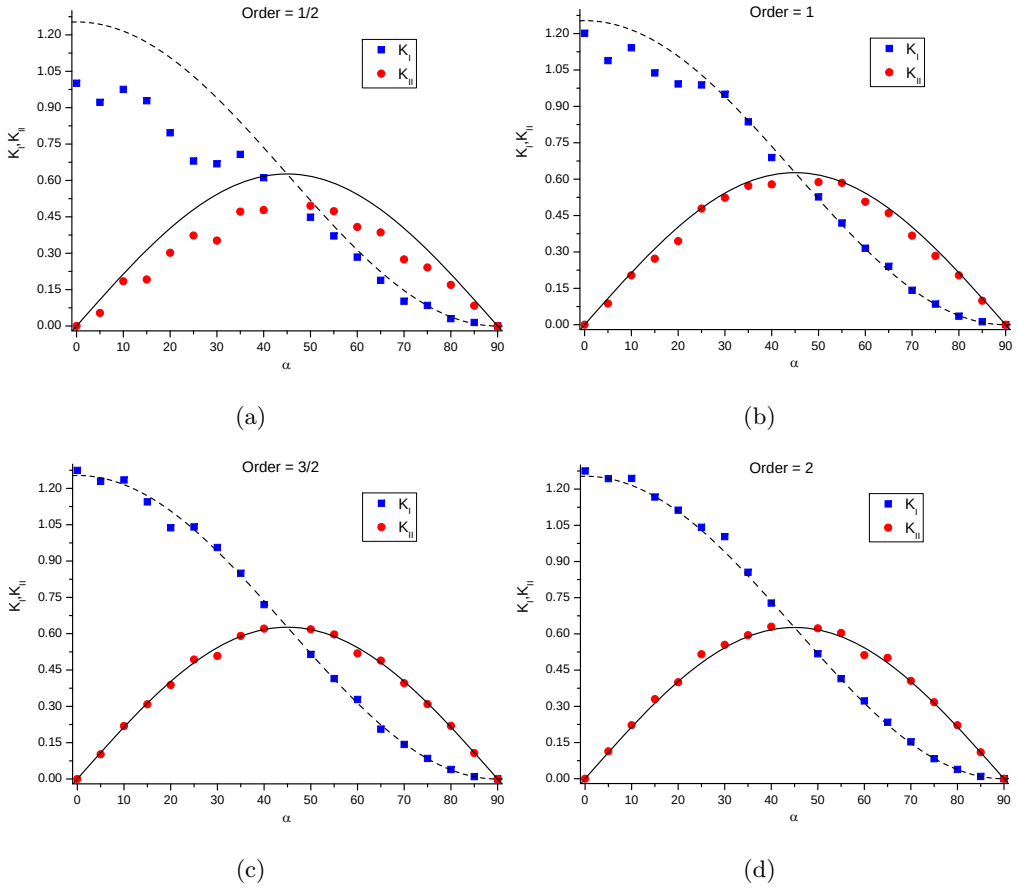

Figure 8.3: K_I and K_{II} in a plate with an angled center crack. Dashed line and solid line represent exact SIFs K_I and K_{II}

shows a comparison of crack path with different initial perturbations.

8.4 L-shaped plate

Finally consider a multiple crack growth example [84; 75] in a L-shaped plate. The problem is more realistic for engineering application. The geometry is shown in Fig. 8.8. The bottom edge of the plate is fixed in both directions and the top left edge is imposed a vertical displacement $u = 1.55mm$. The material modeled is a high strength steel 18Ni1900 with Young's modulus $E = 190GPa$, Poisson's ratio $\nu = 0.3$ and fracture toughness $K_c = 68MPa\sqrt{m}$ [59]. The initial lengths of the three cracks, from top to bottom, are $l_1 =$

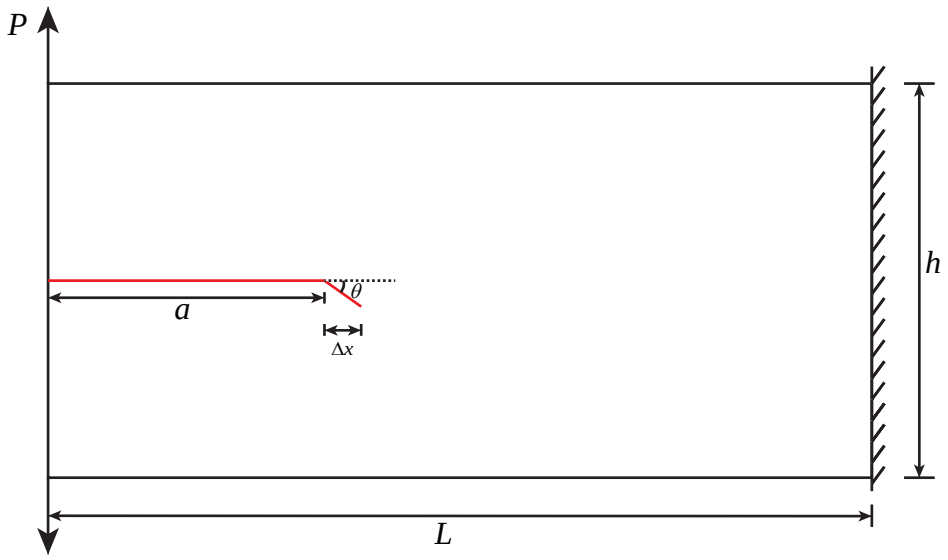

Figure 8.4: Double cantilever beam specimen under opposite load

$11.67mm$, $l_2 = 6.80mm$ and $l_3 = 5.30mm$ with distance $h_1 = 21.5mm$ and $h_2 = 14.0mm$. The angle α for the first crack is equal to 30. The mesh is 40×40 units for domain $h \times h$. The interesting crack shielding phenomena can be observed through crack propagation process shown in Fig. 8.9.

The equivalent mode I stress intensity factor K_I^{eq} is computed at each step to determine crack propagation [19] show in Fig. 8.10. If the computed value is below the given material fracture toughness K_c, represented by solid red line, the crack will stop growing.

As indicated by simulation, the lower and middle cracks stop propagating at step 7 and 14 respectively where the two cracks are shielded by the propagating crack.

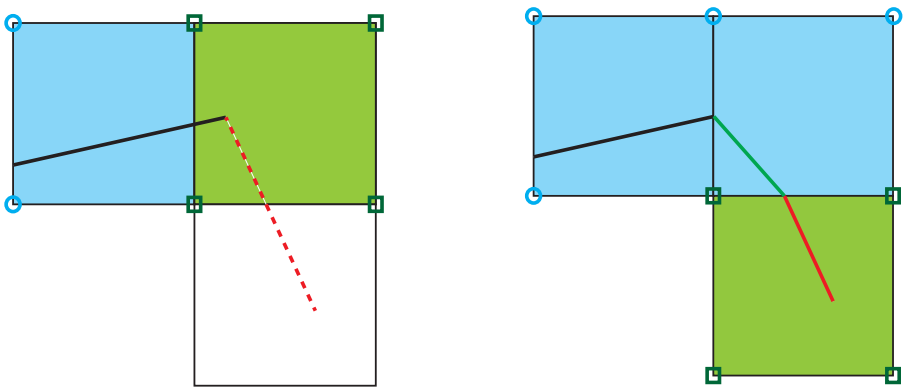

(a) (b)

Figure 8.5: Crack extension illustration: Green colored element indicate a tip element and blue indicate an element fully cut by the crack (a) Step i: Red dashed line shows the tentative direction and extension of crack propagation at step $i+1$ determined using the proposed method (b) Step $i+1$: The kink in tip element at step i is removed by assuming a straight line segment in the element (shown in green) and the actual crack path at propagation step $i+1$ is shown by the red line.

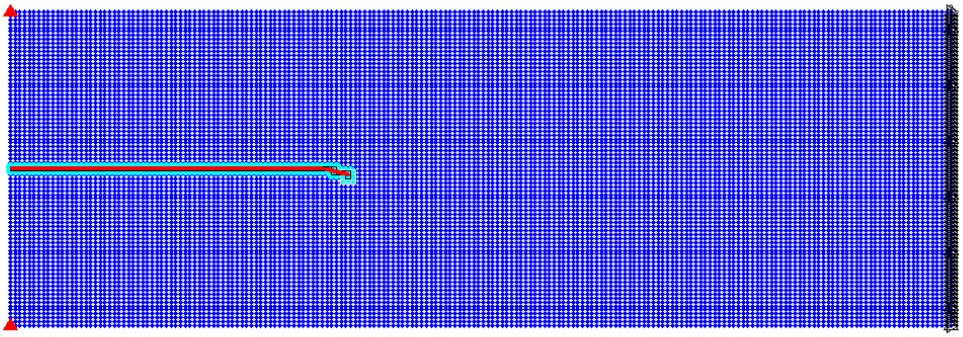

(a)

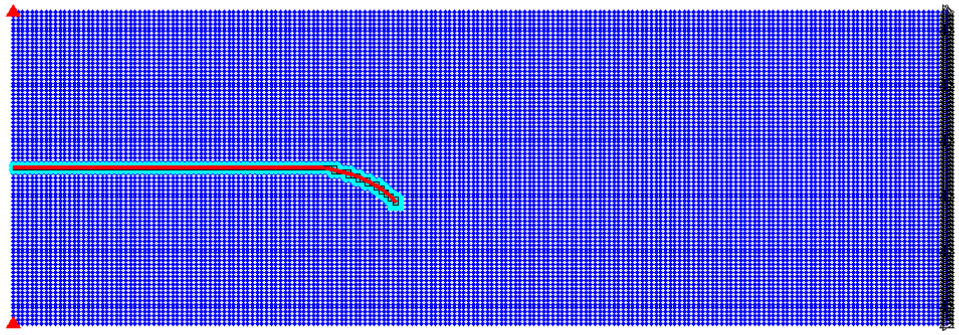

(b)

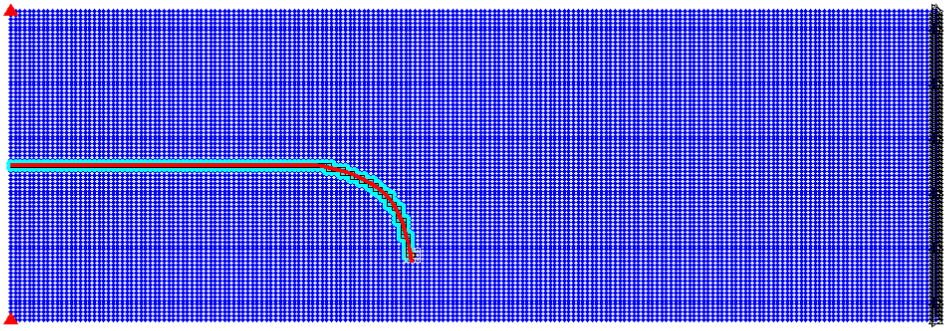

(c)

Figure 8.6: Crack propagation illustration by setting initial perturbation $\theta = 15$

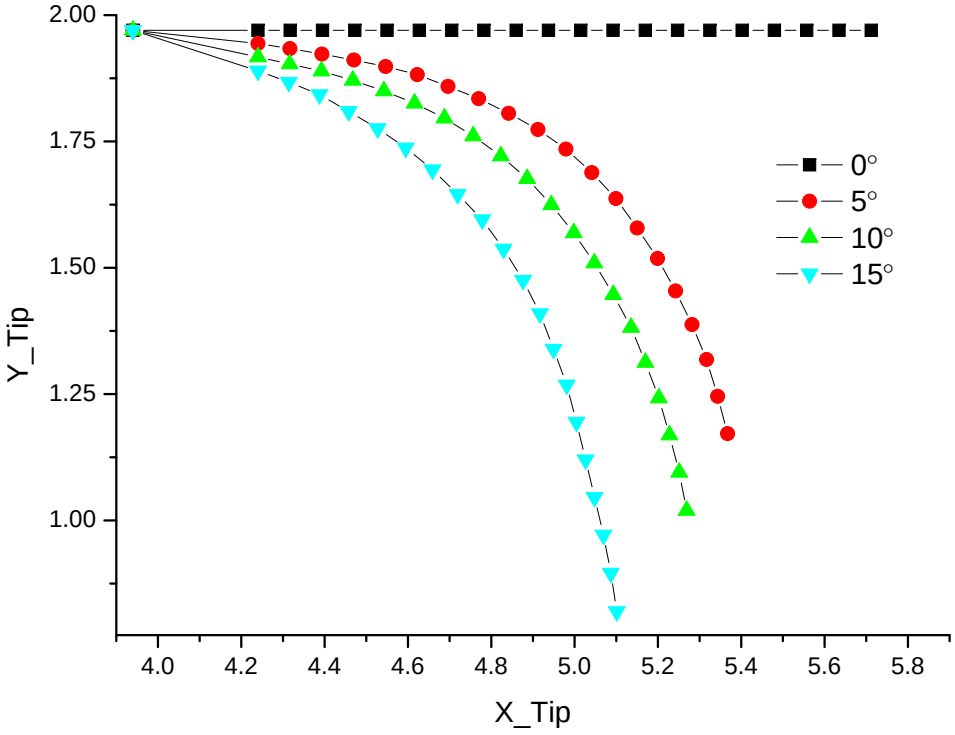

Figure 8.7: Comparison of crack path initiated by different perturbation

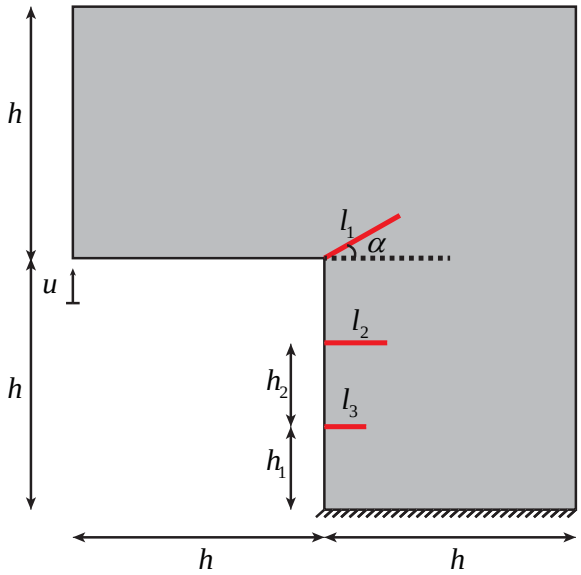

Figure 8.8: Geometry and initial setup of the L-shaped plate example

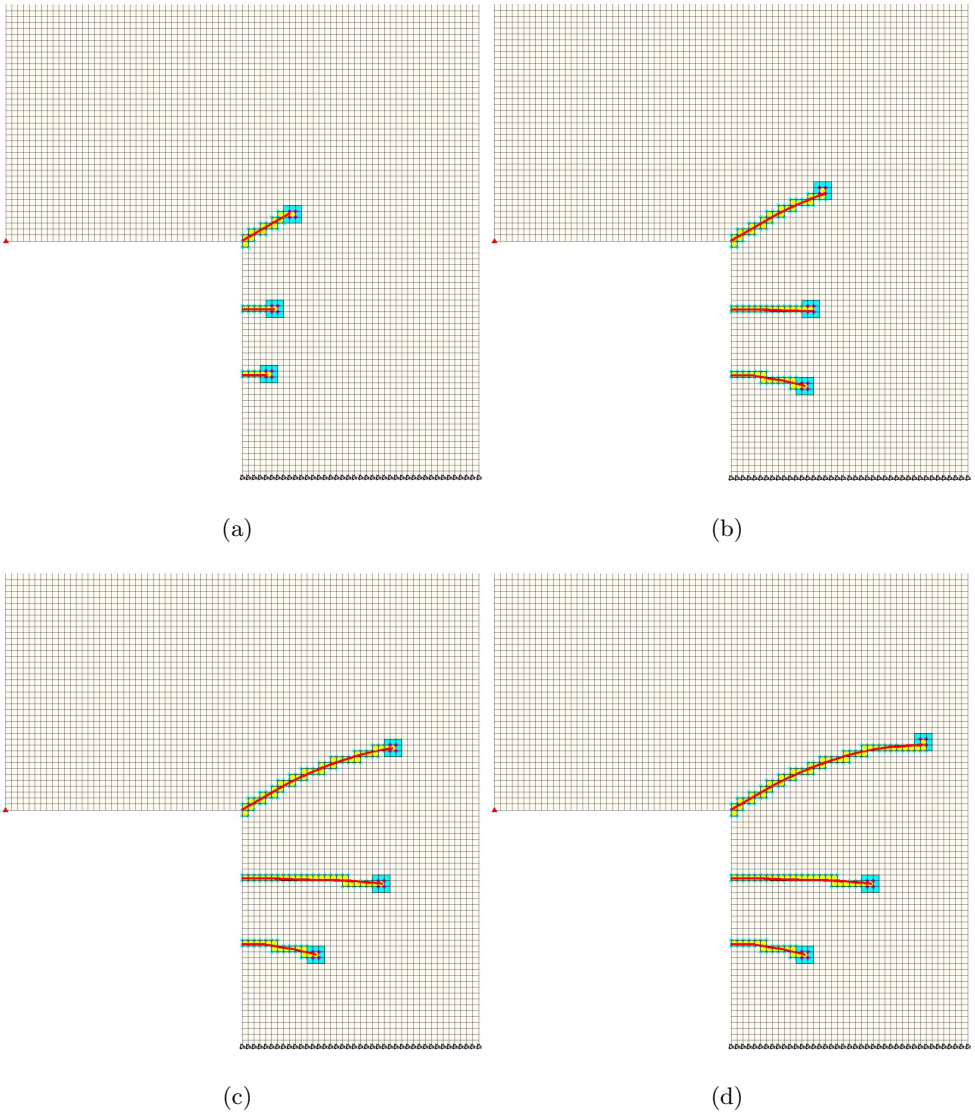

(a) (b)

(c) (d)

Figure 8.9: Crack propagation illustration for steps 1, 7, 14 and 19

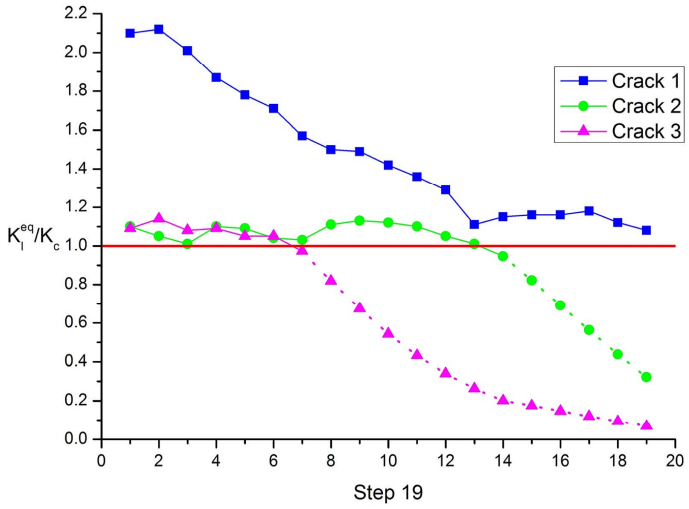

Figure 8.10: Computed equivalent mode I SIF K_I^{eq}. Solid red line represents the material fracture toughness below which the crack growing stops.

Part IV

The Mechanics of SWCNT Aggregates

Chapter 9

Introduction

Carbon nanotubes (CNTs) were first discovered in 1991 [33] and have since been the subject of intensive research due to a wide range of potential applications [17; 48; 15; 14; 28; 35; 13]. CNTs are allotropes of carbon with a nanostructure that can have a length-to-diameter ratio greater than $1,000,000$ and, in terms of tensile strength and elastic modulus, are among the strongest and stiffest materials ever synthesized. A single-walled carbon nanotube (SWCNT) can be regarded as a roll of graphene sheet while a multi-walled carbon nanotube (MWCNT) is an assembly of coaxial SWCNTs where the neighboring layers are separated by a Van der Waals equilibrium distance $0.34\ nm$ [63; 61]. The high values of CNTs Young modulus and tensile strength have attracted the attention of many researchers, since their discovery.

One interesting application of nanotubes is their use as reinforcing components in nanocomposites, e.g. in epoxy adhesives or polymers, which could be employed for infrastructure or military protection. However, to obtain nearly optimal performance from a continuum point of view, it is well know that CNTs must be homogenously dispersed in the polymer [27; 29]. This distribution would lead to a macroscopically isotropic response of nanocomposites, i.e. the mechanical behavior will be similar in every loading direction.

In this part a novel molecular mechanics approach is proposed to study the mechanics of CNT aggregates. Despite the large bulk of work studying the mechanical properties of a SWCNT, MWCNT and nanotube composites, little attention has been given to CNT aggregates composed of randomly agglomerated SWCNT or MWCNT bundles [61]. Chen et al.

[12] examined the aggregation behavior of colloidal single-walled carbon nanotubes(SWNT) in dilute aqueous suspensions using a novel light scattering measurement technique. Kirca et al. [37] proposed a 2-D and 3-D CNT network generation methods by which the geometrical parameters, such as CNT length, chirality, intersection angle and junctional density, can be adjusted to obtain a random CNT network. Coluci et al. [16] conducted a theoretical investigation of the mechanical properties of idealized networks formed by single-walled carbon nanotubes.

This deficit can partially be attributed to the intensive computational requirements for modeling such structures with molecular dynamics (MD) methods. Hence in most molecular modeling methods of CNTs, only a small number is modeled assuming periodic boundary conditions, nonetheless important conclusions can still be made. For example a study performed by Yakobson et al. [80] on compression of a single CNT reported that a Young Modulus of 5.5 Tpa. Buehler et al. [10] have investigated a very long SWCNT under compressive loading and found three different deformation mechanisms with increasing aspect ratios. Using MD, Frankland et al. [25] investigated the stress-strain behavior of polymers enhanced by unidirectional nanotubes and found that a long continuous nanotube composite is enhanced only in the direction of the nanotube. Qi et al. [57] modeled polymer with nanotubes using a Nose-Hoover MD method which adjusts the system volume based on temperature and pressure. The stress-strain curves, along with Young's modulus and Poisson's ratio were obtained at different temperatures, and it was shown that the Young modulus of the system will decrease as the temperature increases.

To overcome the computational limitations of molecular dynamics, a novel molecular mechanics approach is proposed to investigate the stress-strain response of randomly dispersed short SWCNTs. In other words the mechanics of SWCNT aggregates consisting of many nanotubes randomly dispersed is studied in the simulation cell. The idea is to perform strain loading by incrementally stretching the simulation cell and conformingly mapping atoms to their new position. Then, at every increment a constrained minimization is performed where the CNT ends are restrained from moving. Atomic interactions within and between CNTs are modeled by an AIREBO potential and the CNTs dispersion is determined by an algorithm that produces spherical uniform distribution of CNTs. In

our simulations, a (5,5) armchair SWCNT with length 2 nm is employed to construct the SWCNT aggregates.

The method is implemented within LAMMPS, a molecular dynamics software developed at Sandia National Labs [56]. Using this method the mechanics of nanotube aggregates is studied to demonstrate that the isotropic response is indeed obtained as the number of randomly dispersed CNTs increases (an intuitive result that would require intensive computational resources with molecular dynamics). Moreover, it is shown that Young's modulus increases as the density of nanotubes in the unit cell increases.

The part is organized in the following way: The atomistic potential(AIREBO) that accounts for both short and long atom interactions is introduced first. Then a detailed algorithm for generating randomly dispersed CNTs in a computational cell is described. Next, the proposed incremental constrained minimization method is given. The stress-strain response curves and the corresponding discussion are presented in the end.

Chapter 10

Computational model

10.1 Bonding potentials

Two bond types, known as σ and π-bonds, describe the interaction between atoms of carbon nanotubes. σ-bond is due to the process of sp^2 hybridization [9]. This is a covalent bond which provides most of CNT's fabulous strength and has been studied experimentally and theoretically in [72; 38; 46; 82]. π-bond, exists between layers of multi walled CNTs, and between different single walled CNTs in aggregates [61]. Its effectiveness is relatively weak but not negligible. Hence, in order to reproduce these experimental results, many empirical potentials were developed. However, these potential primarily capture σ-bonds, neglecting the effects of π-bonds. One such potential, is the so-called Tersoff-Brenner potential [7]. This is a multi-body potential, suitable for modeling covalent bonds between carbon, silicon, hydrogen, germanium and their compound. Unfortunately, despite the fact that numerous studies have been devoted to investigating the mechanical properties of SWCNT, in most of these studies, only the σ-bond was considered, although some research considering both bonds can also be found in the literature [44].

In this study Brenner's second generation Reactive Empirical Bond-Order (REBO) potential [8] is employed to describe interactions within carbon nanotubes. Its accuracy was verified by computing the fracture stress and strain of a single (12,12) SWCNT [43] and comparing it to other published studies [5]. In order to incorporate Van der Waals interactions between SWCNTs, a complete bond expression must consist of at least two terms as

[69]

$$E = \frac{1}{2}\sum_{i}\sum_{j\neq i}[E_{ij}^{REBO} + E_{ij}^{LJ}] \tag{10.1}$$

where the index i runs through all the atoms in the system, and where

$$E_{ij}^{LJ} = S(t_r(r_{ij}))S(t_b(b_{ij}^{*}))C_{ij}V_{ij}^{LJ}(r_{ij}) + [1 - S(t_r(r_{ij}))]C_{ij}V_{ij}^{LJ}(r_{ij}) \tag{10.2}$$

contributes to the Lennard-Jones (LJ) potential energy. Here r_{ij} is the distance between atom i and j and the $t_r(r_{ij})$ is a scaling function used to rescale the domain of the switching function $S(t)$. V_{ij} is a standard 12-6 LJ interactions and C_{ij} is a connectivity switch to disable LJ interactions within REBO range. In general, a LJ potential is valid where REBO potential is ineffective, i.e. when $r > 0.2\ nm$, which is controlled by switching on the function $S(t)$ so that the short-ranged LJ repulsive term $\frac{1}{r^{12}}$ does not interfere with energy described by E^{REBO}.

10.2 Generation of randomly dispersed CNTs in the cell

Current atomistic modeling research is mainly focused on individual SWCNT [36], MWCNT [54] or polymer-nanotube composites [25]. While these theoretical models show impressive mechanical behavior, in practice, CNTs are not individually synthesized but rather randomly agglomerated bundles [71]. Moreover, as pointed out [61], the high stiffness and strength obtained from an individual SWCNT is not necessarily present in CNTs structures.

One precondition when simulating CNT structures, valid for most simulations, is to construct a representative cell that can present both a homogeneous distribution as well as isotropic behavior in all loading directions. The cell must exhibit isotropic properties so that the simulation results are not affected by the initial configuration.

To generate a representative cell for CNT aggregates, it is necessary to rotate and displace every SWCNT based on an unbiased distribution, as illustrated in Figure 10.1. One natural assumption is that the direction of a SWCNT in space follows a spherical uniform distribution. One approach to generate this distribution is by employing the trig method [67]. The trig method, which is very efficient in three dimensions, finds an unbiased

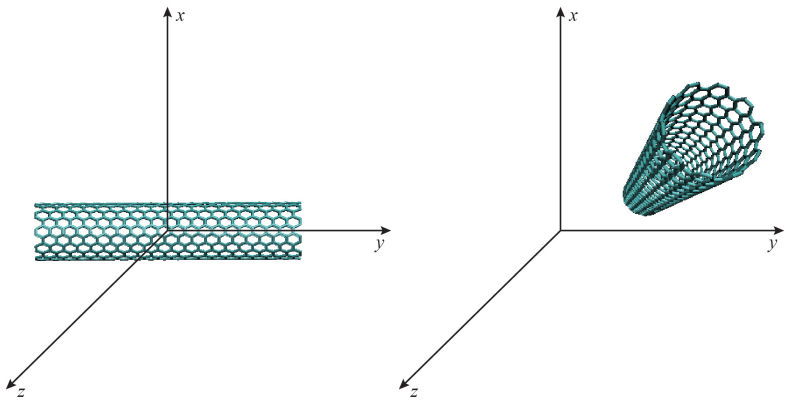

(a) (b)

Figure 10.1: (a) Orientation of a SWCNT in axial direction. (b) Rotation and translation of a SWCNT in an arbitrary direction

angle θ in space starting from a given base direction, e.g. the y-axis. Then a rotation matrix $\mathbf{R}$ is established as

$$\mathbf{R} = \mathbf{I} + \sin\theta\mathbf{M} + (1 - \cos\theta)\mathbf{M^2} \tag{10.3}$$

to translate every atom in a standard carbon nanotube to a new position that corresponds to a spherical uniform distribution. Matrix $\mathbf{M}$ is constructed using angles obtained from the trig method and $\mathbf{I}$ is the identity matrix. Once formed, the SWCNT is displaced at a distance based on a 3-dimensional uniform distribution, defined in a range of a cell. With each new added SWCNT, the distance between its axis and all other already displaced CNTs' axis must be computed to ensure that it is greater than $2r + 0.2$ nm where r is the radius of CNT and 0.2 is the distance within which covalent bonds will form. By doing so, unwanted covalent bonds can be avoided in CNT structures. If this requirement has not been met, a new location is generated for further verification. It is emphasized that individual SWCNT are not relaxed before being introduced into the cell. In other words, first all CNTs are placed in the aggregates and then a global energy minimization is performed as discussed in Section 2.3, where each CNT finds its optimal position.

Employing the algorithm described above leads to a typical initial configuration with randomly dispersed CNTs in a box, as illustrated in Figure 10.2 for 10 and 200 CNTs. While in this study a (5,5) armchair SWCNT with a 2 nm length is employed to construct

the SWCNT aggregates, this method is not restricted to any particular SWCNT type.

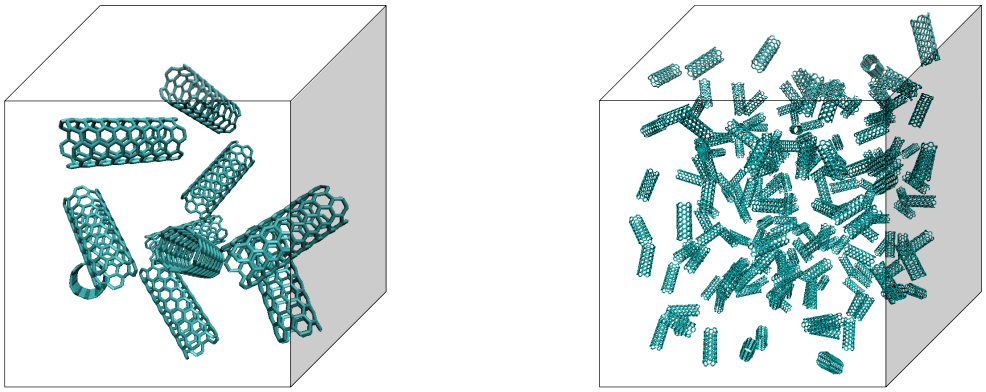

(a) (b)

Figure 10.2: (a) A representative computational cell with 10 (5,5) SWCNTs. (b) A representative computational cell with 200 (5,5) SWCNTs

10.3 Simulation scheme

Molecular statics and molecular dynamics are two widely used methods in atomistic simulations and modeling. Generally speaking, molecular dynamics (MD) employs Newton's law and integrate the equations in time to solve for atom movements in space. This method usually contains two phases: equilibration and production, therefore committing significant computing resources. Moreover, the time steps used to integrate these equations are often on the order of femto-seconds (10^{-15} sec). Furthermore, to observe meaningful results in MD, one typically needs to employ thousands of steps. Hence, for some problems MD may become prohibitively expensive.

Molecular statics on the other hand, investigates ensemble properties by energy minimization. Physical properties are immediately obtained once equilibrium is achieved. Nonetheless, one significant drawback is that molecular statics does not consider temperature effects, hence any properties obtained from the simulation corresponds to a 0 degrees kelvin temperature.

In this study, molecular statics is employed to study the mechanics of CNT aggregates. The method developed in the study illustrates that an isotropic response of the cell can

only be obtained when considering many randomly dispersed CNTs.

In order to obtain the stress-strain response, an incremental loading approach with a constrained minimization is proposed to solve problem at every step. Assuming that the iteration begins with a random distribution of N nanotube aggregates, the following algorithm is proposed:

(1) solve an unconstrained energy minimization problem to let atoms locate their optimum positions.

(2) expand the cell in one direction at a time (x, y or z which is chosen randomly) while keeping the other two directions free. The incremental expansion size is a parameter defined by the user.

(3) rescale conformingly the coordinates of CNT atoms with the new cell dimensions. This step essentially stretches the nanotube with the computational cell.

(4) solve a constrained energy minimization problem by fixing the ends of every CNT in the cell. Upon convergence obtain the stress in the system, e.g. by using a virial stress measurement.

(5) repeat steps (2)-(4) until a specified strain is achieved and obtain the stress increment corresponding to the strain increment.

(6) repeat the incremental loading steps (2)-(5) in all three directions and obtain the total stress-strain response of the system.

One incremental loading step with a single CNT is illustrated in Figure 10.3. Dashed lines correspond to increment i, and solid lines to increment i+1. The bold lines illustrate the two fixed ends of the nanotube, retaining the nanotube from retreating back to its original positions.

Remark 1: *It is assumed that only nanotubes are present, and hence all nanotubes are stretched.*

Remark 2: *Note that the cell expands incrementally in one direction at a time. The other two directions are free to contract so that a zero stress is obtained due to the energy minimization algorithm, however, it is observed that the total volume of the cell is not conserved.*

Remark 3: *The virial stress measure is employed to compute the stress from atomistic*

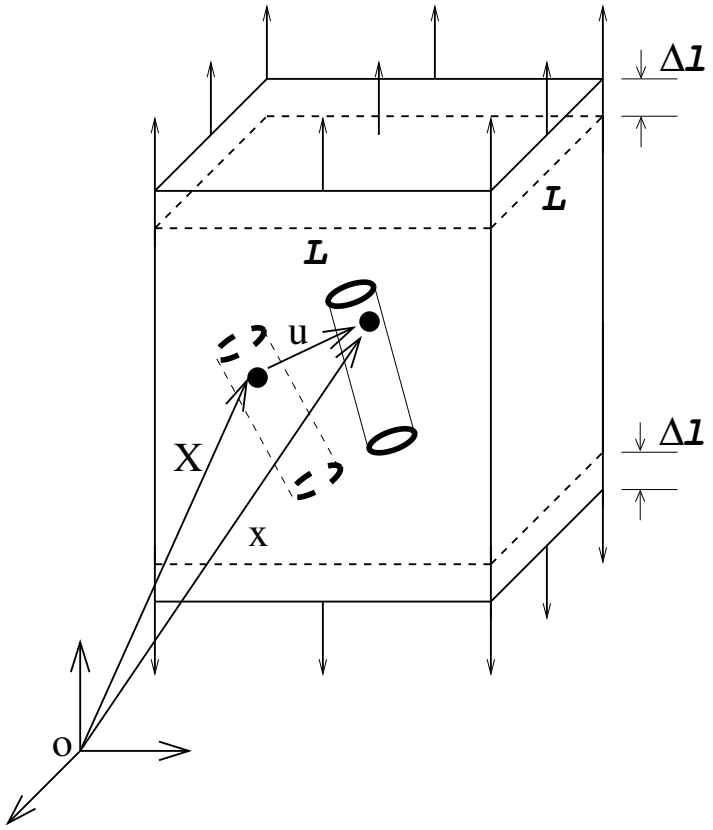

Figure 10.3: Illustration of the incremental loading procedure. Dashed lines correspond to increment i and solid lines to increment i+1. The bold ends on the CNT indicate that its ends are fixed.

calculations. In MD simulations, the virial stress is obtained from kinetic and potential energy contributions. However, in molecular statics, the stress is obtained only from the potential energy, that is

$$\sigma_{ij}^{\alpha} = -\frac{1}{V^{\alpha}} \sum_{\beta} F_i^{\alpha\beta} r_j^{\alpha\beta} \tag{10.4}$$

where V^{α} is the atomic volume of some atom α, $F_i^{\alpha\beta}$ is the i^{th}-component of the force between atom α and atom β computed from the derivative of the potential. $r_j^{\alpha\beta}$ is the j-component of the distance between atom α and β [52; 73]. The system stress is then

calculated as the summation of atomic stresses

$$\sigma_{ij} = -\frac{1}{V}\sum_{\alpha}\sum_{\beta} F_i^{\alpha\beta} r_j^{\alpha\beta} \tag{10.5}$$

Remark 4: Mathematically, the general incremental constrained minimization algorithm may be written as

$$\begin{aligned} \underset{\mathbf{\Delta r^i}}{\text{minimize}} \quad & E(r_1^{i-1} + \Delta r_1^i, \ldots, r_n^{i-1} + \Delta r_n^i) \\ \text{subject to} \quad & r_j^i = r_{j0}^i \ (j \in \text{CNTs end}) \end{aligned} \tag{10.6}$$

Where r_j^i denotes the displacement in i^{th} iteration of atom j. r_{j0}^i is the prescribed displacement, obtained as the cell is being stretched, for atom j in i^{th} iteration. This procedure corresponds to a macroscopic uniaxial tension test. It is expected that by increasing the number of nanotubes in the cell, a macroscopically isotropic response could be obtained in every direction.

Chapter 11

Results and discussion

The computations are performed using LAMMPS [56] on a SiCortex parallel machine employing 600 processors. An axial strain is applied in each direction at an increment of 0.01% until 5% strain is reached. The stress is computed once the constrained minimization has converged and the Young's modulus is then extracted from the slope of the stress-strain curves. In our simulations, a (5,5) armchair SWCNT with length 2 nm is employed to construct the SWCNT aggregates, hence each CNT consists of 160 atoms.

11.1 Comparison with MD simulations

First the stress-strain results obtained with the proposed method is compared to molecular dynamics simulation with a microcanonical ensemble (NVE). In the MD method, strains are applied in the same manner as the proposed method (See Section 2.3) however NVE is used to update atoms positions. The length of the cell is increased by 0.05% strain in each iteration until 5% strain is reached. In each iteration the system is allowed to equilibrate for 2,000 time steps and the stresses are obtained by averaging the results in the next 2,000 production time steps. The results, shown in Figure 11.1, were obtained for 25 CNTs. It is interesting to note that while the MD simulation begins at a temperature that is nearly 0 degrees Kelvin (before the strain is applied), when it reaches 5% strain the temperature increases to 0.8 degrees Kelvin. Thus due to the slow loading process and the linear stress-strain relations, most of the external work is transformed into a potential energy while the

temperature slowly increases in the simulation.

For this particular case, the proposed molecular mechanics approach show very good agreement with MD simulations. However, the corresponding computing time for MD was 18 hours while only 1 hour was needed for the molecular mechanics computation. To emphasize this point we show in Table 11.1 the CPU time that it takes to run an MD simulation versus the CPU time that takes the proposed molecular mechanics method to converge, for a varying number of nanotubes. The Table also reports the time steps versus the optimization iterations required by each method. It can clearly be seen that the MD simulation quickly becomes expensive and hence impossible to solve with many atoms in the system. On the other hand, while the optimization is limited to some particular applications, the proposed method could be used to solve these huge size optimization problems.

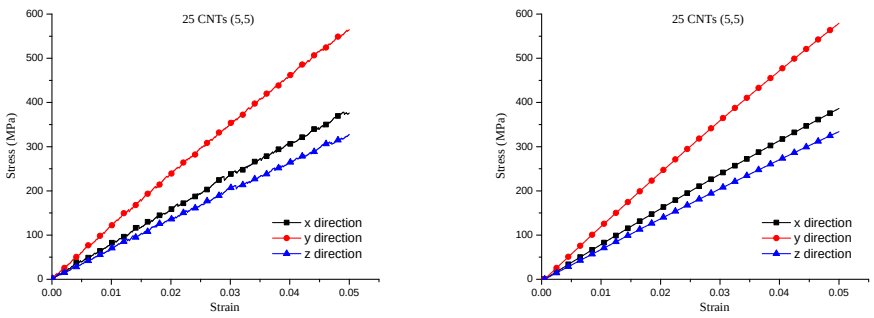

(a) (b)

Figure 11.1: Stress-strain curve for 25-(5,5) CNTs using (a) Molecular Statics (b) Molecular Dynamics

Table 11.1: Comparison between MD simulations and the proposed molecular mechanics method for increasing number of nanotubes. The problem was run on a SiCortex parallel machine with 600 processors

Number of CNTs		5	10	15	20	25
Proposed method	Time(hrs)	0.9	1.0	1.0	1.5	2.0
	Iterations	7761	7188	9492	6879	7206
Molecular Dynamics	Time(hrs)	67.6	92.9	75.0	137.5	205.0
	time steps	6.0×10^6	6.0×10^6	6.0×10^6	6.0×10^6	6.0×10^6

11.2 Studies with increasing number of randomly dispersed CNTs at constant density

Figure 11.2 illustrates the stress-strain response obtained for 50-, 200-, 800-, and 1000- (5,5) armchair CNT aggregates, with a constant density 0.08g/cm^3 computed as

$$\rho = \frac{1.993 \times 10^{-26} \cdot N}{V} \tag{11.1}$$

where N is the number of atoms in the simulation cell, 1.993×10^{-26} kg is the atom mass of Carbon-12 and V is the simulation volume. To study CNTs dispersion, the so-called order parameter S [78] is employed. This parameter is typically used to indicate isotropy and randomness of crystals and is defined by

$$S = < \frac{3\cos^2\theta - 1}{2} > \tag{11.2}$$

where θ is the angle between the CNTs axis and some local director and the brackets denote a spatial average. For example, an isotropic sample is indicated by $S = 0$ and a perfectly aligned sample by $S = 1$. The order parameter for the CNTs distribution studied in this study is given in Table 11.2. The results show that S is converging to 0 as the number of CNTs in the system increases, which demonstrate the randomness and isotropic characteristic of the configuration.

Remark 5: *Eq. 11.1 indicates that as the number of atoms in the cell increase, the volume of the simulation box must also increase accordingly, to keep a constant density.*

Table 11.2: Order parameters for 50-,200-,800-, and 1000- CNT aggregates

Number of CNTs	50	200	800	1000
Order Parameter	-0.0577	0.0197	0.0171	0.0078

The results in Figure 11.2 infer that the macroscopic response becomes more isotropic, or in other words the uncertainty of the response reduces, as the number of nanotubes in the cell increases.

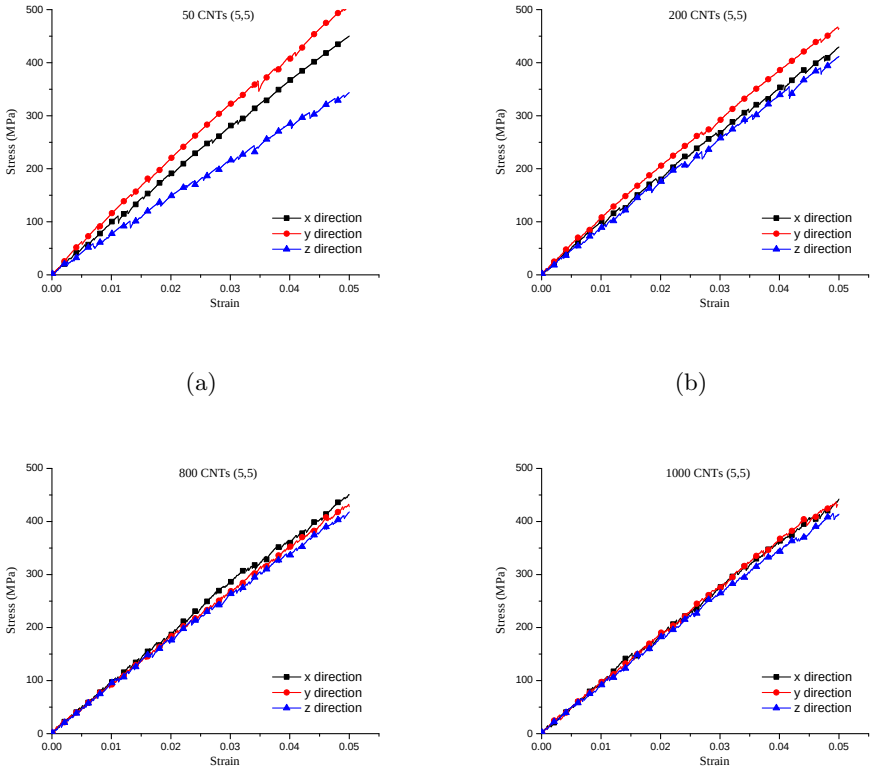

Figure 11.2: stress-strain curves obtained from atomistic simulations of 50-, 200-, 800- and 1000-(5,5) armchair CNT aggregates

The CNT structures produce linear stress-strain curves within 5% strain and there is no apparent nonlinearity observed. The Young's modulus, calculated as the average in x,y

and z directions up to 5% strain, is approximately 8.6 GPa for CNT aggregates with 1000 nanotubes. This number is significantly smaller than the reported results for one SWCNT Young's modulus, which ranges from $0.44 - 5.5$ TPa [68]. One reason for such a huge difference is due to the definition of an atomic volume when computing the stress. In a typical one SWCNT tension simulation, the atomic volume is assumed as an artificial thin walled cylinder with a 0.34 nm wall thickness [63; 61]. However, for CNTs structures, the atomic volume is defined as the entire volume, which includes the hollow volume inside the tube and between tubes. Due to the extremely small artificial volume for a SWCNT, the stress computed using equation (10.5) is much lager, and hence the extracted Young's modulus. In practice however, CNTs are not individually synthesized but rather randomly agglomerated bundles [71].

The coefficients of variance of the computed Young's modulus and the normal stresses σ_{ii} at every direction, as function of the number of CNTs are shown in Figure 11.3 and Figure 11.4, respectively. It can be observed that when the number of CNTs grows to 700 and above, which corresponds to $112,000$ atoms, the results converge with a coefficient of variance that is less than 4% and and the Young's modulus mean is 8.6 GPa. Along these lines, it is estimated that as the number of nanotubes in the system increases, while keeping the density constant, the coefficients of variance will decay even more and the results will become more accurate in terms of obtaining an isotropic response in all directions.

Remark 6: *While it is difficult to quantify the number of atoms required to obtain acceptable results given different density levels, several conclusions can still be made. Assuming that 800 CNTs (*$128,000$ *atoms) provide an acceptable result with respect to the coefficient of variance, with a simulation volume of* 3.2×10^{-23} m^3 *then (i) keeping the volume fixed and adding more atoms will give acceptable results, and (ii) keeping the number of atoms fixed at* $128,000$ *and reducing the simulation volumes will also give acceptable results. In general, once an acceptable result is obtained, another one can be obtained without trial and error by simply increasing atoms in the simulation or decreasing the simulation volume.*

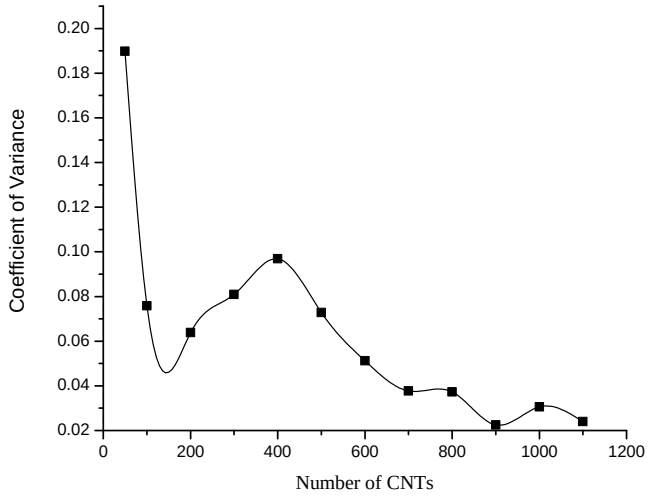

Figure 11.3: The coefficients of variance indicating the variation of the Young modulus from its average, obtained with increasing number of CNTs at constant density.

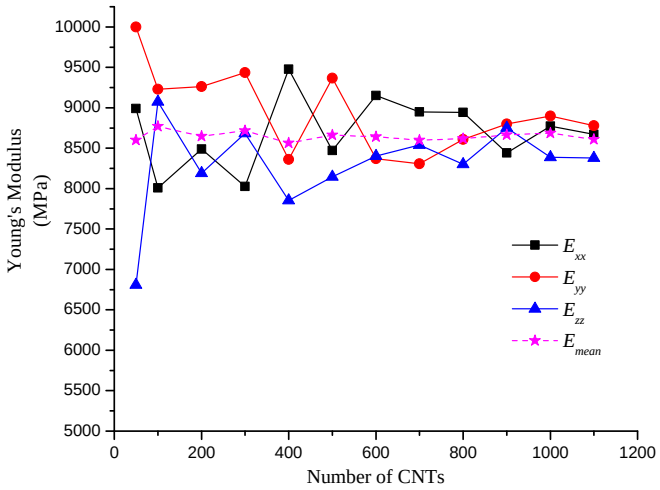

Figure 11.4: Young's modulus at each direction.

11.3 Studies with 800 randomly dispersed CNTs and increasing density

Another set of simulations is performed to investigate Young's modulus change with respect to density variance. The results are present in Table 11.3 and Figure 11.5.

Density(g/cm^3)	0.1	0.12	0.14	0.16
Young's Modulus(GPa)	10.87	12.96	15.28	17.55
Coefficient of Variance	3.8%	2.6%	2.9%	3.4%

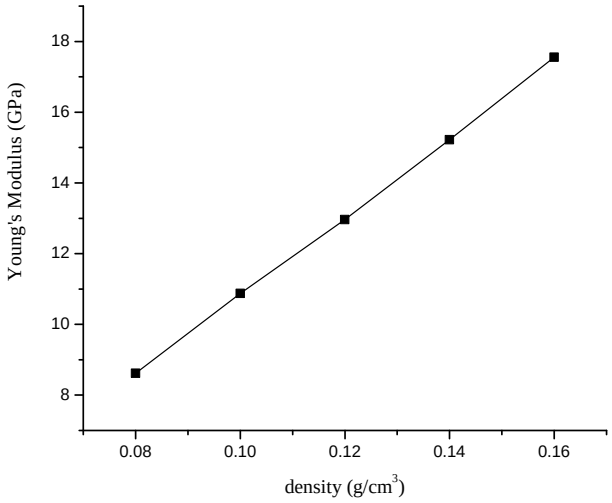

Figure 11.5: Young's modulus for different densities

All simulations were performed using 800-(5,5) randomly dispersed CNTs so the simulation volume decreased accordingly. As discussed above, the simulation results should have good homogenous and isotropic properties since the same amount of $128,000$ atoms is employed in a smaller simulation volume, which shows comparable small coefficients of variance in Table 11.2. A linear relation between the density and Young's modulus for (5,5) CNT aggregates can clearly be observed in Figure 11.5.

Part V

Conclusions

Chapter 12

Conclusions

12.1 Summary of Contributions

The author's main contributions are in (i) computational fracture mechanics, the developments of XFEM methods for computation of Strain Energy Release Rates [41], and (ii) computational nanomechanics, molecular statics methods to study SWCNT aggregates [40]. These contributions are summarized here:

i. **XFEM-High order enrichment functions:** High order enrichment functions are developed and incorporated in XFEM to show that high accuracy can be obtained when combining these functions with Irwin's integral for extraction of SERRs. The high order terms are derived from the asymptotic fields for the displacement components near the crack tip and implemented in an XFEM Matlab code..

ii. **XFEM-Analytical formulation of Irwin's integral:** Closed form of analytical formulation to extract SERRs is developed based on the classical Irwin integral and the special capabilities of XFEM. The formulation is derived in polar coordinates and no special postprocessing is required to compute the SERRs. The proposed approach can be applied to arbitrary crack settings. The results indicate that high order enrichment functions have significant effect on the convergence. When the integral limits tend to zero, simpler SERR expressions are obtained and high order terms vanish. Nonetheless, these terms contribute indirectly via coefficients of first

order terms.The approach is simple and may be an alternative to the popular J-integral method..

iii. **XFEM-Numerical implementation of Irwin's integral:** The proposed approach has also been implemented numerically and served as a verification of the analytical method. In addition one can directly employ the numerical approach and obtain results for more complicated applications and various other element types.

iv. **Nanomechanics simulation**: The molecular mechanics method presented in the thesis is based on an incremental constrained minimization methodology. At each increment the simulation cell is deformed (similar to a displacement control in continuous systems) and the energy is minimized while the atoms are mapped to their new positions. It is assumed that their relative position in the cell does not change and that their ends are fixed (constrained to the simulation box). This approach produced similar results as the MD method with NVE ensembles but the convergence of the proposed method is orders of magnitude faster. Moreover, it is shown that an isotropic behavior is obtained when the number of arbitrary distributed CNTs in the aggregates increases, which is an intuitive result but would require tremendous computational resources if studied by MD.

12.2 Future Work

i. **XFEM**: The current quadrature rule is inefficient for the type of crack tip asymptotic functions that are used. Improving the numerical integration will be the subject of future work. With the use of dedicated quadrature rules that exploit the tip asymptotic behavior, the method has the potential of becoming competitive. In addition, the proposed approach can be extended to bi-materials, 3D problems and other element types.

ii. **Nanomechanics**: The technique introduced in this study may provide a bridge between atomistic and continuum models, as the isotropic stress-strain relation may be incorporated by concurrent multiscale techniques and directly be employed as the

constitutive law in continuum homogenized formulations.

Part VI

Bibliography

Bibliography

[1] L. Banks-Sills and O. Dolev. The conservative M-integral for thermal-elastic problems. *International journal of fracture*, 125(1):149–170, 2004.

[2] L. Banks-Sills and D. Sherman. Comparison of methods for calculating stress intensity factors with quarter-point elements. *International Journal of Fracture*, 32:127–140, 1986.

[3] R. S. Barsoum. One the use of isoparametric finite elements in linear fracture mechanics. *International Journal for Numerical Methods in Engineering*, 10:25–37, 1976.

[4] T. Belytschko and T. Black. Elastic crack growth in finite elements with minimal remeshing. *International Journal for Numerical Methods in Engineering*, 45:601–620, 1999.

[5] T. Belytschko, S. P. Xiao, G. C. Schatz, and R. S. Ruoff. Atomistic simulations of nanotube fracture. *Phys. Rev. B*, 65:235430, Jun 2002.

[6] Ted Belytschko, Robert Gracie, and Giulio Ventura. A review of extended/generalized finite element methods for material modeling. *Modelling and Simulation in Materials Science and Engineering*, 17(4):043001, 2009.

[7] Donald W. Brenner. Empirical potential for hydrocarbons for use in simulating the chemical vapor deposition of diamond films. *Phys. Rev. B*, 42:9458–9471, Nov 1990.

[8] Donald W Brenner, Olga A Shenderova, Judith A Harrison, Steven J Stuart, Boris Ni, and Susan B Sinnott. A second-generation reactive empirical bond order (rebo)

potential energy expression for hydrocarbons. *Journal of Physics: Condensed Matter*, 14(4):783–802, 2002.

[9] Theodore E. Brown, Bruce E. Bursten, and H. Eugene H Lemay. *Chemistry: The Central Science*. Prentice-Hall, 1999.

[10] Markus J. Buehler, Yong Kong, and Huajian Gao. Deformation mechanisms of very long single-wall carbon nanotubes subject to compressive loading. *Journal of Engineering Materials and Technology*, 126(3):245–249, 2004.

[11] S. K. Chan, I. S. Tuba, and W. K. Wilson. On the finite element method in linear fracture mechanics. *Engineering Fracture Mechanics*, 2:1–17, 1970.

[12] Quan Chen, Craig Saltiel, Siva Manickavasagam, Linda S. Schadler, Richard W. Siegel, and Hoichang Yang. Aggregation behavior of single-walled carbon nanotubes in dilute aqueous suspension. *Journal of Colloid and Interface Science*, 280(1):91 – 97, 2004.

[13] X. Chen and Y. Huang. Nanomechanics modeling and simulation of carbon nanotubes. *Journal of Engineering Mechanics*, 134:211–216, 2008.

[14] Zhihong Chen, Joerg Appenzeller, Yu-Ming Lin, Jennifer Sippel-Oakley, Andrew G. Rinzler, Jinyao Tang, Shalom J. Wind, Paul M. Solomon, and Phaedon Avouris. An integrated logic circuit assembled on a single carbon nanotube. *Science*, 24:1735, 2006.

[15] Jonathan N. Coleman, Umar Khan, Werner J. Blau, and Yurii K. Gunko. Small but strong: A review of the mechanical properties of carbon nanotubepolymer composites. *Carbon*, 44:1624–1652, 2006.

[16] V. R. Coluci, S. O. Dantas, A. Jorio, and D. S. Galvão. Mechanical properties of carbon nanotube networks by molecular mechanics and impact molecular dynamics calculations. *Phys. Rev. B*, 75:075417, Feb 2007.

[17] H. Dai. Carbon nanotubes: opportunities and challenges. *Surface Science*, 500:218–241, 2002.

[18] P. Destuynder, S. Lescure, and M. Djaoua. Some remarks on elastic fracture mechanics. *Journal de mécanique théorique et appliquée*, 2(1):113–135, 1983.

[19] John E. Dolbow. *An Extended Finite Element Method with Discontinuous Enrichment for Applied Mechanics*. PhD thesis, Northwestern University, 1999.

[20] C. A. Duarte, I. Babuska, and J. T. Oden. Generalized finite element methods for three-dimensional structural mechanics problems. *Computers & Structures*, 77(2):215–232, 2000.

[21] C. A. Duarte, O. N. Hamzeh, T. J. Liszka, and W. W. Tworzydlo. A generalized finite element method for the simulation of three-dimensional dynamic crack propagation. *Computer Methods in Applied Mechanics and Engineering*, 190(15-17):2227–2262, 2001.

[22] F. Erdogan and G.C. Sih. On the crack extension in plane loading and transverse shear. *Journal of Basic Mechanics*, 85:519–527, 1963.

[23] H. L. Ewalds and R. J. H. Wanhill. *Fracture Mechanics*. Edward Arnold, 1984.

[24] S.A. Fawaz. Application of the virtual crack closure technique to calculate stress intensity factors for through cracks with an elliptical crack front. *Engineering Fracture Mechanics*, 59(3):327 – 342, 1998.

[25] S.J.V. Frankland, V.M. Harik, G.M. Odegard, D.W. Brenner, and T.S. Gates. The stress-strain behavior of polymer-nanotube composites from molecular dynamics simulation. *Composites Science and Technology*, 63:1655–1661, 2003.

[26] T. P. Fries and T. Belytschko. The extended/generalized finite element method: An overview of the method and its applications. *International Journal for Numerical Methods in Engineering*, 84(3):253–304, 2010.

[27] F.H. Gojny, M.H.G. Wichmann, U. Kopke, B. Fiedler, and K. Schulte. Carbon nanotube-reinforced epoxy-composites: enhanced stiffness and fracture toughness at low nanotube content. *Composites Science and Technology*, 64:2363–2371, 2004.

[28] Benjamin S. Harrison and Anthony Atala. Carbon nanotube applications for tissue engineering. *Biomaterials*, 28:344–353, 2006.

[29] Chunnian He, Naiqin Zhao, Chunsheng Shi, Xiwen Du, Jiajun Li, Haipeng Li, and Qingran Cui. An approach to obtaining homogeneously dispersed carbon nanotubes in al powders for preparing reinforced al-matrix composites. *Advanced Materials*, 19:1128–1132, 2007.

[30] T. K. Hellen. On the method of virtual crack extensions. *International Journal for Numerical Methods in Engineering*, 9(1):187–207, 1975.

[31] T. J. R. Hughes. *The Finite Element Method: Linear Static And Dynamic Finite Element Analysis*. Prentice-Hall, Inc., 1987.

[32] M.A. Hussain, S.L. Pu, and J.H. Underwood. Strain energy release rate for a crack under combined mode I and mode II. *Fracture Analysis ASTM STP*, 560:2–28, 1974.

[33] Sumio Iijima. Helical microtubules of graphitic carbon. *Nature*, 354:56–58, 1991.

[34] G. Irwin. Handbuch der physik. *Bd. 6. Elastizitaet und Plastizitaet*, pages 551–590, 1958.

[35] Ali Javey, Jing Guo, Qian Wang, Mark Lundstrom, and Hongjie Dai. Ballistic carbon nanotube field-effect transistors. *Nature*, 424:654–657, 2003.

[36] Y. Jin and F. G. Yuan. Simulation of elastic properties of single-walled carbon nanotubes. *Composites Science and Technology*, 63:1507–1515, 2003.

[37] M. Kirca, X. Yang, and A.C. To. A stochastic algorithm for modeling heat welded random carbon nanotube network. *Computer Methods in Applied Mechanics and Engineering*, 259(0):1 – 9, 2013.

[38] A. Krishnan, E. Dujardin, T.W. Ebbesen, P.N. Yianilos, and M.M.J. Treacy. Young's modulus of single-walled nanotubes. *Physical Review B*, 58:14013–14019, 1998.

[39] R. Krueger. The virtual crack closure technique: history, approach and applications. Technical report, NASA, 2002. NASA/CR-2002-211628, ICASE Report No. 2002-10.

[40] Mengyu Lan and Haim Waisman. Mechanics of swcnt aggregates studied by incremental constrained minimization. *Journal of Nanomechanics and Micromechanics*, 2(2):15–22, 2011.

[41] Mengyu Lan, Haim Waisman, and Isaac Harari. A general direct analytical method to extract strain energy release rates from Irwin's integral using XFEM. *Summitted to International Journal for Numerical Methods in Engineering*, 2013.

[42] F. Z. Li, C. F. Shih, and A. Needleman. A comparison of methods for calculating energy release rates. *Engineering Fracture Mechanics*, 21(2):405–421, 1985.

[43] K.M. Liew, X.Q. He, and C.H. Wong. On the study of elastic and plastic properties of multi-walled carbon nanotubes under axial tension using molecular dynamics simulation. *Acta Materialia*, 52:2521–2527, 2004.

[44] K.M. Liew, C.H. Wong, and M.J. Tan. Tensile and compressive properties of carbon nanotube bundles. *Acta Materialia*, 54:225–231, 2006.

[45] X. Y. Liu, Q. Z. Xiao, and B. L. Karihaloo. XFEM for direct evaluation of mixed mode SIFs in homogeneous and bi-materials. *International Journal for Numerical Methods in Engineering*, 59:1103–1118, 2004.

[46] O. Lourie, D.M. Cox, and H.D. Wagner. Buckling and collapse of embedded carbon nanotubes. *Physical Review Letters*, 81:1638–1641, 1998.

[47] S.K. Maiti and R.A. Smith. Comparison of the criteria for mixed mode brittle fracture based on the preinstability stress-strain field. part ii: pure shear and uniaxial loading. *Journal of Fracture*, 24:5–22, 1984.

[48] Ashish Modi, Nikhil Koratkar, Eric Lass, Bingqing Wei, and Pulickel M. Ajayan. Miniaturized gas ionization sensors using carbon nanotubes. *Nature*, 424:171–174, 2003.

[49] N. Moës, J. Dolbow, and T. Belytschko. A finite element method for crack growth without remeshing. *International Journal for Numerical Methods in Engineering*, 46:131–150, 1999.

[50] N. Moës, A. Gravouil, and T. Belytschko. Non-planar 3d crack growth by the extended finite element and level setspart i: Mechanical model. *International Journal for Numerical Methods in Engineering*, 53(11):2549–2568, 2002.

[51] B. Moran and C. F. Shih. A general treatment of crack tip contour integrals. *International Journal of Fracture*, 35:295–310, 1987.

[52] O. H. Nielsen and Richard M. Martin. Quantum-mechanical theory of stress and force. *Physical Revew B*, 32:3780–3791, 1985.

[53] S. Osher and J. A. Sethian. Fronts propagating with curvature-dependent speed: Algorithms based on Hamilton-Jacobi formulations. *Journal of Computation Physics*, 79:12–49, 1988.

[54] Antonio Pantano, David M. Parks, and Mary C. Boyce. Mechanics of deformation of single- and multi-wall carbon nanotubes. *Journal of the Mechanics and Physics of Solids*, 52:789 – 821, 2004.

[55] D. M. Parks. A stiffness derivative finite element technique for determination of crack tip stress intensity factors. *International Journal of Fracture*, 10(4):487–502, 1974.

[56] S. Plimpton. Fast parallel algorithms for short-range molecular dynamics. *Journal of Computational Physics*, 117:1–19, 1995.

[57] Dewei Qi, Jeffrey Hinkley, and Gouwei He. Molecular dynamics simulation of thermal and mechanical properties of polyimidecarbon-nanotube composites. *Modelling and Simulation in Materials Science and Engineering*, 13:493–507, 2005.

[58] J. Réthoré, S. Roux, and F. Hild. Hybrid analytical and extended finite element method (hax-fem): A new enrichment procedure for cracked solids. *International journal for numerical methods in engineering*, 81(3):269–285, 2010.

[59] R.F.Decker. *Source Book on Maraging Steels*. American Society for Metals, 1979.

[60] J. R. Rice. A path independent integral and the approximate analysis of strain concentration by notches and cracks. *Journal of Applied Mechanics*, 35:379–386, 1968.

[61] Rodney S. Ruoff, Dong Qian, and Wing Kam Liu. Mechanical properties of carbon nanotubes: theoretical predictions and experimental measurements. *Comptes Rendus Physique*, 4:993–1008, 2003.

[62] E. F. Rybicki and M. F. Kanninen. A finite element calculation of stress intensity factors by a modified crack closure integral. *Engineering Fracture Mechanics*, 9:931–938, 1977.

[63] Yahachi Saito, Shunji Bandow, Masato Tomita, and Takayoshi Hayashi. Interlayer spacings in carbon nanotubes. *Nature*, 48:1907–1909, 1993.

[64] J. A. Sethian. *Level Set Methods and Fast Marching Methods : Evolving Interfaces in Computational Geometry, Fluid Mechanics, Computer Vision, and Materials Science.* Cambridge University Press, 1999.

[65] C. F. Shih, H. G. Delorenzi, and M. D. German. Crack extension modeling with singular quadratic isoparametric elements. *International Journal of Fracture*, 1:647–651, 1976.

[66] K. N. Shivakumar, P. W. Tan, and J. C. Newman. A virtual crack-closure technique for calculating stress intensity factors for cracked three dimensional bodies. *International Journal of Fracture*, 36:R43–R50, 1988.

[67] Ken Shoemake. *Graphics Gems III.* Academic Press Professional, Inc., San Diego, CA, USA, 1992.

[68] M.M. Shokrieh and R. Rafiee. A review of the mechanical properties of isolated carbon nanotubes and carbon nanotube composites. *Mechanics of Composite Materials*, 46:155–172, 2010.

[69] Steven J. Stuart, Alan B. Tutein, and Judith A Harrison. A reactive potential for hydrocarbons with intermolecular interactions. *Journal of Chemical Physicsr*, 112:6472–6486, 2000.

[70] N. Sukumar, D. L Chopp, N. Moës, and T. Belytschko. Modeling holes and inclusions by level sets in the extended finite element method. *Computer Methods in Applied Mechanics and Engineering*, 190(46-47):6183–6200, 2000.

[71] Andreas Thess, Roland Lee, Pavel Nikolaev, Hongjie Dai, Pierre Petit, Jerome Robert, Chunhui Xu, Young Hee Lee, Seong Gon Kim, Andrew G. Rinzler, Daniel T. Colbert, Gustavo E. Scuseria, David Tománek, John E. Fischer, and Richard E. Smalley. Crystalline ropes of metallic carbon nanotubes. *Science*, 273:483 – 487, 1996.

[72] M.M. Treacy, T.W. Ebbesen, and J.M. Gibson. Exceptionally high young's modulus observed for individual carbon nanotubes. *Nature*, 38:670–680, 1996.

[73] V. Vitek and T. Egami. Atomic level stresses in solids and liquids. *Physica Status Solidi B*, 144:145–156, 1987.

[74] Haim Waisman. An analytical stiffness derivative extended finite element technique for extraction of crack tip strain energy release rates. *Engineering Fracture Mechanics*, 77(16):3204 – 3215, 2010.

[75] Haim Waisman and Luc Berger-Vergiat. An adaptive domain decomposition preconditioner for crack propagation problems modeled by XFEM. *International Journal for Multiscale Computational Engineering*, 2013.

[76] S. S. Wang, J. F. Yau, and H. T. Corten. A mixed-mode crack analysis of rectilinear anisotropic solids using conservation laws of elasticity. *International Journal of Fracture*, 16:247–259, 1980.

[77] M.L. Williams. On the stress distribution at the base of a stationary crack. *Journal of Applied Mechanics*, pages 101–106, 1957.

[78] Mark R. Wilson. Determination of order parameters in realistic atom-based models of liquid crystal systems. *Journal of Molecular Liquids*, 68:23–31, 1996.

[79] W. K. Wilson. *Combined mode fracture mechanics*. PhD thesis, University of Pittsburgh, 1969.

[80] B. I. Yakobson, C. J. Brabec, and J. Bernholc. Nanomechanics of carbon tubes: instabilities beyond linear response. *Physical Review Letters*, 76:2511–2514, 1996.

[81] J. F Yau, S. S. Wang, and H. T. Corten. A mixed-mode crack analysis of isotropic solids using conservation-laws of elasticity. *Journal of Applied Mechanics*, 47(2):335–341, 1980.

[82] M.F. Yu, O. Lourie, M.J. Dyer, K. Moloni, T.F. Kelly, and R.S. Ruo. Strength and breaking mechanism of multiwalled carbon nanotubes under tensile load. *Science*, 287:637–640, 2000.

[83] A. Zamani, R. Gracie, and M.R. Eslami. Higher order tip enrichment of extended finite element method in thermoelasticity. *Computational Mechanics*, 46(6):851–866, 2010.

[84] Arash Zamani, Robert Gracie, and M. Reza Eslami. Cohesive and non-cohesive fracture by higher-order enrichment of XFEM. *International Journal for Numerical Methods in Engineering*, 90(4):452–483, 2012.

Part VII

Appendices

Appendix A

Extracting SERRs from Irwin's Integral

A.1 Expansion of leading high order functions

Terms of order $\sqrt{r}$:

$$u_1 = \frac{K_{I1}r^{1/2}}{2\mu\sqrt{2\pi}}\{\cos\frac{1}{2}\theta(\kappa-1)+\sin\frac{\theta}{2}\sin\theta\}+\frac{K_{II1}r^{1/2}}{2\mu\sqrt{2\pi}}\{\sin\frac{1}{2}\theta(\kappa+1)+\cos\frac{\theta}{2}\sin\theta\} \quad (A.1)$$

$$v_1 = \frac{K_{I1}r^{1/2}}{2\mu\sqrt{2\pi}}\{\sin\frac{1}{2}\theta(\kappa+1)-\cos\frac{\theta}{2}\sin\theta\}+\frac{K_{II1}r^{1/2}}{2\mu\sqrt{2\pi}}\{\cos\frac{1}{2}\theta(1-\kappa)+\sin\frac{\theta}{2}\sin\theta\} \quad (A.2)$$

Terms of order r:

$$u_2 = \frac{K_{I2}r}{4\mu\sqrt{2\pi}}\cos\theta\{\kappa+1\}+\frac{K_{II2}r}{4\mu\sqrt{2\pi}}\sin\theta\{\kappa+1\} \quad (A.3)$$

$$v_2 = \frac{K_{I2}r}{4\mu\sqrt{2\pi}}\sin\theta\{\kappa-3\}+\frac{K_{II2}r}{4\mu\sqrt{2\pi}}\cos\theta\{-\kappa-1\} \quad (A.4)$$

Terms of order $r^{3/2}$:

$$\begin{aligned} u_3 =& \frac{K_{I3}r^{3/2}}{6\mu\sqrt{2\pi}}\{\cos\frac{1}{2}\theta(\kappa-1)-2\sin\theta\sin\frac{\theta}{2}(\kappa+\frac{1}{2})\} \\ &+\frac{K_{II3}r^{3/2}}{6\mu\sqrt{2\pi}}\{\sin\frac{1}{2}\theta(-\kappa-1)+2\sin\theta\cos\frac{\theta}{2}(\kappa+\frac{5}{2})\} \end{aligned} \quad (A.5)$$

$$\begin{aligned} v_3 =& \frac{K_{I3}r^{3/2}}{6\mu\sqrt{2\pi}}\{2\sin\theta\cos\frac{\theta}{2}(\kappa-\frac{1}{2})-\sin\frac{1}{2}\theta(\kappa+1)\} \\ &+\frac{K_{II3}r^{3/2}}{6\mu\sqrt{2\pi}}\{-2\sin\theta\sin\frac{\theta}{2}(-\kappa+\frac{5}{2})+\cos\frac{1}{2}\theta(1-\kappa)\} \end{aligned} \quad (A.6)$$

Terms of order r^2:

$$u_4 = \frac{K_{I4} r^2}{8\mu\sqrt{2\pi}}\{(\kappa+3)\cos 2\theta - 2\} + \frac{K_{II4} r^2}{8\mu\sqrt{2\pi}}\{(\kappa+1)\sin 2\theta\} \tag{A.7}$$

$$v_4 = \frac{K_{I4} r^2}{8\mu\sqrt{2\pi}}\{(\kappa-3)\sin 2\theta\} + \frac{K_{II4} r^2}{8\mu\sqrt{2\pi}}\{(-\kappa+1)\cos 2\theta - 2\} \tag{A.8}$$

A.2 Derivatives of high order functions used for XFEM implementation

The crack-tip functions in Eq. (3.14) are given by

$$\begin{cases} F_1 & = \sqrt{r}\sin\frac{\theta}{2} \\ F_2 & = \sqrt{r}\cos\frac{\theta}{2} \\ F_3 & = \sqrt{r}\sin\theta\sin\frac{\theta}{2} \\ F_4 & = \sqrt{r}\sin\theta\cos\frac{\theta}{2} \\ F_5 & = r\cos\theta \\ F_6 & = r\sin\theta \\ F_7 & = r^{3/2}\cos\frac{\theta}{2} \\ F_8 & = r^{3/2}\sin\frac{\theta}{2} \\ F_9 & = r^{3/2}\sin\theta\sin\frac{\theta}{2} \\ F_{10} & = r^{3/2}\sin\theta\cos\frac{\theta}{2} \\ F_{11} & = r^2 \\ F_{12} & = r^2\sin 2\theta \\ F_{13} & = r^2\cos 2\theta \end{cases} \tag{A.9}$$

Their first derivatives with respect to r and θ are given as

$$\begin{cases} f_1^r &= \frac{\partial F_1}{\partial r} = \frac{1}{2\sqrt{r}} \sin\frac{\theta}{2} \\ f_2^r &= \frac{\partial F_2}{\partial r} = \frac{1}{2\sqrt{r}} \cos\frac{\theta}{2} \\ f_3^r &= \frac{\partial F_3}{\partial r} = \frac{1}{2\sqrt{r}} \sin\frac{\theta}{2} \sin\theta \\ f_4^r &= \frac{\partial F_4}{\partial r} = \frac{1}{2\sqrt{r}} \cos\frac{\theta}{2} \sin\theta \\ f_5^r &= \frac{\partial F_5}{\partial r} = \cos\theta \\ f_6^r &= \frac{\partial F_6}{\partial r} = \sin\theta \\ f_7^r &= \frac{\partial F_7}{\partial r} = \frac{3}{2}\sqrt{r} \cos\frac{\theta}{2} \\ f_8^r &= \frac{\partial F_8}{\partial r} = \frac{3}{2}\sqrt{r} \sin\frac{\theta}{2} \\ f_9^r &= \frac{\partial F_9}{\partial r} = \frac{3}{2}\sqrt{r} \sin\frac{\theta}{2} \sin\theta \\ f_{10}^r &= \frac{\partial F_{10}}{\partial r} = \frac{3}{2}\sqrt{r} \cos\frac{\theta}{2} \sin\theta \\ f_{11}^r &= \frac{\partial F_{11}}{\partial r} = 2r \\ f_{12}^r &= \frac{\partial F_{12}}{\partial r} = 2r \sin 2\theta \\ f_{13}^r &= \frac{\partial F_{13}}{\partial r} = 2r \cos 2\theta \end{cases} \tag{A.10}$$

$$
\begin{cases}
f_1^\theta &= \frac{\partial F_1}{\partial \theta} = \frac{\sqrt{r}}{2}\cos\frac{\theta}{2} \\
f_2^\theta &= \frac{\partial F_2}{\partial \theta} = -\frac{\sqrt{r}}{2}\sin\frac{\theta}{2} \\
f_3^\theta &= \frac{\partial F_3}{\partial \theta} = \frac{\sqrt{r}}{2}\cos\frac{\theta}{2}\sin\theta + \sqrt{r}\sin\frac{\theta}{2}\cos\theta \\
f_4^\theta &= \frac{\partial F_4}{\partial \theta} = \frac{\sqrt{r}}{2}\cos\frac{\theta}{2}\cos\theta - \sqrt{r}\sin\frac{\theta}{2}\sin\theta \\
f_5^\theta &= \frac{\partial F_5}{\partial \theta} = -r\sin\theta \\
f_6^\theta &= \frac{\partial F_6}{\partial \theta} = r\cos\theta \\
f_7^\theta &= \frac{\partial F_7}{\partial \theta} = -\frac{r^{3/2}}{2}\sin\frac{\theta}{2} \\
f_8^\theta &= \frac{\partial F_8}{\partial \theta} = \frac{r^{3/2}}{2}\cos\frac{\theta}{2} \\
f_9^\theta &= \frac{\partial F_9}{\partial \theta} = \frac{r^{3/2}}{2}\cos\frac{\theta}{2}\sin\theta + r^{3/2}\sin\frac{\theta}{2}\cos\theta \\
f_{10}^\theta &= \frac{\partial F_{10}}{\partial \theta} = -\frac{r^{3/2}}{2}\sin\frac{\theta}{2}\sin\theta + r^{3/2}\cos\frac{\theta}{2}\cos\theta \\
f_{11}^\theta &= \frac{\partial F_{11}}{\partial \theta} = 0 \\
f_{12}^\theta &= \frac{\partial F_{12}}{\partial \theta} = 2r^2\cos 2\theta \\
f_{13}^\theta &= \frac{\partial F_{13}}{\partial \theta} = -2r^2\sin 2\theta
\end{cases}
\tag{A.11}
$$

A.3 Derivation of Eqs. (4.10) and (4.11)

Starting from Eq (4.10), we first show that the even order terms will vanish. Assume $i = 2m$ where m is an integer, by substituting $\theta = -\pi$ into Eq (3.5)we will get

$$\begin{aligned}
u_{2m}(r,-\pi) =& \frac{r^{2m/2}}{2\mu n\sqrt{2\pi}}\{K_{I2m}[(\kappa+\frac{2m}{2}+(-1)^{2m})\cos\frac{2m}{2}(-\pi)-\frac{2m}{2}\cos(\frac{2m}{2}-2)(-\pi)] \\
&+K_{II2m}[(\kappa+\frac{2m}{2}-(-1)^{2m})\sin\frac{2m}{2}(-\pi)-\frac{2m}{2}\sin(\frac{2m}{2}-2)(-\pi)]\} \\
=& \frac{r^{m}}{2\mu n\sqrt{2\pi}}\{K_{I2m}[(\kappa+m+1)\cos(-m\pi)-m\cos(m-2)(-\pi)] \\
&+K_{II2m}[(\kappa+m-1)\sin(-m\pi)-m\sin(m-2)(-\pi)]\} \\
=& \frac{r^{m}}{2\mu n\sqrt{2\pi}}\{K_{I2m}[(\kappa+m+1)\cos(m\pi)-m\cos(m\pi)] \\
&+K_{II2m}[-(\kappa+m-1)\sin(m\pi)+m\sin(m\pi)]\} \\
=& \frac{r^{m}}{2\mu n\sqrt{2\pi}}\{K_{I2m}[(\kappa+1)\cos(m\pi)]
\end{aligned} \tag{A.12}$$

We then substitute $\theta = \pi$ into Eq (3.5) to arrive at

$$\begin{aligned}
u_{2m}(r,\pi) =& \frac{r^{2m/2}}{2\mu n\sqrt{2\pi}}\{K_{I2m}[(\kappa+\frac{2m}{2}+(-1)^{2m})\cos\frac{2m}{2}(\pi)-\frac{2m}{2}\cos(\frac{2m}{2}-2)(\pi)] \\
&+K_{II2m}[(\kappa+\frac{2m}{2}-(-1)^{2m})\sin\frac{2m}{2}(\pi)-\frac{2m}{2}\sin(\frac{2m}{2}-2)(\pi)]\} \\
=& \frac{r^{m}}{2\mu n\sqrt{2\pi}}\{K_{I2m}[(\kappa+m+1)\cos(m\pi)-m\cos(m-2)(\pi)] \\
&+K_{II2m}[(\kappa+m-1)\sin(m\pi)-m\sin(m-2)(\pi)]\} \\
=& \frac{r^{m}}{2\mu n\sqrt{2\pi}}\{K_{I2m}[(\kappa+m+1)\cos(m\pi)-m\cos(m\pi)] \\
&+K_{II2m}[(\kappa+m-1)\sin(m\pi)-m\sin(m\pi)]\} \\
=& \frac{r^{m}}{2\mu n\sqrt{2\pi}}\{K_{I2m}[(\kappa+1)\cos(m\pi)]
\end{aligned} \tag{A.13}$$

Finally we arrive at

$$u_{2m}(r,\pi) - u_{2m}(r,-\pi) = 0 \tag{A.14}$$

Next we substitute $\theta = -\pi$ into Eq (3.6)we will get

$$\begin{aligned}
v_{2m}(r,-\pi) =& \frac{r^{2m/2}}{2\mu n\sqrt{2\pi}}\{K_{I2m}[(\kappa - \frac{2m}{2} - (-1)^{2m})\sin\frac{2m}{2}(-\pi) + \frac{2m}{2}\sin(\frac{2m}{2}-2)(-\pi)] \\
&+K_{II2m}[(-\kappa + \frac{2m}{2} - (-1)^{2m})\cos\frac{2m}{2}(-\pi) - \frac{2m}{2}\cos(\frac{2m}{2}-2)(-\pi)]\} \\
=& \frac{r^{m}}{2\mu n\sqrt{2\pi}}\{K_{I2m}[(\kappa - m - 1)\sin(-m\pi) + m\sin(m-2)(-\pi)] \\
&+K_{II2m}[(-\kappa + m - 1)\cos(-m\pi) - m\cos(m-2)(-\pi)]\} \\
=& \frac{r^{m}}{2\mu n\sqrt{2\pi}}\{-K_{I2m}[(\kappa - m - 1)\sin(m\pi) - m\sin(m\pi)] \\
&+K_{II2m}[(-\kappa + m - 1)\cos(m\pi) - m\cos(m\pi)]\} \\
=& \frac{r^{m}}{2\mu n\sqrt{2\pi}}\{K_{I2m}[(-\kappa - 1)\cos(m\pi)]
\end{aligned} \tag{A.15}$$

$$\begin{aligned}
v_{2m}(r,\pi) =& \frac{r^{2m/2}}{2\mu n\sqrt{2\pi}}\{K_{I2m}[(\kappa - \frac{2m}{2} - (-1)^{2m})\sin\frac{2m}{2}(\pi) + \frac{2m}{2}\sin(\frac{2m}{2}-2)(\pi)] \\
&+K_{II2m}[(-\kappa + \frac{2m}{2} - (-1)^{2m})\cos\frac{2m}{2}(\pi) - \frac{2m}{2}\cos(\frac{2m}{2}-2)(\pi)]\} \\
=& \frac{r^{m}}{2\mu n\sqrt{2\pi}}\{K_{I2m}[(\kappa - m - 1)\sin(m\pi) + m\sin(m-2)(\pi)] \\
&+K_{II2m}[(-\kappa + m - 1)\cos(m\pi) - m\cos(m-2)(\pi)]\} \\
=& \frac{r^{m}}{2\mu n\sqrt{2\pi}}\{K_{I2m}[(\kappa - m - 1)\sin(m\pi) + m\sin(m\pi)] \\
&+K_{II2m}[(-\kappa + m - 1)\cos(m\pi) - m\cos(m\pi)]\} \\
=& \frac{r^{m}}{2\mu n\sqrt{2\pi}}\{K_{I2m}[(-\kappa - 1)\cos(m\pi)]
\end{aligned} \tag{A.16}$$

Finally we arrive at

$$v_{2m}(r,\pi) - v_{2m}(r,-\pi) = 0 \tag{A.17}$$

Next we show that the odd terms are preserved. Assume $i = 2m + 1$ where m is an

integer, by substituting $\theta = -\pi$ into Eq (3.5)we will get

$$
\begin{aligned}
&u_{2m+1}(r,-\pi)\\
=&\frac{r^{(2m+1)/2}}{2\mu n\sqrt{2\pi}}\{K_{I2m+1}[(\kappa+\frac{2m+1}{2}+(-1)^{2m+1})\cos\frac{2m+1}{2}(-\pi)-\frac{2m+1}{2}\cos(\frac{2m+1}{2}-2)(-\pi)]\\
+&K_{II2m+1}[(\kappa+\frac{2m+1}{2}-(-1)^{2m+1})\sin\frac{2m+1}{2}(-\pi)-\frac{2m+1}{2}\sin(\frac{2m+1}{2}-2)(-\pi)]\}\\
=&\frac{r^{m+1/2}}{2\mu n\sqrt{2\pi}}\{K_{I2m+1}[-(\kappa+m-1/2)\sin(m\pi)+(m+1/2)\sin(m\pi)]\\
+&K_{II2m+1}[-(\kappa+m+3/2)\cos(m\pi)+(m+1/2)\cos(m\pi)]\}\\
=&\frac{r^{m+1/2}}{2\mu n\sqrt{2\pi}}[K_{II2m+1}[(-\kappa-1)\cos(m\pi)]
\end{aligned}
\tag{A.18}
$$

We then substitute $\theta = \pi$ into Eq (3.5) to arrive at

$$
\begin{aligned}
&u_{2m+1}(r,\pi)\\
=&\frac{r^{(2m+1)/2}}{2\mu n\sqrt{2\pi}}\{K_{I2m+1}[(\kappa+\frac{2m+1}{2}+(-1)^{2m+1})\cos\frac{2m+1}{2}(\pi)-\frac{2m+1}{2}\cos(\frac{2m+1}{2}-2)(\pi)]\\
+&K_{II2m+1}[(\kappa+\frac{2m+1}{2}-(-1)^{2m+1})\sin\frac{2m+1}{2}(\pi)-\frac{2m+1}{2}\sin(\frac{2m+1}{2}-2)(\pi)]\}\\
=&\frac{r^{m+1/2}}{2\mu n\sqrt{2\pi}}\{K_{I2m+1}[(\kappa+m-1/2)\sin(m\pi)-(m+1/2)\sin(m\pi)]\\
+&K_{II2m+1}[(\kappa+m+3/2)\cos(m\pi)-(m+1/2)\cos(m\pi)]\}\\
=&\frac{r^{m+1/2}}{2\mu n\sqrt{2\pi}}[K_{II2m+1}[(\kappa+1)\cos(m\pi)]
\end{aligned}
\tag{A.19}
$$

Finally we arrive at

$$
u_{2m+1}(r,\pi)-u_{2m+1}(r,-\pi)=\frac{r^{m+1/2}}{\mu n\sqrt{2\pi}}[K_{II2m+1}[(\kappa+1)(-1)^m] \tag{A.20}
$$

Next we substitute $\theta = -\pi$ into Eq (3.6)we will get

$$
\begin{aligned}
&v_{2m+1}(r,-\pi)\\
=&\frac{r^{(2m+1)/2}}{2\mu n\sqrt{2\pi}}\{K_{I2m+1}[(\kappa-\frac{2m+1}{2}-(-1)^{2m+1})\sin\frac{2m+1}{2}(-\pi)+\frac{2m+1}{2}\sin(\frac{2m+1}{2}-2)(-\pi)]\\
&+K_{II2m+1}[(-\kappa+\frac{2m+1}{2}-(-1)^{2m+1})\cos\frac{2m+1}{2}(-\pi)-\frac{2m+1}{2}\cos(\frac{2m+1}{2}-2)(-\pi)]\}\\
=&\frac{r^{m+1/2}}{2\mu n\sqrt{2\pi}}\{K_{I2m+1}[-(\kappa-m+1/2)\cos(m\pi)-(m+1/2)\cos(m\pi)]\\
&+K_{II2m+1}[-(-\kappa+m+3/2)\sin(m\pi)+(m+1/2)\sin(m\pi)]\}\\
=&\frac{r^{m+1/2}}{2\mu n\sqrt{2\pi}}[K_{I2m+1}[(-\kappa-1)\cos(m\pi)]
\end{aligned}
\tag{A.21}
$$

$$
\begin{aligned}
&v_{2m+1}(r,\pi)\\
=&\frac{r^{(2m+1)/2}}{2\mu n\sqrt{2\pi}}\{K_{I2m+1}[(\kappa-\frac{2m+1}{2}-(-1)^{2m+1})\sin\frac{2m+1}{2}(\pi)+\frac{2m+1}{2}\sin(\frac{2m+1}{2}-2)(\pi)]\\
&+K_{II2m+1}[(-\kappa+\frac{2m+1}{2}-(-1)^{2m+1})\cos\frac{2m+1}{2}(\pi)-\frac{2m+1}{2}\cos(\frac{2m+1}{2}-2)(\pi)]\}\\
=&\frac{r^{m+1/2}}{2\mu n\sqrt{2\pi}}\{K_{I2m+1}[(\kappa-m+1/2)\cos(m\pi)+(m+1/2)\cos(m\pi)]\\
&+K_{II2m+1}[-(-\kappa+m+3/2)\sin(m\pi)+(m+1/2)\sin(m\pi)]\}\\
=&\frac{r^{m+1/2}}{2\mu n\sqrt{2\pi}}[K_{I2m+1}[(\kappa+1)\cos(m\pi)]
\end{aligned}
\tag{A.22}
$$

Finally we arrive at

$$
v_{2m+1}(r,\pi)-v_{2m+1}(r,-\pi)=\frac{r^{m+1/2}}{\mu n\sqrt{2\pi}}[K_{I2m+1}[(\kappa+1)(-1)^m] \tag{A.23}
$$

It can clearly been from the Eqs. (A.12) to (A.23) that even order terms of r in the expansion of the displacement jump vanish and odd order terms are preserved.

A.4 Derivatives of displacement field and shape function in polar coordinates

The derivatives of the displacement field in Eq. (4.28) with respect to r and θ are

$$\frac{\partial u}{\partial r} = \sum_{I=1}^{4} \frac{\partial N_I}{\partial r} u_I + \sum_{I=1}^{4} \frac{\partial N_I}{\partial r} \sum_{j=1}^{n_F} F_j b_{jI} + \sum_{I=1}^{4} N_I \sum_{j=1}^{n_F} \frac{\partial F_j}{\partial r} b_{jI} \tag{A.24}$$

$$\frac{\partial u}{\partial \theta} = \sum_{I=1}^{4} \frac{\partial N_I}{\partial \theta} u_I + \sum_{I=1}^{4} \frac{\partial N_I}{\partial \theta} \sum_{j=1}^{n_F} F_j b_{jI} + \sum_{I=1}^{4} N_I \sum_{j=1}^{n_F} \frac{\partial F_j}{\partial \theta} b_{jI} \tag{A.25}$$

where the derivatives of the shape functions are

$$\frac{\partial N_I}{\partial r} = \frac{1}{4}(1 + 4\frac{x_I \cos\theta}{h_x^2})(1 + 4\frac{y_I r \sin\theta}{h_y^2}) + \frac{1}{4}(1 + 4\frac{x_I r \cos\theta}{h_x^2})(1 + 4\frac{y_I \sin\theta}{h_y^2}) \tag{A.26}$$

$$\frac{\partial N_I}{\partial \theta} = \frac{1}{4}(1 - 4\frac{x_I r \sin\theta}{h_x^2})(1 + 4\frac{y_I r \sin\theta}{h_y^2}) + \frac{1}{4}(1 + 4\frac{x_I r \cos\theta}{h_x^2})(1 + 4\frac{y_I r \cos\theta}{h_y^2}) \tag{A.27}$$

A.5 Coefficients of Irwin's integral expansion

The coefficients of Irwin's integral expansion in Eq. (4.19) and Eq. (4.20) are

$$\begin{cases}
\alpha_0^r = \frac{1}{4} m_1^r m_4^r \pi \\
\alpha_1^r = \frac{1}{3} m_1^r m_5^r \\
\alpha_2^r = \frac{3}{16} m_2^r m_4^r \pi + \frac{1}{16} m_1^r m_6^r \pi \\
\alpha_3^r = \frac{2}{15} m_1^r m_7^r + \frac{1}{5} m_2^r m_5^r \\
\alpha_4^r = \frac{1}{32} m_1^r m_8^r \pi + \frac{1}{32} m_2^r m_6^r \pi + \frac{5}{32} m_3^r m_4^r \pi \\
\alpha_5^r = \frac{8}{105} m_1^r m_9^r + \frac{2}{35} m_2^r m_7^r + \frac{1}{7} m_3^r m_5^r \\
\alpha_6^r = \frac{3}{256} m_2^r m_8^r \pi + \frac{5}{256} m_3^r m_6^r \pi + \frac{5}{256} m_1^r m_{10}^r \pi \qquad r = I, II \\
\alpha_7^r = \frac{8}{315} m_2^r m_9^r + \frac{2}{63} m_3^r m_7^r + \frac{16}{315} m_1^r m_{11}^r \\
\alpha_8^r = \frac{3}{512} m_2^r m_{10}^r \pi + \frac{3}{512} m_3^r m_8^r \pi \\
\alpha_9^r = \frac{8}{693} m_3^r m_9^r + \frac{16}{1155} m_2^r m_{11}^r \\
\alpha_{10}^r = \frac{5}{2048} m_3^r m_{10}^r \pi \\
\alpha_{11}^r = \frac{16}{3003} m_3^r m_{11}^r
\end{cases} \tag{A.28}$$

The coefficients of m are

$$
\begin{cases}
m_1^I = \sum_{I=1}^4 \frac{1}{2} b_{y1I} \\
m_2^I = \sum_{I=1}^4 (\frac{b_{y8I}}{2} - \frac{2b_{y1I}x_I}{h_x^2}) \\
m_3^I = \sum_{I=1}^4 (-\frac{2x_I b_{y8I}}{h_x^2}) \\
m_4^I = \nu \sum_{I=1}^4 \frac{b_{x2I}}{8} + (1-\nu) \sum_{I=1}^4 (\frac{b_{y1I}}{8} + \frac{b_{y4I}}{4}) \\
m_5^I = \nu \sum_{I=1}^4 (\frac{x_I u_{xI}}{h_x^2} + \frac{b_{x5I}}{4}) + (1-\nu) \sum_{I=1}^4 (\frac{y_I u_{yI}}{h_y^2} + \frac{b_{y6I}}{4}) \\
m_6^I = \nu \sum_{I=1}^4 (\frac{3}{2} \frac{x_I b_{x2I}}{h_x^2} + \frac{3}{8} b_{x7I}) \\
+(1-\nu) \sum_{I=1}^4 (\frac{y_I b_{y2I}}{h_y^2} + \frac{x_I b_{y1I}}{2h_x^2} + \frac{x_I b_{y4I}}{h_x^2} + \frac{b_{y8I}}{8} + \frac{b_{y10I}}{4}) \\
m_7^I = \nu \sum_{I=1}^4 (\frac{2x_I b_{x5I}}{h_x^2} + \frac{b_{x11I}}{2} + \frac{b_{x13I}}{2}) \\
+(1-\nu) \sum_{I=1}^4 (\frac{4x_I y_I u_{yI}}{h_x^2 h_y^2} + \frac{y_I b_{y5I}}{h_y^2} + \frac{x_I b_{y6I}}{h_x^2} + \frac{b_{y12I}}{2}) \\
m_8^I = \nu \sum_{I=1}^4 \frac{5}{2} \frac{x_I b_{x7I}}{h_x^2} \\
+(1-\nu) \sum_{I=1}^4 (\frac{4x_I y_I b_{y2I}}{h_x^2 h_y^2} + \frac{y_I b_{y7I}}{h_y^2} + \frac{1}{2} \frac{x_I b_{y8I}}{h_x^2} + \frac{x_I b_{y10I}}{h_x^2}) \\
m_9^I = \nu \sum_{I=1}^4 (\frac{3x_I b_{x11I}}{h_x^2} + \frac{3x_I b_{x13I}}{h_x^2}) \\
+(1-\nu) \sum_{I=1}^4 (\frac{4x_I y_I b_{y5I}}{h_x^2 h_y^2} + \frac{y_I b_{y11I}}{h_y^2} + \frac{y_I b_{y13I}}{h_y^2} + \frac{2x_I b_{y12I}}{h_x^2}) \\
m_{10}^I = (1-\nu) \sum_{I=1}^4 \frac{4x_I y_I b_{y7I}}{h_x^2 h_y^2} \\
m_{11}^I = (1-\nu) \sum_{I=1}^4 (\frac{4x_I y_I b_{y11I}}{h_x^2 h_y^2} + \frac{4x_I y_I b_{y13I}}{h_x^2 h_y^2})
\end{cases}
\tag{A.29}
$$

$$
\begin{cases}
m_1^{II} = \sum_{I=1}^{4} \frac{1}{2} b_{x1I} \\
m_2^{II} = \sum_{I=1}^{4} (\frac{b_{x8I}}{2} - \frac{2 b_{x1I} x_I}{h_x^2}) \\
m_3^{II} = \sum_{I=1}^{4} (-\frac{2 x_I b_{x8I}}{h_x^2}) \\
m_4^{II} = \sum_{I=1}^{4} (\frac{b_{x1I}}{8} + \frac{b_{x4I}}{4} + \frac{b_{y2I}}{8}) \\
m_5^{II} = \sum_{I=1}^{4} (\frac{y_I u_{xI}}{h_y^2} + \frac{x_I u_{yI}}{h_x^2} + \frac{b_{x6I}}{4} + \frac{b_{y5I}}{4}) \\
m_6^{II} = \sum_{I=1}^{4} (\frac{y_I b_{x2I}}{h_y^2} + \frac{x_I b_{x1I}}{2h_x^2} + \frac{x_I b_{x4I}}{h_x^2} + \frac{3 x_I b_{y2I}}{2h_x^2} + \frac{b_{x8I}}{8} + \frac{b_{x10I}}{4} + \frac{3 b_{y7I}}{8}) \\
m_7^{II} = \sum_{I=1}^{4} (\frac{4 x_I y_I u_{xI}}{h_x^2 h_y^2} + \frac{y_I b_{x5I}}{h_y^2} + \frac{x_I b_{x6I}}{h_x^2} + \frac{2 x_I b_{y5I}}{h_x^2} + \frac{b_{y11I}}{2} + \frac{b_{y13I}}{2} + \frac{b_{x12I}}{2}) \\
m_8^{II} = \sum_{I=1}^{4} (\frac{4 x_I y_I b_{x2I}}{h_x^2 h_y^2} + \frac{y_I b_{x7I}}{h_y^2} + \frac{x_I b_{x8I}}{2h_x^2} + \frac{x_I b_{x10I}}{h_x^2} + \frac{5 x_I b_{y7I}}{2h_x^2}) \\
m_9^{II} = \sum_{I=1}^{4} (\frac{4 x_I y_I b_{x5I}}{h_x^2 h_y^2} + \frac{y_I b_{x11I}}{h_y^2} + \frac{y_I b_{x13I}}{h_y^2} + \frac{2 x_I b_{x12I}}{h_x^2} + \frac{3 x_I b_{y11I}}{h_x^2} + \frac{3 x_I b_{y13I}}{h_x^2}) \\
m_{10}^{II} = \sum_{I=1}^{4} \frac{4 x_I y_I b_{x7I}}{h_x^2 h_y^2} \\
m_{11}^{II} = \sum_{I=1}^{4} (\frac{4 x_I y_I b_{x11I}}{h_x^2 h_y^2} + \frac{4 x_I y_I b_{x13I}}{h_x^2 h_y^2})
\end{cases}
\tag{A.30}
$$

A.6 Coefficients of Irwin's integral expansion

The coefficients of Irwin's integral expansion in Eq. (7.5) and Eq. (7.6) are

$$
\begin{cases}
\alpha_0^r = \frac{1}{4} m_1^r m_5^r \pi \\
\alpha_1^r = \frac{1}{3} m_1^r m_6^r \\
\alpha_2^r = \frac{3}{16} m_2^r m_5^r \pi + \frac{1}{16} m_1^r m_7^r \pi \\
\alpha_3^r = \frac{2}{15} m_1^r m_8^r + \frac{1}{5} m_2^r m_6^r \\
\alpha_4^r = \frac{1}{32} m_1^r m_9^r \pi + \frac{1}{32} m_2^r m_7^r \pi + \frac{5}{32} m_3^r m_5^r \pi \\
\alpha_5^r = \frac{8}{105} m_1^r m_{10}^r + \frac{2}{35} m_2^r m_8^r + \frac{1}{7} m_3^r m_6^r \\
\alpha_6^r = \frac{3}{256} m_2^r m_9^r \pi + \frac{5}{256} m_3^r m_7^r \pi + \frac{5}{256} m_1^r m_{11}^r \pi + \frac{35}{256} m_4^r m_5^r \pi \qquad r = I, II \\
\alpha_7^r = \frac{8}{315} m_2^r m_{10}^r + \frac{2}{63} m_3^r m_8^r + \frac{16}{315} m_1^r m_{12}^r + \frac{1}{9} m_4^r m_6^r \\
\alpha_8^r = \frac{3}{512} m_2^r m_{11}^r \pi + \frac{3}{512} m_3^r m_9^r \pi + \frac{7}{512} m_4^r m_7^r \pi \\
\alpha_9^r = \frac{8}{693} m_3^r m_{10}^r + \frac{16}{1155} m_2^r m_{12}^r + \frac{2}{99} m_4^r m_8^r \\
\alpha_{10}^r = \frac{5}{2048} m_3^r m_{11}^r \pi + \frac{7}{2048} m_4^r m_9^r \pi \\
\alpha_{11}^r = \frac{16}{3003} m_3^r m_{12}^r + \frac{8}{1287} m_4^r m_{10}^r \\
\alpha_{12}^r = \frac{5}{4096} m_4^r m_{11}^r \pi \\
\alpha_{13}^r = \frac{16}{6435} m_4^r m_{12}^r
\end{cases}
\tag{A.31}
$$

The coefficients of m are

$$
\begin{cases}
m_1^I &= \sum_{I=1}^{4} \frac{1}{2} \frac{\left({h_x}^2+4\,x_I x_{o'}\right)\left({h_y}^2+4\,y_I y_{o'}\right)\left(-b_{x1I}\sin(\alpha)+b_{y1I}\cos(\alpha)\right)}{{h_x}^2{h_y}^2} \\
m_2^I &= \sum_{I=1}^{4} \frac{-1}{2{h_x}^2{h_y}^2}(\sin(\alpha)\,b_{x8I}{h_x}^2{h_y}^2 + 4\,\sin(\alpha)\,b_{x8I}{h_x}^2 y_I y_{o'} + 4\,\sin(\alpha)\,b_{x8I}x_I x_{o'}{h_y}^2 \\
&\quad +16\,\sin(\alpha)\,b_{x8I}x_I x_{o'}y_I y_{o'} - 4\,b_{x1I}y_I\,(\sin(\alpha))^2\,{h_x}^2 - 16\,b_{x1I}y_I\,(\sin(\alpha))^2\,x_I x_{o'} \\
&\quad -4\,b_{x1I}\sin(\alpha)\,x_I\cos(\alpha)\,{h_y}^2 - 16\,b_{x1I}\sin(\alpha)\,x_I\cos(\alpha)\,y_I y_{o'} - \cos(\alpha)\,b_{y8I}{h_x}^2{h_y}^2 \\
&\quad -4\,\cos(\alpha)\,b_{y8I}{h_x}^2 y_I y_{o'} - 4\,\cos(\alpha)\,b_{y8I}x_I x_{o'}{h_y}^2 - 16\,\cos(\alpha)\,b_{y8I}x_I x_{o'}y_I y_{o'} \\
&\quad +4\,b_{y1I}\cos(\alpha)\,y_I\sin(\alpha)\,{h_x}^2 + 16\,b_{y1I}\cos(\alpha)\,y_I\sin(\alpha)\,x_I x_{o'} + 4\,b_{y1I}x_I\,(\cos(\alpha))^2\,{h_y}^2 \\
&\quad +16\,b_{y1I}x_I\,(\cos(\alpha))^2\,y_I y_{o'}) \\
m_3^I &= \sum_{I=1}^{4} \frac{2}{{h_x}^2{h_y}^2}(b_{x8I}y_I\,(\sin(\alpha))^2\,{h_x}^2 + 4\,b_{x8I}y_I\,(\sin(\alpha))^2\,x_I x_{o'} + \sin(\alpha)\,b_{x8I}x_I\cos(\alpha)\,{h_y}^2 \\
&\quad +4\,\sin(\alpha)\,b_{x8I}x_I\cos(\alpha)\,y_I y_{o'} - 4\,x_I\cos(\alpha)\,y_I\,(\sin(\alpha))^2\,b_{x1I} - \cos(\alpha)\,b_{y8I}y_I\sin(\alpha)\,{h_x}^2 \\
&\quad -4\,\cos(\alpha)\,b_{y8I}y_I\sin(\alpha)\,x_I x_{o'} - b_{y8I}x_I\,(\cos(\alpha))^2\,{h_y}^2 - 4\,b_{y8I}x_I\,(\cos(\alpha))^2\,y_I y_{o'} \\
&\quad +4\,x_I\,(\cos(\alpha))^2\,y_I\sin(\alpha)\,b_{y1I}) \\
m_4^I &= \sum_{I=1}^{4} \frac{8x_I\cos(\alpha)y_I\sin(\alpha)\left(-\sin(\alpha)b_{x8I}+\cos(\alpha)b_{y8I}\right)}{{h_x}^2{h_y}^2} \\
m_5^I &= \nu\sum_{I=1}^{4}\left(\frac{\left({h_x}^2+4\,x_I x_{o'}\right)\left({h_y}^2+4\,y_I y_{o'}\right)\left(b_{x2I}\cos(\alpha)+b_{y2I}\sin(\alpha)\right)}{8{h_x}^2{h_y}^2}\right) \\
&\quad -(1-\nu)\sum_{I=1}^{4}\frac{1}{8}\left(\frac{\left({h_x}^2+4\,x_I x_{o'}\right)\left({h_y}^2+4\,y_I y_{o'}\right)\left(b_{x1I}\sin(\alpha)+2\,\sin(\alpha)b_{x4I}-b_{y1I}\cos(\alpha)-2\,\cos(\alpha)b_{y4I}\right)}{{h_x}^2{h_y}^2}\right)
\end{cases}
$$

$$
\left\{
\begin{array}{ll}
m_6^I & = \nu \sum_{I=1}^{4} \frac{1}{4{h_x}^2{h_y}^2}(\, 4 \, \cos(\alpha) \, u_{xI} y_I \sin(\alpha) \, {h_x}^2 + 16 \, \cos(\alpha) \, u_{xI} y_I \sin(\alpha) \, x_I x_{o'} \\
& +4 \, u_{xI} x_I \left(\cos(\alpha)\right)^2 {h_y}^2 + 16 \, u_{xI} x_I \left(\cos(\alpha)\right)^2 y_I y_{o'} + \cos(\alpha) \, b_{x5I} {h_x}^2 {h_y}^2 \\
& +4 \, \cos(\alpha) \, b_{x5I} {h_x}^2 y_I y_{o'} + 4 \, \cos(\alpha) \, b_{x5I} x_I x_{o'} {h_y}^2 + 16 \, \cos(\alpha) \, b_{x5I} x_I x_{o'} y_I y_{o'} \\
& +4 \, u_{yI} y_I \left(\sin(\alpha)\right)^2 {h_x}^2 + 16 \, u_{yI} y_I \left(\sin(\alpha)\right)^2 x_I x_{o'} + 4 \, \sin(\alpha) \, u_{yI} x_I \cos(\alpha) \, {h_y}^2 \\
& +16 \, \sin(\alpha) \, u_{yI} x_I \cos(\alpha) \, y_I y_{o'} + \sin(\alpha) \, b_{y5I} {h_x}^2 {h_y}^2 + 4 \, \sin(\alpha) \, b_{y5I} {h_x}^2 y_I y_{o'} \\
& +4 \, \sin(\alpha) \, b_{y5I} x_I x_{o'} {h_y}^2 + 16 \, \sin(\alpha) \, b_{y5I} x_I x_{o'} y_I y_{o'}) \\
& +(1-\nu) \sum_{I=1}^{4} \frac{1}{4{h_x}^2{h_y}^2}(\, 4 \, u_{xI} x_I \left(\sin(\alpha)\right)^2 {h_y}^2 + 16 \, u_{xI} x_I \left(\sin(\alpha)\right)^2 y_I y_{o'} \\
& -4 \, \cos(\alpha) \, u_{xI} y_I \sin(\alpha) \, {h_x}^2 - 16 \, \cos(\alpha) \, u_{xI} y_I \sin(\alpha) \, x_I x_{o'} - \sin(\alpha) \, b_{x6I} {h_x}^2 {h_y}^2 \\
& -4 \, \sin(\alpha) \, b_{x6I} {h_x}^2 y_I y_{o'} - 4 \, \sin(\alpha) \, b_{x6I} x_I x_{o'} {h_y}^2 - 16 \, \sin(\alpha) \, b_{x6I} x_I x_{o'} y_I y_{o'} \\
& -4 \, \sin(\alpha) \, u_{yI} x_I \cos(\alpha) \, {h_y}^2 - 16 \, \sin(\alpha) \, u_{yI} x_I \cos(\alpha) \, y_I y_{o'} + 4 \, u_{yI} y_I \left(\cos(\alpha)\right)^2 {h_x}^2 \\
& +16 \, u_{yI} y_I \left(\cos(\alpha)\right)^2 x_I x_{o'} + \cos(\alpha) \, b_{y6I} {h_x}^2 {h_y}^2 + 4 \, \cos(\alpha) \, b_{y6I} {h_x}^2 y_I y_{o'} \\
& +4 \, \cos(\alpha) \, b_{y6I} x_I x_{o'} {h_y}^2 + 16 \, \cos(\alpha) \, b_{y6I} x_I x_{o'} y_I y_{o'})
\end{array}
\right.
\tag{A.32}
$$

$$
\left\{
\begin{aligned}
m_7^I \quad &= \nu \sum_{I=1}^{4} \tfrac{3}{8{h_x}^2{h_y}^2}(4\,\cos(\alpha)\, b_{x2I} y_I \sin(\alpha)\, {h_x}^2 + 16\,\cos(\alpha)\, b_{x2I} y_I \sin(\alpha)\, x_I x_{o'} \\
&+4\, b_{x2I} x_I \left(\cos(\alpha)\right)^2 {h_y}^2 + 16\, b_{x2I} x_I \left(\cos(\alpha)\right)^2 y_I y_{o'} + \cos(\alpha)\, b_{x\gamma I} {h_x}^2 {h_y}^2 \\
&+4\,\cos(\alpha)\, b_{x\gamma I} {h_x}^2 y_I y_{o'} + 4\,\cos(\alpha)\, b_{x\gamma I} x_I x_{o'} {h_y}^2 + 16\,\cos(\alpha)\, b_{x\gamma I} x_I x_{o'} y_I y_{o'} \\
&+4\, b_{y2I} y_I \left(\sin(\alpha)\right)^2 {h_x}^2 + 16\, b_{y2I} y_I \left(\sin(\alpha)\right)^2 x_I x_{o'} + 4\,\sin(\alpha)\, b_{y2I} x_I \cos(\alpha)\, {h_y}^2 \\
&+16\,\sin(\alpha)\, b_{y2I} x_I \cos(\alpha)\, y_I y_{o'} + \sin(\alpha)\, b_{y\gamma I} {h_x}^2 {h_y}^2 + 4\,\sin(\alpha)\, b_{y\gamma I} {h_x}^2 y_I y_{o'} \\
&+4\,\sin(\alpha)\, b_{y\gamma I} x_I x_{o'} {h_y}^2 + 16\,\sin(\alpha)\, b_{y\gamma I} x_I x_{o'} y_I y_{o'}) \\
&+(1-\nu) \sum_{I=1}^{4} -\tfrac{1}{8{h_x}^2{h_y}^2}(-4\, b_{y1I} x_I \left(\cos(\alpha)\right)^2 {h_y}^2 + 4\, b_{x1I} y_I \left(\sin(\alpha)\right)^2 {h_x}^2 \\
&-\cos(\alpha)\, b_{y8I} {h_x}^2 {h_y}^2 - 8\, x_I \left(\cos(\alpha)\right)^2 {h_y}^2 b_{y4I} - 2\,\cos(\alpha)\, {h_x}^2 {h_y}^2 b_{y10I} \\
&-8\, b_{x2I} x_I \left(\sin(\alpha)\right)^2 {h_y}^2 + 2\,\sin(\alpha)\, {h_x}^2 {h_y}^2 b_{x10I} - 8\, b_{y2I} y_I \left(\cos(\alpha)\right)^2 {h_x}^2 \\
&+8\, y_I \left(\sin(\alpha)\right)^2 {h_x}^2 b_{x4I} + 16\, b_{x1I} \sin(\alpha)\, x_I \cos(\alpha)\, y_I y_{o'} - 16\,\cos(\alpha)\, b_{y8I} x_I x_{o'} y_I y_{o'} \\
&-16\, b_{y1I} \cos(\alpha)\, y_I \sin(\alpha)\, x_I x_{o'} + 32\,\cos(\alpha)\, b_{x2I} y_I \sin(\alpha)\, x_I x_{o'} + 32\,\sin(\alpha)\, b_{y2I} x_I \cos(\alpha)\, y_I y_{o'} \\
&+32\,\sin(\alpha)\, x_I x_{o'} y_I y_{o'} b_{x10I} - 32\,\cos(\alpha)\, y_I \sin(\alpha)\, x_I x_{o'} b_{y4I} - 32\,\cos(\alpha)\, x_I x_{o'} y_I y_{o'} b_{y10I} \\
&+32\,\cos(\alpha)\, y_I \sin(\alpha)\, x_I y_{o'} b_{x4I} + 16\,\sin(\alpha)\, b_{x8I} x_I x_{o'} y_I y_{o'} + \sin(\alpha)\, b_{x8I} {h_x}^2 {h_y}^2 \\
&+4\,\sin(\alpha)\, b_{x8I} {h_x}^2 y_I y_{o'} + 4\,\sin(\alpha)\, b_{x8I} x_I x_{o'} {h_y}^2 + 16\, b_{x1I} y_I \left(\sin(\alpha)\right)^2 x_I x_{o'} \\
&+4\, b_{x1I} \sin(\alpha)\, x_I \cos(\alpha)\, {h_y}^2 - 4\,\cos(\alpha)\, b_{y8I} {h_x}^2 y_I y_{o'} - 4\,\cos(\alpha)\, b_{y8I} x_I x_{o'} {h_y}^2 \\
&-4\, b_{y1I} \cos(\alpha)\, y_I \sin(\alpha)\, {h_x}^2 - 16\, b_{y1I} x_I \left(\cos(\alpha)\right)^2 y_I y_{o'} + 8\,\sin(\alpha)\, {h_x}^2 y_I y_{o'} b_{x10I} \\
&-8\,\cos(\alpha)\, y_I \sin(\alpha)\, {h_x}^2 b_{y4I} - 32\, x_I \left(\cos(\alpha)\right)^2 y_I y_{o'} b_{y4I} - 8\,\cos(\alpha)\, x_I x_{o'} {h_y}^2 b_{y10I} \\
&-32\, b_{x2I} x_I \left(\sin(\alpha)\right)^2 y_I y_{o'} + 8\,\cos(\alpha)\, b_{x2I} y_I \sin(\alpha)\, {h_x}^2 + 8\,\sin(\alpha)\, b_{y2I} x_I \cos(\alpha)\, {h_y}^2 \\
&-8\,\cos(\alpha)\, {h_x}^2 y_I y_{o'} b_{y10I} - 32\, b_{y2I} y_I \left(\cos(\alpha)\right)^2 x_I x_{o'} + 8\,\sin(\alpha)\, x_I x_{o'} {h_y}^2 b_{x10I} \\
&+32\, y_I \left(\sin(\alpha)\right)^2 x_I x_{o'} b_{x4I} + 8\,\sin(\alpha)\, x_I \cos(\alpha)\, {h_y}^2 b_{x4I})
\end{aligned}
\right.
\tag{A.33}
$$

$$
\begin{cases}
m_8^I & = \nu \sum_{I=1}^{4} \frac{1}{2{h_x}^2{h_y}^2} (16 \cos(\alpha) b_{x5I} y_I \sin(\alpha) x_I x_{o'} + 16 \cos(\alpha) x_I x_{o'} y_I y_{o'} b_{x11I} \\
& +16 \cos(\alpha) x_I x_{o'} y_I y_{o'} b_{x13I} + 16 \sin(\alpha) b_{y5I} x_I \cos(\alpha) y_I y_{o'} + 16 \sin(\alpha) x_I x_{o'} y_I y_{o'} b_{y11I} \\
& +16 \sin(\alpha) x_I x_{o'} y_I y_{o'} b_{y13I} + 4 \sin(\alpha) {h_x}^2 y_I y_{o'} b_{y11I} + 4 \sin(\alpha) {h_x}^2 y_I y_{o'} b_{y13I} \\
& +4 \cos(\alpha) b_{x5I} y_I \sin(\alpha) {h_x}^2 + 16 b_{x5I} x_I (\cos(\alpha))^2 y_I y_{o'} + 4 \sin(\alpha) x_I x_{o'} {h_y}^2 b_{y11I} \\
& +4 \sin(\alpha) x_I x_{o'} {h_y}^2 b_{y13I} + 4 \cos(\alpha) x_I x_{o'} {h_y}^2 b_{x13I} + 16 b_{y5I} y_I (\sin(\alpha))^2 x_I x_{o'} \\
& +4 \sin(\alpha) b_{y5I} x_I \cos(\alpha) {h_y}^2 + 16 x_I \cos(\alpha) y_I (\sin(\alpha))^2 u_{yI} + 16 x_I (\cos(\alpha))^2 y_I \sin(\alpha) u_{xI} \\
& +4 \cos(\alpha) {h_x}^2 y_I y_{o'} b_{x11I} + 4 \cos(\alpha) {h_x}^2 y_I y_{o'} b_{x13I} + 4 \cos(\alpha) x_I x_{o'} {h_y}^2 b_{x11I} + \cos(\alpha) {h_x}^2 {h_y}^2 b_{x11I} \\
& + \cos(\alpha) {h_x}^2 {h_y}^2 b_{x13I} + \sin(\alpha) {h_x}^2 {h_y}^2 b_{y11I} + \sin(\alpha) {h_x}^2 {h_y}^2 b_{y13I} \\
& +4 b_{x5I} x_I (\cos(\alpha))^2 {h_y}^2 + 4 b_{y5I} y_I (\sin(\alpha))^2 {h_x}^2) \\
& +(1-\nu) \sum_{I=1}^{4} \frac{1}{2{h_x}^2{h_y}^2} (16 \cos(\alpha) b_{y12I} x_I x_{o'} y_I y_{o'} - 8 \cos(\alpha) b_{x5I} y_I \sin(\alpha) x_I x_{o'} \\
& -8 \sin(\alpha) b_{y5I} x_I \cos(\alpha) y_I y_{o'} + 2 b_{x5I} x_I (\sin(\alpha))^2 {h_y}^2 \\
& +8 x_I y_I u_{xI} (\sin(\alpha))^3 + 2 b_{y6I} x_I (\cos(\alpha))^2 {h_y}^2 + \cos(\alpha) b_{y12I} {h_x}^2 {h_y}^2 \\
& +8 x_I y_I u_{yI} (\cos(\alpha))^3 + 2 b_{y5I} y_I (\cos(\alpha))^2 {h_x}^2 - 2 b_{x6I} y_I (\sin(\alpha))^2 {h_x}^2 \\
& - \sin(\alpha) b_{x12I} {h_x}^2 {h_y}^2 + 8 \cos(\alpha) b_{y6I} y_I \sin(\alpha) x_I x_{o'} - 16 \sin(\alpha) b_{x12I} x_I x_{o'} y_I y_{o'} \\
& -8 \sin(\alpha) b_{x6I} x_I \cos(\alpha) y_I y_{o'} + 8 b_{x5I} x_I (\sin(\alpha))^2 y_I y_{o'} - 4 \sin(\alpha) b_{x12I} x_I x_{o'} {h_y}^2 \\
& -4 \sin(\alpha) b_{x12I} {h_x}^2 y_I y_{o'} + 8 b_{y5I} y_I (\cos(\alpha))^2 x_I x_{o'} - 2 \sin(\alpha) b_{x6I} x_I \cos(\alpha) {h_y}^2 \\
& -8 b_{x6I} y_I (\sin(\alpha))^2 x_I x_{o'} + 8 b_{y6I} x_I (\cos(\alpha))^2 y_I y_{o'} + 2 \cos(\alpha) b_{y6I} y_I \sin(\alpha) {h_x}^2 \\
& +4 \cos(\alpha) b_{y12I} x_I x_{o'} {h_y}^2 + 4 \cos(\alpha) b_{y12I} {h_x}^2 y_I y_{o'} - 2 \cos(\alpha) b_{x5I} y_I \sin(\alpha) {h_x}^2 \\
& -8 x_I (\cos(\alpha))^2 y_I \sin(\alpha) u_{xI} - 2 \sin(\alpha) b_{y5I} x_I \cos(\alpha) {h_y}^2 - 8 \cos(\alpha) x_I y_I (\sin(\alpha))^2 u_{yI})
\end{cases}
\tag{A.34}
$$

$$
\left\{
\begin{array}{ll}
m_9^I & = \nu \sum_{I=1}^{4} \frac{5}{2{h_x}^2{h_y}^2} (\cos(\alpha)\, b_{x\gamma I} y_I \sin(\alpha)\, {h_x}^2 + 4\, \cos(\alpha)\, b_{x\gamma I} y_I \sin(\alpha)\, x_I x_{o'} \\
& + b_{x\gamma I} x_I (\cos(\alpha))^2 {h_y}^2 + 4\, b_{x\gamma I} x_I (\cos(\alpha))^2 y_I y_{o'} + 4\, x_I (\cos(\alpha))^2 y_I \sin(\alpha)\, b_{x2I} \\
& + b_{y\gamma I} y_I (\sin(\alpha))^2 {h_x}^2 + 4\, b_{y\gamma I} y_I (\sin(\alpha))^2 x_I x_{o'} + \sin(\alpha)\, b_{y\gamma I} x_I \cos(\alpha)\, {h_y}^2 \\
& + 4\, \sin(\alpha)\, b_{y\gamma I} x_I \cos(\alpha)\, y_I y_{o'} + 4\, x_I \cos(\alpha)\, y_I (\sin(\alpha))^2 b_{y2I}) \\
& + (1-\nu) \sum_{I=1}^{4} \frac{1}{2{h_x}^2{h_y}^2} (-8\, \sin(\alpha)\, x_I \cos(\alpha)\, y_I y_{o'} b_{x10I} + 8\, \sin(\alpha)\, x_I \cos(\alpha)\, y_I x_{o'} b_{y10I} \\
& - 4\, b_{x8I} y_I (\sin(\alpha))^2 x_I x_{o'} - \sin(\alpha)\, b_{x8I} x_I \cos(\alpha)\, {h_y}^2 - 4\, \cos(\alpha)\, x_I y_I (\sin(\alpha))^2 b_{x1I} \\
& + \cos(\alpha)\, b_{y8I} y_I \sin(\alpha)\, {h_x}^2 + 4\, b_{y8I} x_I (\cos(\alpha))^2 y_I y_{o'} + 4\, x_I (\cos(\alpha))^2 y_I \sin(\alpha)\, b_{y1I} \\
& - 2\, \cos(\alpha)\, b_{x\gamma I} y_I \sin(\alpha)\, {h_x}^2 - 8\, x_I (\cos(\alpha))^2 y_I \sin(\alpha)\, b_{x2I} - 2\, \sin(\alpha)\, b_{y\gamma I} x_I \cos(\alpha)\, {h_y}^2 \\
& - 8\, \cos(\alpha)\, x_I y_I (\sin(\alpha))^2 b_{y2I} + 8\, b_{x\gamma I} x_I (\sin(\alpha))^2 y_I y_{o'} - 8\, y_I (\sin(\alpha))^2 x_I x_{o'} b_{x10I} \\
& - 2\, \sin(\alpha)\, x_I \cos(\alpha)\, {h_y}^2 b_{x10I} - 8\, \cos(\alpha)\, x_I y_I (\sin(\alpha))^2 b_{x4I} + 8\, b_{y\gamma I} y_I (\cos(\alpha))^2 x_I x_{o'} \\
& + 2\, \cos(\alpha)\, y_I \sin(\alpha)\, {h_x}^2 b_{y10I} + 8\, x_I (\cos(\alpha))^2 y_I y_{o'} b_{y10I} + 8\, x_I (\cos(\alpha))^2 y_I \sin(\alpha)\, b_{y4I} \\
& - 8\, \sin(\alpha)\, b_{y\gamma I} x_I \cos(\alpha)\, y_I y_{o'} - 8\, \cos(\alpha)\, b_{x\gamma I} y_I \sin(\alpha)\, x_I x_{o'} + 4\, \cos(\alpha)\, b_{y8I} y_I \sin(\alpha)\, x_I x_{o'} \\
& - 4\, \sin(\alpha)\, b_{x8I} x_I \cos(\alpha)\, y_I y_{o'} - b_{x8I} y_I (\sin(\alpha))^2 {h_x}^2 + b_{y8I} x_I (\cos(\alpha))^2 {h_y}^2 \\
& + 2\, b_{x\gamma I} x_I (\sin(\alpha))^2 {h_y}^2 + 8\, x_I y_I b_{x2I} (\sin(\alpha))^3 - 2\, y_I (\sin(\alpha))^2 {h_x}^2 b_{x10I} \\
& + 2\, b_{y\gamma I} y_I (\cos(\alpha))^2 {h_x}^2 + 8\, x_I y_I b_{y2I} (\cos(\alpha))^3 + 2\, x_I (\cos(\alpha))^2 {h_y}^2 b_{y10I})
\end{array}
\right.
\tag{A.35}
$$

$$
\begin{cases}
m_{10}^{I} & = \nu \sum_{I=1}^{4} \frac{3}{{h_x}^2 {h_y}^2} (\cos(\alpha)\, y_I \sin(\alpha)\, {h_x}^2 b_{x11I} \\
& + \cos(\alpha)\, y_I \sin(\alpha)\, {h_x}^2 b_{x13I} + 4\, \cos(\alpha)\, y_I \sin(\alpha)\, x_I x_{o'} b_{x11I} + 4\, \cos(\alpha)\, y_I \sin(\alpha)\, x_I x_{o'} b_{x13I} \\
& + x_I (\cos(\alpha))^2 {h_y}^2 b_{x11I} + x_I (\cos(\alpha))^2 {h_y}^2 b_{x13I} + 4\, x_I (\cos(\alpha))^2 y_I y_{o'} b_{x11I} \\
& + 4\, x_I (\cos(\alpha))^2 y_I y_{o'} b_{x13I} + 4\, x_I (\cos(\alpha))^2 y_I \sin(\alpha)\, b_{x5I} + y_I (\sin(\alpha))^2 {h_x}^2 b_{y11I} \\
& + y_I (\sin(\alpha))^2 {h_x}^2 b_{y13I} + 4\, y_I (\sin(\alpha))^2 x_I x_{o'} b_{y11I} + 4\, y_I (\sin(\alpha))^2 x_I x_{o'} b_{y13I} \\
& + \sin(\alpha)\, x_I \cos(\alpha)\, {h_y}^2 b_{y11I} + \sin(\alpha)\, x_I \cos(\alpha)\, {h_y}^2 b_{y13I} + 4\, \sin(\alpha)\, x_I \cos(\alpha)\, y_I y_{o'} b_{y11I} \\
& + 4\, \sin(\alpha)\, x_I \cos(\alpha)\, y_I y_{o'} b_{y13I} + 4\, x_I \cos(\alpha)\, y_I (\sin(\alpha))^2 b_{y5I}) \\
& + (1-\nu) \sum_{I=1}^{4} \frac{1}{{h_x}^2 {h_y}^2} (- \cos(\alpha)\, y_I \sin(\alpha)\, {h_x}^2 b_{x11I} - \cos(\alpha)\, y_I \sin(\alpha)\, {h_x}^2 b_{x13I} \\
& - 4\, x_I (\cos(\alpha))^2 y_I \sin(\alpha)\, b_{x5I} - \sin(\alpha)\, x_I \cos(\alpha)\, {h_y}^2 b_{y11I} \\
& - \sin(\alpha)\, x_I \cos(\alpha)\, {h_y}^2 b_{y13I} - 4\, x_I \cos(\alpha)\, y_I (\sin(\alpha))^2 b_{y5I} \\
& + 4\, x_I (\sin(\alpha))^2 y_I y_{o'} b_{x11I} + 4\, x_I (\sin(\alpha))^2 y_I y_{o'} b_{x13I} - 8\, b_{x12I} y_I (\sin(\alpha))^2 x_I x_{o'} \\
& - 2\, \sin(\alpha)\, b_{x12I} x_I \cos(\alpha)\, {h_y}^2 - 4\, x_I \cos(\alpha)\, y_I (\sin(\alpha))^2 b_{x6I} \\
& + 4\, x_I (\cos(\alpha))^2 y_I x_{o'} b_{y11I} + 4\, x_I (\cos(\alpha))^2 y_I x_{o'} b_{y13I} \\
& + 2\, \cos(\alpha)\, b_{y12I} y_I \sin(\alpha)\, {h_x}^2 + 8\, b_{y12I} x_I (\cos(\alpha))^2 y_I y_{o'} \\
& + 4\, x_I (\cos(\alpha))^2 y_I \sin(\alpha)\, b_{y6I} - 8\, \sin(\alpha)\, b_{x12I} x_I \cos(\alpha)\, y_I y_{o'} \\
& + 8\, \cos(\alpha)\, b_{y12I} y_I \sin(\alpha)\, x_I x_{o'} - 4\, \cos(\alpha)\, y_I \sin(\alpha)\, x_I x_{o'} b_{x11I} \\
& + x_I (\sin(\alpha))^2 {h_y}^2 b_{x11I} + x_I (\sin(\alpha))^2 {h_y}^2 b_{x13I} + 4\, x_I y_I b_{x5I} (\sin(\alpha))^3 \\
& - 2\, b_{x12I} y_I (\sin(\alpha))^2 {h_x}^2 + y_I (\cos(\alpha))^2 {h_x}^2 b_{y11I} + y_I (\cos(\alpha))^2 {h_x}^2 b_{y13I} \\
& + 4\, x_I y_I b_{y5I} (\cos(\alpha))^3 + 2\, b_{y12I} x_I (\cos(\alpha))^2 {h_y}^2 \\
& - 4\, \cos(\alpha)\, y_I \sin(\alpha)\, x_I x_{o'} b_{x13I} - 4\, \cos(\alpha)\, y_I \sin(\alpha)\, x_I y_{o'} b_{y13I} \\
& - 4\, \cos(\alpha)\, y_I \sin(\alpha)\, x_I y_{o'} b_{y11I})
\end{cases}
\tag{A.36}
$$

$$
\begin{cases}
m_{11}^{I} & = \nu \sum_{I=1}^{4} \frac{14}{{h_x}^2 {h_y}^2} (x_I \cos(\alpha) y_I \sin(\alpha) (\cos(\alpha) b_{x7I} + \sin(\alpha) b_{y7I})) \\
& +(1-\nu) \sum_{I=1}^{4} \frac{2 x_I y_I}{{h_x}^2 {h_y}^2} (2 b_{x7I} (\sin(\alpha))^3 \\
& -2 \sin(\alpha) b_{x7I} (\cos(\alpha))^2 - (\sin(\alpha))^2 \cos(\alpha) b_{x8I} \\
& -2 (\sin(\alpha))^2 \cos(\alpha) b_{x10I} - 2 \cos(\alpha) b_{y7I} (\sin(\alpha))^2 \\
& +2 b_{y7I} (\cos(\alpha))^3 + \sin(\alpha) (\cos(\alpha))^2 b_{y8I} \\
& +2 \sin(\alpha) (\cos(\alpha))^2 b_{y10I}) \\
m_{12}^{I} & = \nu \sum_{I=1}^{4} (\frac{16 x_I \cos(\alpha) y_I \sin(\alpha) \left(\cos(\alpha) b_{x11I} + \cos(\alpha) b_{x13I} + \sin(\alpha) b_{y11I} + \sin(\alpha) b_{y13I}\right)}{{h_x}^2 {h_y}^2}) \\
& +(1-\nu) \sum_{I=1}^{4} \frac{4 x_I y_I}{{h_x}^2 {h_y}^2} ((\sin(\alpha))^3 b_{x11I} \\
& + (\sin(\alpha))^3 b_{x13I} - \sin(\alpha) (\cos(\alpha))^2 b_{x11I} \\
& - \sin(\alpha) (\cos(\alpha))^2 b_{x13I} - 2 (\sin(\alpha))^2 \cos(\alpha) b_{x12I} \\
& - (\sin(\alpha))^2 \cos(\alpha) b_{y11I} - (\sin(\alpha))^2 \cos(\alpha) b_{y13I} \\
& + (\cos(\alpha))^3 b_{y11I} + (\cos(\alpha))^3 b_{y13I} + 2 \sin(\alpha) (\cos(\alpha))^2 b_{y12I})
\end{cases}
\tag{A.37}
$$

$$
\begin{cases}
m_1^{II} & = \sum_{I=1}^{4} \frac{1}{2} \frac{\left({h_x}^2+4\,x_I x_{o'}\right)\left({h_y}^2+4\,y_I y_{o'}\right)\left(b_{x1I}\cos(\alpha)+b_{y1I}\sin(\alpha)\right)}{{h_x}^2{h_y}^2} \\
m_2^{II} & = \sum_{I=1}^{4} \frac{-1}{2{h_x}^2{h_y}^2}(-\cos(\alpha)\, b_{x8I}{h_x}^2{h_y}^2 - 4\,\cos(\alpha)\, b_{x8I}{h_x}^2 y_I y_{o'} \\
& \quad -4\,\cos(\alpha)\, b_{x8I}x_I x_{o'}{h_y}^2 - 16\,\cos(\alpha)\, b_{x8I}x_I x_{o'} y_I y_{o'} \\
& \quad +4\, b_{x1I}\cos(\alpha)\, y_I \sin(\alpha)\, {h_x}^2 + 16\, b_{x1I}\cos(\alpha)\, y_I \sin(\alpha)\, x_I x_{o'} \\
& \quad +4\, b_{x1I}x_I \left(\cos(\alpha)\right)^2 {h_y}^2 + 16\, b_{x1I}x_I \left(\cos(\alpha)\right)^2 y_I y_{o'} - \sin(\alpha)\, b_{y8I}{h_x}^2{h_y}^2 \\
& \quad -4\,\sin(\alpha)\, b_{y8I}{h_x}^2 y_I y_{o'} - 4\,\sin(\alpha)\, b_{y8I}x_I x_{o'}{h_y}^2 \\
& \quad -16\,\sin(\alpha)\, b_{y8I}x_I x_{o'} y_I y_{o'} + 4\, b_{y1I}y_I \left(\sin(\alpha)\right)^2 {h_x}^2 \\
& \quad +16\, b_{y1I}y_I \left(\sin(\alpha)\right)^2 x_I x_{o'} + 4\, b_{y1I}\sin(\alpha)\, x_I \cos(\alpha)\, {h_y}^2 + 16\, b_{y1I}\sin(\alpha)\, x_I \cos(\alpha)\, y_I y_{o'}) \\
m_3^{II} & = \sum_{I=1}^{4} \frac{2}{{h_x}^2{h_y}^2}(-\cos(\alpha)\, b_{x8I}y_I \sin(\alpha)\, {h_x}^2 \\
& \quad -4\,\cos(\alpha)\, b_{x8I}y_I \sin(\alpha)\, x_I x_{o'} - b_{x8I}x_I \left(\cos(\alpha)\right)^2 {h_y}^2 - 4\, b_{x8I}x_I \left(\cos(\alpha)\right)^2 y_I y_{o'} \\
& \quad +4\, x_I \left(\cos(\alpha)\right)^2 y_I \sin(\alpha)\, b_{x1I} - b_{y8I}y_I \left(\sin(\alpha)\right)^2 {h_x}^2 \\
& \quad -4\, b_{y8I}y_I \left(\sin(\alpha)\right)^2 x_I x_{o'} - \sin(\alpha)\, b_{y8I}x_I \cos(\alpha)\, {h_y}^2 \\
& \quad -4\,\sin(\alpha)\, b_{y8I}x_I \cos(\alpha)\, y_I y_{o'} + 4\, x_I \cos(\alpha)\, y_I \left(\sin(\alpha)\right)^2 b_{y1I}) \\
m_4^{II} & = \sum_{I=1}^{4} 8\, \frac{x_I \cos(\alpha) y_I \sin(\alpha)\left(\cos(\alpha)b_{x8I}+\sin(\alpha)b_{y8I}\right)}{{h_x}^2{h_y}^2}
\end{cases}
\tag{A.38}
$$

$$
\begin{cases}
m_5^{II} & = \sum_{I=1}^{4} \left(\frac{1}{8} \frac{\left({h_x}^2+4\,x_I x_{o'}\right)\left({h_y}^2+4\,y_I y_{o'}\right)\left(b_{x1I}\cos(\alpha)+2\,\cos(\alpha) b_{x4I}-b_{x2I}\sin(\alpha)+b_{y1I}\sin(\alpha)+2\,\sin(\alpha) b_{y4I}+b_{y2I}\cos(\alpha)\right)}{{h_x}^2 {h_y}^2} \right) \\
m_6^{II} & = \sum_{I=1}^{4} \frac{1}{4{h_x}^2{h_y}^2} (\, 16\,\sin\left(\alpha\right) b_{y6I} x_I x_{o'} y_I y_{o'} - 16\,\sin\left(\alpha\right) b_{x5I} x_I x_{o'} y_I y_{o'} \\
 & \quad +16\,\cos\left(\alpha\right) b_{y5I} x_I x_{o'} y_I y_{o'} + 32\,\sin\left(\alpha\right) u_{yI} y_I \cos\left(\alpha\right) x_I x_{o'} \\
 & \quad +4\,u_{xI} y_I \left(\cos\left(\alpha\right)\right)^2 {h_x}^2 + \cos\left(\alpha\right) b_{x6I} {h_x}^2 {h_y}^2 - 4\,u_{yI} x_I \left(\sin\left(\alpha\right)\right)^2 {h_y}^2 \\
 & \quad +\sin\left(\alpha\right) b_{y6I} {h_x}^2 {h_y}^2 - 4\,u_{xI} y_I \left(\sin\left(\alpha\right)\right)^2 {h_x}^2 - \sin\left(\alpha\right) b_{x5I} {h_x}^2 {h_y}^2 \\
 & \quad +4\,u_{yI} x_I \left(\cos\left(\alpha\right)\right)^2 {h_y}^2 + \cos\left(\alpha\right) b_{y5I} {h_x}^2 {h_y}^2 - 8\,\cos\left(\alpha\right) u_{xI} x_I \sin\left(\alpha\right) {h_y}^2 \\
 & \quad +16\,u_{xI} y_I \left(\cos\left(\alpha\right)\right)^2 x_I x_{o'} + 4\,\cos\left(\alpha\right) b_{x6I} {h_x}^2 y_I y_{o'} + 4\,\cos\left(\alpha\right) b_{x6I} x_I x_{o'} {h_y}^2 \\
 & \quad -16\,u_{yI} x_I \left(\sin\left(\alpha\right)\right)^2 y_I y_{o'} + 8\,\sin\left(\alpha\right) u_{yI} y_I \cos\left(\alpha\right) {h_x}^2 \\
 & \quad +4\,\sin\left(\alpha\right) b_{y6I} {h_x}^2 y_I y_{o'} + 4\,\sin\left(\alpha\right) b_{y6I} x_I x_{o'} {h_y}^2 - 16\,u_{xI} y_I \left(\sin\left(\alpha\right)\right)^2 x_I x_{o'} \\
 & \quad -4\,\sin\left(\alpha\right) b_{x5I} {h_x}^2 y_I y_{o'} - 4\,\sin\left(\alpha\right) b_{x5I} x_I x_{o'} {h_y}^2 + 16\,u_{yI} x_I \left(\cos\left(\alpha\right)\right)^2 y_I y_{o'} \\
 & \quad +4\,\cos\left(\alpha\right) b_{y5I} {h_x}^2 y_I y_{o'} + 4\,\cos\left(\alpha\right) b_{y5I} x_I x_{o'} {h_y}^2 - 32\,\cos\left(\alpha\right) u_{xI} x_I \sin\left(\alpha\right) y_I y_{o'} \\
 & \quad +16\,\cos\left(\alpha\right) b_{x6I} x_I x_{o'} y_I y_{o'})
\end{cases}
\tag{A.39}
$$

$$
\begin{cases}
m_7^{II} & = \sum_{I=1}^{4} \frac{1}{8{h_x}^2{h_y}^2}(48\, b_{y2I} x_I \left(\cos\left(\alpha\right)\right)^2 y_I y_{o'} + 12\, \cos\left(\alpha\right) b_{y7I} {h_x}^2 y_I y_{o'} \\
& +12\, \cos\left(\alpha\right) b_{y7I} x_I x_{o'} {h_y}^2 + 8\, \sin\left(\alpha\right) x_I \cos\left(\alpha\right) {h_y}^2 b_{y4I} - 48\, b_{x2I} y_I \left(\sin\left(\alpha\right)\right)^2 x_I x_{o'} \\
& -12\, \sin\left(\alpha\right) b_{x7I} {h_x}^2 y_I y_{o'} - 12\, \sin\left(\alpha\right) b_{x7I} x_I x_{o'} {h_y}^2 + 8\, \sin\left(\alpha\right) x_I x_{o'} {h_y}^2 b_{y10I} \\
& +32\, y_I \left(\sin\left(\alpha\right)\right)^2 x_I x_{o'} b_{y4I} + 8\, \sin\left(\alpha\right) {h_x}^2 y_I y_{o'} b_{y10I} \\
& +20\, \sin\left(\alpha\right) b_{y2I} y_I \cos\left(\alpha\right) {h_x}^2 - 32\, b_{y2I} x_I \left(\sin\left(\alpha\right)\right)^2 y_I y_{o'} \\
& +8\, \cos\left(\alpha\right) x_I x_{o'} {h_y}^2 b_{x10I} + 12\, b_{y2I} x_I \left(\cos\left(\alpha\right)\right)^2 {h_y}^2 \\
& +3\, \cos\left(\alpha\right) b_{y7I} {h_x}^2 {h_y}^2 + 8\, \cos\left(\alpha\right) {h_x}^2 y_I y_{o'} b_{x10I} + 32\, b_{x2I} y_I \left(\cos\left(\alpha\right)\right)^2 x_I x_{o'} \\
& -3\, \sin\left(\alpha\right) b_{x7I} {h_x}^2 {h_y}^2 + 8\, y_I \left(\sin\left(\alpha\right)\right)^2 {h_x}^2 b_{y4I} - 12\, b_{x2I} y_I \left(\sin\left(\alpha\right)\right)^2 {h_x}^2 \\
& -8\, b_{y2I} x_I \left(\sin\left(\alpha\right)\right)^2 {h_y}^2 + 2\, \sin\left(\alpha\right) {h_x}^2 {h_y}^2 b_{y10I} \\
& +8\, x_I \left(\cos\left(\alpha\right)\right)^2 {h_y}^2 b_{x4I} + 2\, \cos\left(\alpha\right) {h_x}^2 {h_y}^2 b_{x10I} \\
& -20\, \cos\left(\alpha\right) b_{x2I} x_I \sin\left(\alpha\right) {h_y}^2 + 8\, b_{x2I} y_I \left(\cos\left(\alpha\right)\right)^2 {h_x}^2 \\
& +48\, \cos\left(\alpha\right) b_{y7I} x_I x_{o'} y_I y_{o'} + 32\, \cos\left(\alpha\right) y_I \sin\left(\alpha\right) x_I x_{o'} b_{x4I} + 80\, \sin\left(\alpha\right) b_{y2I} y_I \cos\left(\alpha\right) x_I x_{o'} \\
& +32\, \sin\left(\alpha\right) x_I x_{o'} y_I y_{o'} b_{y10I} + 32\, \cos\left(\alpha\right) y_I \sin\left(\alpha\right) x_I y_{o'} b_{y4I} - 48\, \sin\left(\alpha\right) b_{x7I} x_I x_{o'} y_I y_{o'} \\
& -80\, \cos\left(\alpha\right) b_{x2I} x_I \sin\left(\alpha\right) y_I y_{o'} + 32\, \cos\left(\alpha\right) x_I x_{o'} y_I y_{o'} b_{x10I} \\
& +32\, x_I \left(\cos\left(\alpha\right)\right)^2 y_I y_{o'} b_{x4I} + 16\, b_{x1I} \cos\left(\alpha\right) y_I \sin\left(\alpha\right) x_I x_{o'} + 16\, \sin\left(\alpha\right) b_{y8I} x_I x_{o'} y_I y_{o'} \\
& +16\, b_{y1I} \sin\left(\alpha\right) x_I \cos\left(\alpha\right) y_I y_{o'} + 4\, b_{x1I} x_I \left(\cos\left(\alpha\right)\right)^2 {h_y}^2 \\
& +\sin\left(\alpha\right) b_{y8I} {h_x}^2 {h_y}^2 + 4\, b_{y1I} y_I \left(\sin\left(\alpha\right)\right)^2 {h_x}^2 + 16\, \cos\left(\alpha\right) b_{x8I} x_I x_{o'} y_I y_{o'} \\
& +4\, \cos\left(\alpha\right) b_{x8I} {h_x}^2 y_I y_{o'} + 4\, \cos\left(\alpha\right) b_{x8I} x_I x_{o'} {h_y}^2 + 4\, b_{x1I} \cos\left(\alpha\right) y_I \sin\left(\alpha\right) {h_x}^2 \\
& +16\, b_{x1I} x_I \left(\cos\left(\alpha\right)\right)^2 y_I y_{o'} + 4\, \sin\left(\alpha\right) b_{y8I} {h_x}^2 y_I y_{o'} + 4\, \sin\left(\alpha\right) b_{y8I} x_I x_{o'} {h_y}^2 \\
& +16\, b_{y1I} y_I \left(\sin\left(\alpha\right)\right)^2 x_I x_{o'} + 4\, b_{y1I} \sin\left(\alpha\right) x_I \cos\left(\alpha\right) {h_y}^2 + \cos\left(\alpha\right) b_{x8I} {h_x}^2 {h_y}^2 \\
& +8\, \cos\left(\alpha\right) y_I \sin\left(\alpha\right) {h_x}^2 b_{x4I})
\end{cases}
\tag{A.40}
$$

$$
\begin{cases}
m_8^{II} & = \sum_{I=1}^{4} \frac{1}{2{h_x}^2{h_y}^2} (16 \cos(\alpha) x_I x_{o'} y_I y_{o'} b_{y11I} + 16 \cos(\alpha) x_I x_{o'} y_I y_{o'} b_{y13I} \\
& +16 \cos(\alpha) b_{x12I} x_I x_{o'} y_I y_{o'} + 8 \cos(\alpha) b_{x6I} y_I \sin(\alpha) x_I x_{o'} + 16 \sin(\alpha) b_{y12I} x_I x_{o'} y_I y_{o'} \\
& +8 \sin(\alpha) b_{y6I} x_I \cos(\alpha) y_I y_{o'} - 4 b_{x5I} y_I (\sin(\alpha))^2 {h_x}^2 \\
& - \sin(\alpha) {h_x}^2 {h_y}^2 b_{x11I} - \sin(\alpha) {h_x}^2 {h_y}^2 b_{x13I} + 4 b_{y5I} x_I (\cos(\alpha))^2 {h_y}^2 \\
& + \cos(\alpha) {h_x}^2 {h_y}^2 b_{y11I} + \cos(\alpha) {h_x}^2 {h_y}^2 b_{y13I} + 2 b_{x5I} y_I (\cos(\alpha))^2 {h_x}^2 \\
& +8 x_I y_I u_{xI} (\cos(\alpha))^3 + \cos(\alpha) b_{x12I} {h_x}^2 {h_y}^2 + 2 b_{x6I} x_I (\cos(\alpha))^2 {h_y}^2 \\
& -2 b_{y5I} x_I (\sin(\alpha))^2 {h_y}^2 - 8 x_I y_I u_{yI} (\sin(\alpha))^3 \\
& + \sin(\alpha) b_{y12I} {h_x}^2 {h_y}^2 + 2 b_{y6I} y_I (\sin(\alpha))^2 {h_x}^2 + 24 \cos(\alpha) b_{y5I} y_I \sin(\alpha) x_I x_{o'} \\
& -16 \sin(\alpha) x_I x_{o'} y_I y_{o'} b_{x13I} - 16 \sin(\alpha) x_I x_{o'} y_I y_{o'} b_{x11I} - 24 \sin(\alpha) b_{x5I} x_I \cos(\alpha) y_I y_{o'} \\
& -16 b_{x5I} y_I (\sin(\alpha))^2 x_I x_{o'} - 6 \sin(\alpha) b_{x5I} x_I \cos(\alpha) {h_y}^2 - 24 \cos(\alpha) x_I y_I (\sin(\alpha))^2 u_{xI} \\
& -4 \sin(\alpha) {h_x}^2 y_I y_{o'} b_{x11I} - 4 \sin(\alpha) {h_x}^2 y_I y_{o'} b_{x13I} - 4 \sin(\alpha) x_I x_{o'} {h_y}^2 b_{x11I} \\
& -4 \sin(\alpha) x_I x_{o'} {h_y}^2 b_{x13I} + 6 \cos(\alpha) b_{y5I} y_I \sin(\alpha) {h_x}^2 + 16 b_{y5I} x_I (\cos(\alpha))^2 y_I y_{o'} \\
& +24 x_I (\cos(\alpha))^2 y_I \sin(\alpha) u_{yI} + 4 \cos(\alpha) {h_x}^2 y_I y_{o'} b_{y11I} + 4 \cos(\alpha) {h_x}^2 y_I y_{o'} b_{y13I} \\
& +4 \cos(\alpha) x_I x_{o'} {h_y}^2 b_{y11I} + 4 \cos(\alpha) x_I x_{o'} {h_y}^2 b_{y13I} + 8 b_{x5I} y_I (\cos(\alpha))^2 x_I x_{o'} \\
& +4 \cos(\alpha) b_{x12I} {h_x}^2 y_I y_{o'} + 4 \cos(\alpha) b_{x12I} x_I x_{o'} {h_y}^2 + 2 \cos(\alpha) b_{x6I} y_I \sin(\alpha) {h_x}^2 \\
& +8 b_{x6I} x_I (\cos(\alpha))^2 y_I y_{o'} - 8 b_{y5I} x_I (\sin(\alpha))^2 y_I y_{o'} + 4 \sin(\alpha) b_{y12I} {h_x}^2 y_I y_{o'} \\
& +4 \sin(\alpha) b_{y12I} x_I x_{o'} {h_y}^2 + 8 b_{y6I} y_I (\sin(\alpha))^2 x_I x_{o'} + 2 \sin(\alpha) b_{y6I} x_I \cos(\alpha) {h_y}^2)
\end{cases}
\tag{A.41}
$$

$$
\begin{cases}
m_9^{II} & = \sum_{I=1}^{4} \frac{1}{2{h_x}^2{h_y}^2}(\cos(\alpha)\, b_{x8I} y_I \sin(\alpha)\, {h_x}^2 + 4\, b_{x8I} x_I (\cos(\alpha))^2\, y_I y_{o'} \\
& +4\, x_I (\cos(\alpha))^2\, y_I \sin(\alpha)\, b_{x1I} + 4\, b_{y8I} y_I (\sin(\alpha))^2\, x_I x_{o'} \\
& + \sin(\alpha)\, b_{y8I} x_I \cos(\alpha)\, {h_y}^2 + 4\, \cos(\alpha)\, x_I y_I (\sin(\alpha))^2\, b_{y1I} + 20\, b_{y\gamma I} x_I (\cos(\alpha))^2\, y_I y_{o'} \\
& +28\, x_I (\cos(\alpha))^2\, y_I \sin(\alpha)\, b_{y2I} - 20\, b_{x\gamma I} y_I (\sin(\alpha))^2\, x_I x_{o'} + 28\, \cos(\alpha)\, b_{y\gamma I} y_I \sin(\alpha)\, x_I x_{o'} \\
& +b_{x8I} x_I (\cos(\alpha))^2\, {h_y}^2 + b_{y8I} y_I (\sin(\alpha))^2\, {h_x}^2 - 5\, b_{x\gamma I} y_I (\sin(\alpha))^2\, {h_x}^2 \\
& +5\, b_{y\gamma I} x_I (\cos(\alpha))^2\, {h_y}^2 + 2\, b_{x\gamma I} y_I (\cos(\alpha))^2\, {h_x}^2 + 8\, x_I y_I b_{x2I} (\cos(\alpha))^3 \\
& +2\, x_I (\cos(\alpha))^2\, {h_y}^2 b_{x10I} - 2\, b_{y\gamma I} x_I (\sin(\alpha))^2\, {h_y}^2 - 8\, x_I y_I b_{y2I} (\sin(\alpha))^3 \\
& +2\, y_I (\sin(\alpha))^2\, {h_x}^2 b_{y10I} + 4\, \sin(\alpha)\, b_{y8I} x_I \cos(\alpha)\, y_I y_{o'} - 28\, \sin(\alpha)\, b_{x\gamma I} x_I \cos(\alpha)\, y_I y_{o'} \\
& +8\, \cos(\alpha)\, y_I \sin(\alpha)\, x_I x_{o'} b_{x10I} + 4\, \cos(\alpha)\, b_{x8I} y_I \sin(\alpha)\, x_I x_{o'} + 8\, \cos(\alpha)\, y_I \sin(\alpha)\, x_I y_{o'} b_{y10I} \\
& -7\, \sin(\alpha)\, b_{x\gamma I} x_I \cos(\alpha)\, {h_y}^2 - 28\, \cos(\alpha)\, x_I y_I (\sin(\alpha))^2\, b_{x2I} + 7\, \cos(\alpha)\, b_{y\gamma I} y_I \sin(\alpha)\, {h_x}^2 \\
& +8\, b_{x\gamma I} y_I (\cos(\alpha))^2\, x_I x_{o'} + 2\, \cos(\alpha)\, y_I \sin(\alpha)\, {h_x}^2 b_{x10I} + 8\, x_I (\cos(\alpha))^2\, y_I y_{o'} b_{x10I} \\
& +8\, x_I (\cos(\alpha))^2\, y_I \sin(\alpha)\, b_{x4I} - 8\, b_{y\gamma I} x_I (\sin(\alpha))^2\, y_I y_{o'} \\
& +8\, y_I (\sin(\alpha))^2\, x_I x_{o'} b_{y10I} + 2\, \sin(\alpha)\, x_I \cos(\alpha)\, {h_y}^2 b_{y10I} \\
& +8\, \cos(\alpha)\, x_I y_I (\sin(\alpha))^2\, b_{y4I})
\end{cases}
\tag{A.42}
$$

$$
\left\{
\begin{aligned}
m_{10}^{II} &= \textstyle\sum_{I=1}^{4} \frac{1}{{h_x}^2 {h_y}^2}(-x_I \left(\sin\left(\alpha\right)\right)^2 {h_y}^2 b_{y13I} + 8\,\sin\left(\alpha\right) b_{y12I} x_I \cos\left(\alpha\right) y_I y_{o'} + y_I \left(\cos\left(\alpha\right)\right)^2 {h_x}^2 b_{x13I} \\
&+ y_I \left(\cos\left(\alpha\right)\right)^2 {h_x}^2 b_{x11I} - x_I \left(\sin\left(\alpha\right)\right)^2 {h_y}^2 b_{y11I} + 2\, b_{x12I} x_I \left(\cos\left(\alpha\right)\right)^2 {h_y}^2 \\
&+ 4\, x_I y_I b_{x5I} \left(\cos\left(\alpha\right)\right)^3 - 4\, x_I y_I b_{y5I} \left(\sin\left(\alpha\right)\right)^3 + 2\, b_{y12I} y_I \left(\sin\left(\alpha\right)\right)^2 {h_x}^2 \\
&- 3\, y_I \left(\sin\left(\alpha\right)\right)^2 {h_x}^2 b_{x11I} - 3\, y_I \left(\sin\left(\alpha\right)\right)^2 {h_x}^2 b_{x13I} + 3\, x_I \left(\cos\left(\alpha\right)\right)^2 {h_y}^2 b_{y11I} \\
&- 4\,\cos\left(\alpha\right) x_I \sin\left(\alpha\right) {h_y}^2 b_{x11I} - 4\,\cos\left(\alpha\right) x_I \sin\left(\alpha\right) {h_y}^2 b_{x13I} + 4\, y_I \left(\cos\left(\alpha\right)\right)^2 x_I x_{o'} b_{x11I} \\
&+ 4\, y_I \left(\cos\left(\alpha\right)\right)^2 x_I x_{o'} b_{x13I} + 16\,\sin\left(\alpha\right) y_I \cos\left(\alpha\right) x_I x_{o'} b_{y11I} + 12\, x_I \left(\cos\left(\alpha\right)\right)^2 y_I y_{o'} b_{y13I} \\
&+ 3\, x_I \left(\cos\left(\alpha\right)\right)^2 {h_y}^2 b_{y13I} + 16\,\sin\left(\alpha\right) y_I \cos\left(\alpha\right) x_I x_{o'} b_{y13I} + 8\,\cos\left(\alpha\right) b_{x12I} y_I \sin\left(\alpha\right) x_I x_{o'} \\
&- 16\,\cos\left(\alpha\right) x_I \sin\left(\alpha\right) y_I y_{o'} b_{x11I} - 4\, x_I \left(\sin\left(\alpha\right)\right)^2 y_I y_{o'} b_{y11I} - 4\, x_I \left(\sin\left(\alpha\right)\right)^2 y_I y_{o'} b_{y13I} \\
&+ 4\,\sin\left(\alpha\right) y_I \cos\left(\alpha\right) {h_x}^2 b_{y11I} + 4\,\sin\left(\alpha\right) y_I \cos\left(\alpha\right) {h_x}^2 b_{y13I} + 16\,\sin\left(\alpha\right) x_I y_I b_{y5I} \left(\cos\left(\alpha\right)\right)^2 \\
&+ 8\, b_{y12I} y_I \left(\sin\left(\alpha\right)\right)^2 x_I x_{o'} + 2\,\sin\left(\alpha\right) b_{y12I} x_I \cos\left(\alpha\right) {h_y}^2 + 4\, x_I \cos\left(\alpha\right) y_I \left(\sin\left(\alpha\right)\right)^2 b_{y6I} \\
&- 12\, y_I \left(\sin\left(\alpha\right)\right)^2 x_I x_{o'} b_{x11I} - 12\, y_I \left(\sin\left(\alpha\right)\right)^2 x_I x_{o'} b_{x13I} + 12\, x_I \left(\cos\left(\alpha\right)\right)^2 y_I y_{o'} b_{y11I} \\
&- 16\,\cos\left(\alpha\right) x_I \sin\left(\alpha\right) y_I y_{o'} b_{x13I} - 16\,\cos\left(\alpha\right) x_I y_I b_{x5I} \left(\sin\left(\alpha\right)\right)^2 \\
&+ 2\,\cos\left(\alpha\right) b_{x12I} y_I \sin\left(\alpha\right) {h_x}^2 + 8\, b_{x12I} x_I \left(\cos\left(\alpha\right)\right)^2 y_I y_{o'} \\
&+ 4\, x_I \left(\cos\left(\alpha\right)\right)^2 y_I \sin\left(\alpha\right) b_{x6I}) \\
m_{11}^{II} &= \textstyle\sum_{I=1}^{4} \frac{2 x_I y_I}{{h_x}^2 {h_y}^2}(\, -9\,\cos\left(\alpha\right) \left(\sin\left(\alpha\right)\right)^2 b_{x7I} \\
&+ 2\, b_{x7I} \left(\cos\left(\alpha\right)\right)^3 + \left(\cos\left(\alpha\right)\right)^2 \sin\left(\alpha\right) b_{x8I} + 2\,\left(\cos\left(\alpha\right)\right)^2 \sin\left(\alpha\right) b_{x10I} - 2\, b_{y7I} \left(\sin\left(\alpha\right)\right)^3 \\
&+ 9\,\left(\cos\left(\alpha\right)\right)^2 \sin\left(\alpha\right) b_{y7I} + \cos\left(\alpha\right) \left(\sin\left(\alpha\right)\right)^2 b_{y8I} + 2\,\cos\left(\alpha\right) \left(\sin\left(\alpha\right)\right)^2 b_{y10I}) \\
m_{12}^{II} &= \textstyle\sum_{I=1}^{4} \frac{4 x_I y_I}{{h_x}^2 {h_y}^2}(\, -5\,\cos\left(\alpha\right) \left(\sin\left(\alpha\right)\right)^2 b_{x11I} - 5\,\cos\left(\alpha\right) \left(\sin\left(\alpha\right)\right)^2 b_{x13I} \\
&+ \left(\cos\left(\alpha\right)\right)^3 b_{x11I} + \left(\cos\left(\alpha\right)\right)^3 b_{x13I} + 2\,\left(\cos\left(\alpha\right)\right)^2 \sin\left(\alpha\right) b_{x12I} \\
&- \left(\sin\left(\alpha\right)\right)^3 b_{y11I} - \left(\sin\left(\alpha\right)\right)^3 b_{y13I} + 5\,\left(\cos\left(\alpha\right)\right)^2 \sin\left(\alpha\right) b_{y11I} \\
&+ 5\,\left(\cos\left(\alpha\right)\right)^2 \sin\left(\alpha\right) b_{y13I} + 2\,\cos\left(\alpha\right) \left(\sin\left(\alpha\right)\right)^2 b_{y12I})
\end{aligned}
\right.
\tag{A.43}
$$

A.7 Derivatives of displacement field and shape function in polar coordinates

The derivatives of the displacement field in Eq. (4.28) with respect to r and θ are

$$\frac{\partial u}{\partial r} = \sum_{I=1}^{4} \frac{\partial N_I}{\partial r} u_I + \sum_{I=1}^{4} \frac{\partial N_I}{\partial r} \sum_{j=1}^{n_F} F_j b_{jI} + \sum_{I=1}^{4} N_I \sum_{j=1}^{n_F} \frac{\partial F_j}{\partial r} b_{jI} \tag{A.44}$$

$$\frac{\partial u}{\partial \theta} = \sum_{I=1}^{4} \frac{\partial N_I}{\partial \theta} u_I + \sum_{I=1}^{4} \frac{\partial N_I}{\partial \theta} \sum_{j=1}^{n_F} F_j b_{jI} + \sum_{I=1}^{4} N_I \sum_{j=1}^{n_F} \frac{\partial F_j}{\partial \theta} b_{jI} \tag{A.45}$$

where the derivatives of the shape functions are

$$\frac{\partial N_I}{\partial r} = \frac{x_I \cos(\theta+\alpha)}{h_x^2}(1+4\frac{y_I(r\sin(\theta+\alpha)+y_{o'})}{h_y^2})+\frac{y_I \sin(\theta+\alpha)}{h_y^2}(1+4\frac{x_I(r\cos(\theta+\alpha)+x_{o'})}{h_x^2}) \tag{A.46}$$

$$\frac{\partial N_I}{\partial \theta} = -\frac{x_I r \sin(\theta+\alpha)}{h_x^2}(1+4\frac{y_I(r\sin(\theta+\alpha)+y_{o'})}{h_y^2})+\frac{y_I r \cos(\theta+\alpha)}{h_y^2}(1+4\frac{x_I(r\cos(\theta+\alpha)+x_{o'})}{h_x^2}) \tag{A.47}$$